NONLINEAR EFFECTS IN THE VERTICAL MOTION OF IONS IN A SUPERCONDUCTING CYCLOTRON

By

Dong-o Jeon

A DISSERTATION

Submitted to
Michigan State University
in partial fulfillment of the requirements
for the Degree of

DOCTOR OF PHILOSOPHY

Department of Physics and Astronomy

1995

ABSTRACT

NONLINEAR EFFECTS IN THE VERTICAL MOTION OF IONS IN A SUPERCONDUCTING CYCLOTRON

By

Dong-o Jeon

Coupling effects near the $\nu_z = 3/4$ nonlinear resonance were studied both numerically using the new Z^{2N} Orbit Code and theoretically utilizing an expansion of the Hamiltonian to the fourth order in the vertical motion. A simple one-dimensional model provided only a qualitative agreement, however close the operating point came to the resonance. It turned out that inclusion of third-order coupling terms in the Hamiltonian that are associated with certain nonlinear coupling resonances relatively far away from the operating point provides an excellent explanation of phase space diagrams both quantitatively and qualitatively.

The effects of higher order terms in the magnetic field components were studied numerically using the new Z^{2N} Orbit Code. The following cases were used for this study: the change brought about to phase space diagrams by higher order terms near the $\nu_z = 3/4$ resonance, the evolution of an eigenellipse during acceleration from 10 MeV/u to the final energy, 40 MeV/u, and the higher order effects on the sixth-order $\nu_z = 3/6$ resonance.

The new Z^{2N} Orbit Code uses "improved differentiators" based on a finite difference technique, which overcome the difficulties presented by the "old differentiators" of the original Z^4 Orbit Code. A comparison for the individual terms in the field

components shows that the "old differentiators" are less effective in suppressing high frequency components and also tend to wash out physically important slowly varying components of data. The orbit computation results from the original Z^4 Orbit Code using the "old differentiators" show a highly chaotic behavior that appears unrealistic. A detailed description of the improved differentiators is given in the appendix together with the applications to the magnetic field produced by two saturated iron bars where the exact analytical expressions for the field components are available.

To Father and my family.

ACKNOWLEDGEMENTS

I am deeply grateful to God for having guided me during the course of my life and for having blessed me so much. I owe what I am today totally to God. I'd like to express my deep gratitude to Prof. M. M. Gordon for his years of guidance and kindness. I can't help mentioning that his advice and criticism have been enlightening and helpful. I'd also like to thank Prof. H. Blosser, Dr. F. Marti, and Mr. D. Johnson for their advice and guidance. Also I'd like to thank all the guidance committee members and fellow graduate students. Many thanks go to the National Science Foundation that has made my study possible.

Contents

List of Tables

List of Figures

Chapter 1

Introduction and summary

The Z^4 Orbit Code [1] was originally developed for evaluating non-linear effects that can seriously affect the beam quality during the process of extraction from superconducting cyclotrons. In addition, this orbit code can be used for semi-empirical studies of third and fourth-order resonances that can occur in these cyclotrons. One such study, that of the $2\nu_z = \nu_r$ resonance, has already been reported on [2].

The Z^4 Orbit Code uses exact equations of motion with magnetic field components (B_r, B_θ, B_z) that are evaluated up to fourth-order in z. This evaluation requires up to four successive derivatives of the measured median plane field data. Because of the noise inherent in such data, the calculation of successive derivatives can sometimes lead to spurious results. To overcome this difficulty, a new method of calculating field derivatives has recently been implemented [3]. This method makes use of finite difference techniques like those used in digital signal processing to suppress the noise and produce smoother derivatives.

The main part of this thesis deals with the results obtained from a study of a fourth-order resonance, $\nu_z = 3/4$, that usually occurs in three-sector superconducting cyclotrons when the field level is relatively low. For this purpose, we chose a K1200 superconducting cyclotron [4, 5, 6] field used for ions with $q/A = 0.25$ and a nominal

final energy of 40 MeV/u. Figure 1.1 shows a plot of ν_z vs. ν_r for energies between 10 and 40 MeV/u. The relevant third-order and fourth-order resonances are shown by various straight lines, and we note that $\nu_z = 3/4$ occurs at 35.6 MeV/u.

Even though the $\nu_z = 3/4$ resonance does not lead to an actual instability, acceleration of the beam through this resonance can produce a noticeable deformation of the vertical phase space. This is shown by the phase plots in Fig. 1.2 for two sets of orbits starting on eigenellipses at 34 MeV/u ($\nu_z = 0.721$) with vertical widths $\Delta z = 5$ mm and $\Delta z = 10$ mm. These orbits are run for 99 turns out through the resonance to 39 MeV/u ($\nu_z = 0.782$). The resultant two phase plots shown at the final energy indicate how the deformation depends on amplitude.

All of these orbits start with identical values of $(r,\ p_r)$ on the same (accelerated) equilibrium orbit at 34 MeV/u. Figure 1.3 shows the corresponding pair of radial phase space areas at the final energy that are produced by certain nonlinear coupling effects. The radial widths here, $\Delta x = 0.08$ mm and $\Delta x = 0.28$ mm, are considerably smaller than the corresponding Δz values given above, and moreover, are roughly proportional to $(\Delta z)^2$. Such coupling effects are clearly undesirable, and indicate once more the importance of controlling the range of vertical (and radial) displacements.

The $\nu_r = 3/4$ and $\nu_z = 3/4$ resonances are obviously different since the former involves motion entirely in the median plane and is therefore a simple one-dimensional resonance [7, 8, 9]. For the $\nu_z = 3/4$ case, however, coupling between the z and x motion is inevitable as shown in Figs. 1.2 and 1.3. Nevertheless, one would expect that for small vertical amplitudes close to the resonance, the vertical phase space properties, and especially the location of fixed points, could be described by the simple one-dimensional analysis. Although our results show that this is qualitatively true, they also show that the simple theory does not predict any of the fine structure apparent in the phase plots, no matter how close the operating point is to the

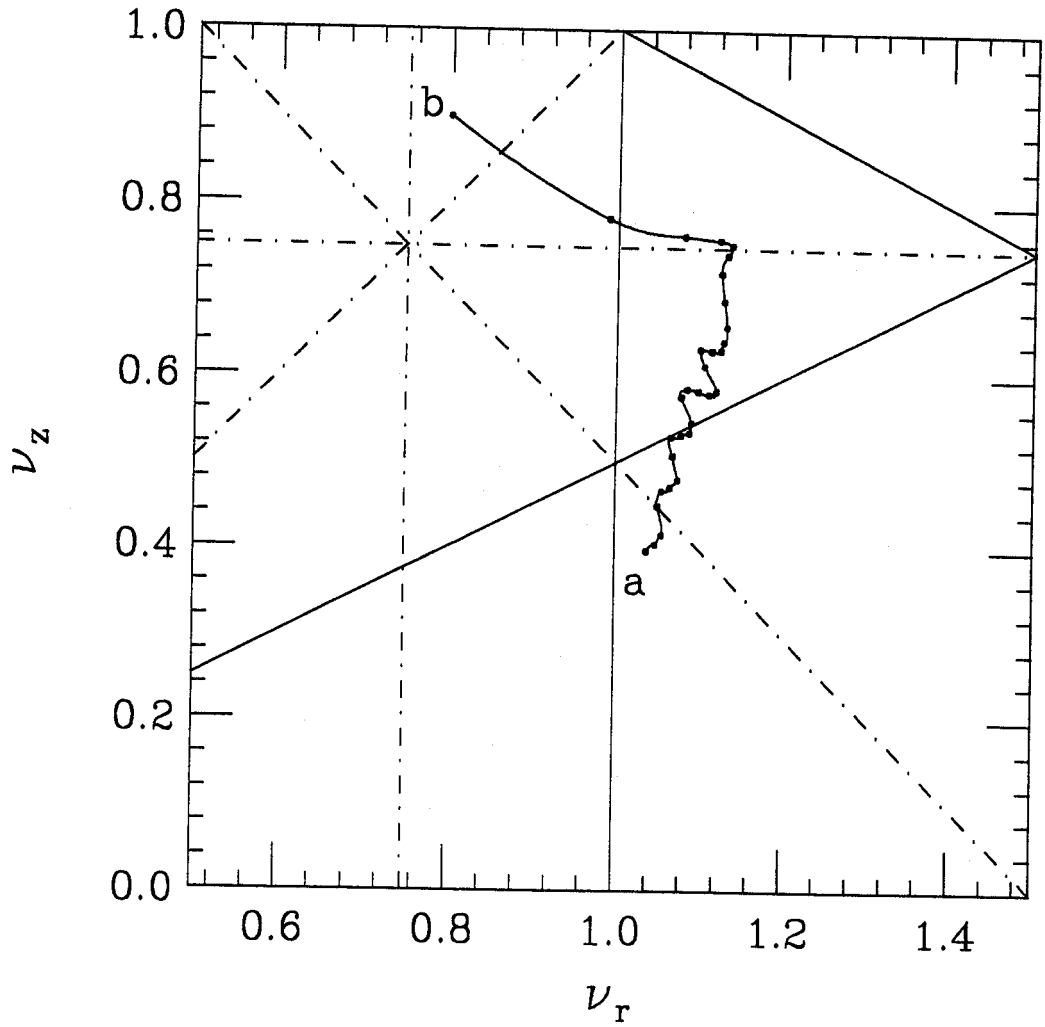

Figure 1.1: Tune diagram for a K1200 superconducting cyclotron field with $q/A = 0.25$ and a nominal final energy of 40 MeV/u. The diagram covers an energy range from 10 MeV/u (marked with "a") to 40 MeV/u (marked with "b") with points shown as small circles having integer energy values. Also shown are three solid lines for the third-order resonances ($3\nu_r = 3$, $2\nu_z = \nu_r$, $\nu_r + 2\nu_z = 3$) and four dot-dash lines for the fourth-order resonances ($4\nu_z = 3$, $4\nu_r = 3$, $2\nu_r = 2\nu_z$, $2\nu_z + 2\nu_r = 3$). The $\nu_z = 3/4$ resonance occurs at 35.6 MeV/u, and this point ($\nu_r = 1.136$, $\nu_z = 0.750$) is apparently not very close to either of the third-order coupling resonances. Nevertheless, these two coupling resonances do affect appreciably the vertical motion near the $\nu_z = 3/4$ resonance.

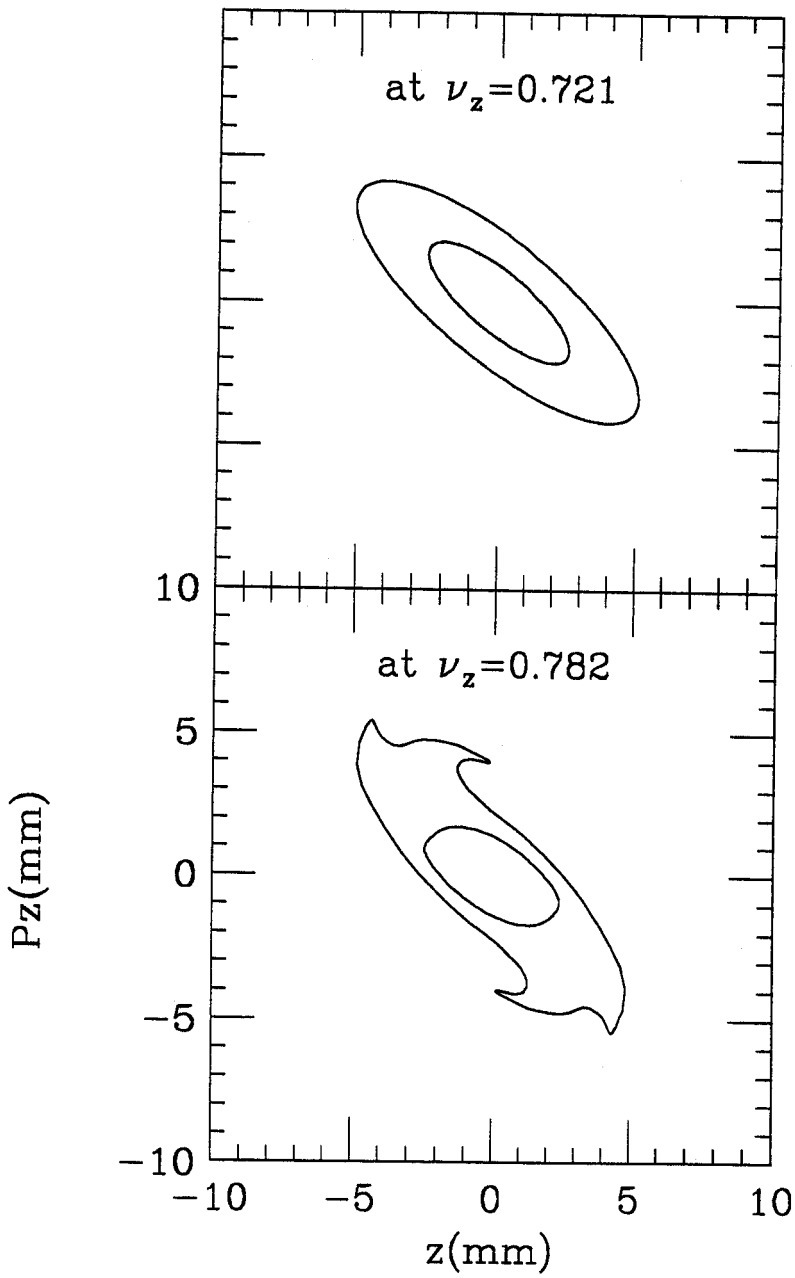

Figure 1.2: Initial and final (z, p_z) phase plots for orbits starting on two different eigenellipses at $E = 34$ MeV/u where $\nu_z = 0.721$ (at top) and accelerating through the resonance to 39 MeV/u where $\nu_z = 0.782$ (at bottom). The vertical widths of the eigenellipses are $\Delta z = 5$ mm and $\Delta z = 10$ mm. These orbits were run for 99 turns using the Z^{2N} Orbit Code with $N = 2$. Clearly, acceleration of the beam through the $\nu_z = 3/4$ resonance can produce significant deformation of the vertical phase space. (We should note that in all our orbit codes, momenta are expressed in length units by setting $\vec{p} \rightarrow \vec{p}/qB_0$, where B_0 is a given central field value. Here $B_0 = 35.1$ kG and our lengths are expressed in mm. $p = 988.7$ mm is the total momentum at $E = 35.6$ MeV/u.)

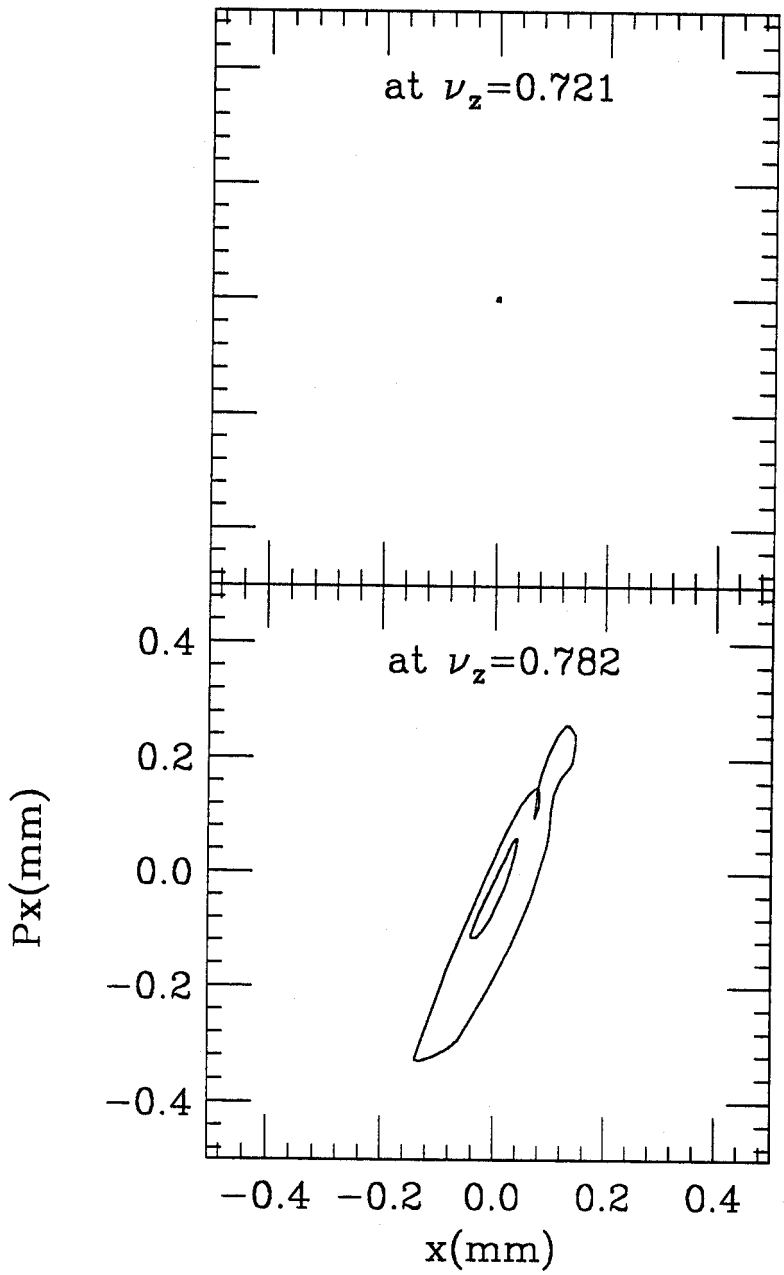

Figure 1.3: Initial and final $(x,\ p_x)$ phase plots for the two sets of orbits depicted in Fig. 1.2, which demonstrate the result of coupling from the z-motion into the x-motion. Because initially all of the orbits share identical values of $(r,\ p_r)$ at 34 MeV/u, they are depicted as a point (shown at top). Finally reaching 39 MeV/u after the acceleration (shown at bottom), the radial widths, $\Delta x = 0.08$ mm and $\Delta x = 0.28$ mm, are much smaller than the corresponding Δz values in Fig. 1.2 and roughly proportional to $(\Delta z)^2$.

resonance. We have, moreover, also found that this fine structure can be very well reproduced when the effects of third-order coupling terms are included in the analysis. One usually associates these terms with certain coupling resonances ($\nu_r - 2\nu_z = 0$ and $\nu_r + 2\nu_z = 3$), and although these resonances are not very close to our operating points, neither are they very far away (see Fig. 1.1).

The phase space properties near the $\nu_z = 3/4$ resonance were explored by comparing orbit code results with those obtained from a standard theoretical analysis based on an expansion of the Hamiltonian. In chapter 2, we present a detailed description on the expansion procedure of the Hamiltonian and on the subsequent canonical transformation using angle and action variables. The Hamiltonian was expanded around the equilibrium orbit order by order. In addition to the linear part, the part pertaining to the $\nu_z = 3/4$ resonance was kept. Concerning coupling terms, we retained only the most slowly varying components of the lowest order coupling terms in the Hamiltonian for the sake of simplicity. A canonical transformation using angle and action variables was carried out assuming that the terms relevant to the $\nu_z = 3/4$ resonance and the coupling terms are perturbations on the linear motion.

In chapter 3, comparisons between orbit computations and the theory are presented at two different values of ν_z, 0.740 and 0.749. We considered two different theoretical models, the simple one-dimensional Hamiltonian model by itself and the same simple model together with the coupling terms. These studies show, for example, that inclusion of the coupling terms reduced the error in the location of the unstable fixed points from about 40 % to about 10 % for both $\nu_z = 0.740$ and $\nu_z = 0.749$. In addition to providing a good explanation of the fine structure in the z-space phase plots, the simple theory including the coupling terms also provides a remarkably good representation of the x-space phase plots resulting from the coupling of the vertical motion into the radial motion.

Chapter 4 starts with a brief description of the Z^{2N} Orbit Code that enables one to use magnetic field components containing all terms up to z^{2N} with N =1, 2, 3, or 4, as desired. The orbit computations described in chapter 3 were carried out with this code using $N = 2$. To see how important higher order terms might be, we repeated some of these computations using the $N = 3$ and $N = 4$ options, which corresponds to including magnetic field terms up to z^6 and z^8 respectively. The results of this study, which are presented in section 4.2, show that for the $\nu_z = 3/4$ resonance, the higher order terms are not significant for the range of z values of interest in the K1200 superconducting cyclotron.

To investigate further the higher order effects, we examined briefly the sixth-order resonance $\nu_z = 3/6$ using the Z^{2N} Orbit Code with $N = 2$ as well as $N = 3$. Both versions of the code produced phase space patterns with fixed points that are typical of a sixth-order resonance, as shown in section 4.3. Moreover, the locations of the fixed points in the two cases differ by only about 14 % which seems somewhat surprising since the $N = 2$ option has no field components with terms higher than fourth-order.

Data are presented in chapter 5 showing the difference in results obtained by using the "old differentiators" and the "improved differentiators" to calculate magnetic field components off the median plane. First a comparison is given for the individual terms in these field components evaluated at $z = 0.5$ in. The results show that the "old differentiators" are less effective in suppressing high frequencies associated with noise and at the same time, they also tend to wash out physically important slowly varying parts of the data. In addition, a comparison is made of some orbits near the $\nu_z = 3/4$ resonance using the old Z^4 Orbit Code and the new Z^{2N} Orbit Code with $N = 2$, which utilized the old and improved differentiators, respectively. These orbits lie in a highly sensitive region of phase space close to the separatrices, and the results from the old Z^4 Orbit Code show a highly chaotic behavior that appears unrealistic.

Finally in the appendix, a detailed description of the improved differentiators is presented. As shown by frequency response curves, the improved method for evaluating derivatives suppresses high frequency signals effectively, while maintaining reasonable accuracy over a sufficiently wide range of low frequencies. The improved first-order and second-order differentiators for a uniform mesh in both one and two dimensions are presented. As a test, these differentiators were applied to the magnetic field produced by two magnetized iron bars where an exact analytical expression for the magnetic field is known, and also applied to the same field when a small amount of noise is superimposed. These results clearly demonstrate the superiority of the improved differentiators.

The work described in this thesis has produced two papers. One dealing with the coupling effects at the $\nu_z = 3/4$ resonance has been published in Nuclear Instruments and Methods A [10]. The other deals with the new method for calculating field components off the median plane and has been accepted for publication in the Journal of Computational Physics [3].

Chapter 2

Hamiltonian theory

The K1200 and K500 superconducting cyclotrons at this laboratory [11, 12] both have three magnet sectors with three dees in the intervening valleys. For this study, we have assumed that the field has perfect three-sector symmetry, and have, for simplicity, ignored all imperfections.

In both the computations and the analysis, the magnetic field components in cylindrical polar coordinates up to z^4 are calculated using:

$$B_z = -\left[B(r,\theta) - \frac{z^2}{2!}\nabla_2^2 B(r,\theta) + \frac{z^4}{4!}\nabla_2^4 B(r,\theta)\right], \tag{2.1}$$

$$B_r = -\frac{\partial}{\partial r}C(r,\theta,z), \tag{2.2}$$

$$B_\theta = -\frac{\partial}{r\partial\theta}C(r,\theta,z), \tag{2.3}$$

where $B(r,\theta)$ is the measured median plane field, and

$$\nabla_2^2 \equiv \frac{\partial^2}{\partial r^2} + \frac{\partial}{r\partial r} + \frac{\partial^2}{r^2\partial\theta^2}, \tag{2.4}$$

is the two-dimensional Laplacian, and

$$C(r,\theta,z) \equiv zB(r,\theta) - \frac{z^3}{3!}\nabla_2^2 B(r,\theta). \tag{2.5}$$

The above field components satisfy $\nabla \cdot \vec{B} = 0$ and can be derived from the following fourth-order vector potential components:

$$A_\theta = -\frac{1}{r}\int rB(r,\theta)\,dr + \frac{\partial}{\partial r}\left(\frac{z^2}{2!}B(r,\theta) - \frac{z^4}{4!}\nabla_2^2 B(r,\theta)\right), \tag{2.6}$$

$$A_r = \frac{\partial}{r\partial\theta}\left(-\frac{z^2}{2!}B(r,\theta) + \frac{z^4}{4!}\nabla_2^2 B(r,\theta)\right), \tag{2.7}$$

$$A_z = 0. \tag{2.8}$$

In the analysis of large synchrotrons and storage rings where Serret-Frenet coordinates are used, it is usually assumed that the component of $\vec{A}$ along the reference orbit is dominant and that the other components can be neglected. But for sectored cyclotrons, one obviously needs both A_r and A_θ.

With the expressions for the vector potential components on hand, we can now write down the Hamiltonian required for the analysis. With θ as the independent variable, this Hamiltonian is given by:

$$\begin{aligned} H_\theta &= -r\left(p^2 - p_r^2 - p_z^2\right)^{\frac{1}{2}} - qrA_\theta, \\ &= -r\left(p^2 - (\Pi_r - qA_r)^2 - \Pi_z^2\right)^{\frac{1}{2}} - qrA_\theta, \end{aligned} \tag{2.9}$$

where p is the total momentum, and where p_r and p_z are components of the mechanical momentum, while Π_r and Π_z are the corresponding canonical momenta. Note that $\Pi_z = p_z$ since $A_z = 0$ and $(\Pi_r)_{z=0} = (p_r)_{z=0}$ since $(A_r)_{z=0} = 0$. We should also note that the equations of motion used in the Z^4 Orbit Code [1] can be derived from this Hamiltonian.

2.1 Expansion of Hamiltonian

The theoretical analysis proceeds by expanding the above H_θ about a given reference orbit, namely the equilibrium orbit (EO). For a given energy (and hence p) value, the

coordinates of this orbit (r_0, p_{r0}) can be determined as a function of θ using the EO Code [13]. Because midplane symmetry is assumed for magnetic field and the EO is on the median plane with $z = p_z$ (or Π_z) $= 0$, it is natural to expand the Hamiltonian H_θ in Eq. 2.9 with respect to z and Π_z (or p_z) in the first place. And subsequent expansion of the Hamiltonian up to fourth-order in z and Π_z is presented as follows:

$$\begin{aligned} H_\theta &= \left[q\int rBdr - rp_\theta\right] + \left[\frac{r}{2p_\theta}\Pi_z^2 + \frac{q}{2}\left(\frac{\Pi_r}{p_\theta}\frac{\partial B}{\partial\theta} - r\frac{\partial B}{\partial r}\right)z^2\right] + \\ &\quad \left[\frac{r}{8p_\theta^3}\Pi_z^4 + \frac{q\Pi_r}{4p_\theta^3}\frac{\partial B}{\partial\theta}z^2\Pi_z^2 + \right. \\ &\quad \left.\left(\frac{q^2}{8rp_\theta}\left(1+\frac{\Pi_r^2}{p_\theta^2}\right)\left(\frac{\partial B}{\partial\theta}\right)^2 - \frac{q\Pi_r}{4!p_\theta}\frac{\partial\nabla_2^2 B}{\partial\theta} + \frac{qr}{4!}\frac{\partial\nabla_2^2 B}{\partial r}\right)z^4\right] + \ldots, \\ &\equiv H_0 + H_2 + H_4 + \ldots, \end{aligned} \tag{2.10}$$

where H_0 is the zero-order Hamiltonian in z and Π_z, H_2 is the second-order Hamiltonian, and H_4 is the fourth-order Hamiltonian and where $p_\theta \equiv (p^2 - \Pi_r^2)^{\frac{1}{2}}$.

After the completion of expansion with respect to z and Π_z, the above Hamiltonian is again expanded around the EO with respect to x and Π_x for the purpose of taking account of the coupling effects and the subsequent deviations from the EO. Deviations from the EO are specified as x and p_x defined by:

$$x = r - r_0, \quad p_x = p_r - p_{r0}. \tag{2.11}$$

Since $\Pi_r = p_r + qA_r$, the corresponding canonical deviation is

$$\Pi_x = \Pi_r - p_{r0} = p_x + qA_r, \tag{2.12}$$

and, of course, $\Pi_z = p_z$ as noted above.

For the sake of simplicity, we restrict ourselves to the lowest order coupling terms in the Hamiltonian which come from the expansion of H_2 with respect to r and Π_r.

After being expanded around the EO, H_2 can be expressed as follows:

$$\begin{aligned} H_2 &= \left[\left(\frac{r}{2p_\theta}\right)_0 \Pi_z^2 + \frac{q}{2}\left(\frac{\Pi_r}{p_\theta}\frac{\partial B}{\partial \theta} - r\frac{\partial B}{\partial r}\right)_0 z^2\right] + \\ &\quad \left[\left(\frac{1}{2p_\theta}\right)_0 x\Pi_z^2 + \left(\frac{r\Pi_r}{2p_\theta^3}\right)_0 \Pi_x\Pi_z^2 + \left(\frac{q}{2p_\theta}\left(1+\frac{\Pi_r^2}{p_\theta^2}\right)\frac{\partial B}{\partial \theta}\right)_0 \Pi_x z^2 + \right. \\ &\quad \left. \frac{q}{2}\left(\frac{\Pi_r}{p_\theta}\frac{\partial^2 B}{\partial\theta\partial r} - \frac{\partial B}{\partial r} - r\frac{\partial^2 B}{\partial r^2}\right)_0 xz^2\right] + \ldots, \qquad (2.13) \\ &\equiv H_2^{(0)} + H_2^{(1)} + \ldots, \qquad (2.14) \end{aligned}$$

where $H_2^{(0)}$ is the zero-order part of H_2 in x and Π_x and $H_2^{(1)}$ is the first-order part, and where $()_0$ means that the quantity in the bracket is evaluated on the EO. It should be noted that $H_2^{(0)}$ contains all the terms pertaining to linear oscillations in z-space.

Most of the terms in $H_2^{(1)}$ are neglected for the sake of simplicity that are proportional to $x\Pi_z^2$, $\Pi_x\Pi_z^2$, and $\Pi_x z^2$ because they are small compared with the dominant term by an order of magnitude. The dominant term to be kept is

$$H_{coupl} \equiv \frac{q}{2}\left(\frac{\Pi_r}{p_\theta}\frac{\partial^2 B}{\partial\theta\partial r} - \frac{\partial B}{\partial r} - r\frac{\partial^2 B}{\partial r^2}\right)_0 xz^2. \qquad (2.15)$$

It should be noted that H_{coupl} consists of the important third-order coupling terms; that is, those proportional to xz^2 with the coefficients evaluated on the EO.

In a similar manner, H_4 can also be expanded around the EO with respect to x and Π_x as follows:

$$H_4 = H_4^{(0)} + H_4^{(1)} + \ldots, \qquad (2.16)$$

where $H_4^{(0)}$ is the zero-order part of H_4 with respect to x and Π_x and $H_4^{(1)}$ the first-order part and so forth. Of course, there are higher order coupling terms coming from H_2 and H_4 and so forth, but the results presented here are obtained by neglecting

all of them. Because all the higher order coupling terms are omitted for the sake of simplicity, only $H_4^{(0)}$ is retained for the analysis presented here:

$$H_4^{(0)} = \left(\frac{r}{8p_\theta^3}\right)_0 \Pi_z^4 + \left(\frac{q\Pi_r}{4p_\theta^3}\frac{\partial B}{\partial\theta}\right)_0 z^2\Pi_z^2 + \left(\frac{q^2}{8rp_\theta}\left(1+\frac{\Pi_r^2}{p_\theta^2}\right)\left(\frac{\partial B}{\partial\theta}\right)^2 - \frac{q\Pi_r}{4!p_\theta}\frac{\partial\nabla_2^2 B}{\partial\theta} + \frac{qr}{4!}\frac{\partial\nabla_2^2 B}{\partial r}\right)_0 z^4. \tag{2.17}$$

Most of the terms in $H_4^{(0)}$ are again ruled out for the sake of simplicity that are proportional to Π_z^4 and $z^2\Pi_z^2$ because they are small compared with the dominant term that is defined to be H_{res}:

$$H_{res} \equiv \left[\frac{q^2}{8rp_\theta}\left(1+\frac{\Pi_r^2}{p_\theta^2}\right)\left(\frac{\partial B}{\partial\theta}\right)^2 - \frac{q\Pi_r}{4!p_\theta}\frac{\partial\nabla_2^2 B}{\partial\theta} + \frac{qr}{4!}\frac{\partial\nabla_2^2 B}{\partial r}\right]_0 z^4. \tag{2.18}$$

It should be pointed out that H_{res} contains the important terms relevant to the $\nu_z = 3/4$ resonance, that is, the fourth-order terms proportional to z^4 with their coefficients evaluated on the EO.

Finally concerning H_0 in Eq. 2.10, only the terms relevant to linear oscillations in x-space are kept and the other higher order terms are neglected because the amplitude of the induced motion in x-space is small compared with that in z-space.

The expansion of the Hamiltonian, as a result, is divided into three parts as follows:

$$H_\theta = H_{lin} + H_{res} + H_{coupl}, \tag{2.19}$$

where H_{lin} contains all of the terms pertaining to the linear oscillations in the z-space and x-space, and H_{res} and H_{coupl} consist of the dominant fourth-order resonant terms and the dominant third-order coupling terms respectively. As was noted previously, in the expansion process we have for simplicity omitted many small terms that appeared insignificant even though they might affect the results.

2.2 Canonical transformation using angle and action variables

We next introduce angle and action variables, $(\phi_z,\ J_z)$ and $(\phi_x,\ J_x)$. If y stands for either z or x, then the required canonical transformation is

$$y = (2J_y\beta_y)^{\frac{1}{2}}\cos(\phi_y+\delta_y), \tag{2.20}$$

$$\Pi_y = -(2J_y/\beta_y)^{\frac{1}{2}}\left[\sin(\phi_y+\delta_y)+\alpha_y\cos(\phi_y+\delta_y)\right], \tag{2.21}$$

where the periodic Courant-Snyder parameters $\alpha_y = \alpha_y(\theta)$, $\beta_y = \beta_y(\theta)$, and the phases $\delta_y = \delta_y(\theta)$ are determined as a function of θ from the transfer matrix elements generated by the EO Code [13]. This transformation reduces the linear part of the Hamiltonian to:

$$H_{lin} = \nu_z J_z + \nu_r J_x, \tag{2.22}$$

so that for the linear motion, J_y =const. and $\phi_y = \nu_y\theta$+const., as expected.

Following the customary procedure, the nonlinear parts of the transformed Hamiltonian are treated as perturbations, and for this purpose, only the terms varying slowly with respect to θ are retained. Detailed description of the procedure is presented below for H_{res} and H_{coupl}.

Using the angle and action variables defined in Eq. 2.20 and 2.21, H_{res} can be written as follows:

$$H_{res} = J_z^2 f(\theta)\left[\cos 4(\phi_z+\delta_z)+4\cos 2(\phi_z+\delta_z)+3\right], \tag{2.23}$$

with

$$f(\theta) \equiv \frac{\beta_z^2}{2}\left(\frac{q^2}{8rp_\theta}\left(1+\frac{\Pi_r^2}{p_\theta^2}\right)\left(\frac{\partial B}{\partial\theta}\right)^2 - \frac{q\Pi_r}{4!p_\theta}\frac{\partial\nabla_2^2 B}{\partial\theta}+\frac{qr}{4!}\frac{\partial\nabla_2^2 B}{\partial r}\right)_0, \tag{2.24}$$

where $()_0$ means that the quantity in the parentheses is evaluated on the EO. Separating the functions dependent on ϕ_z from those dependent on θ which is an independent variable, and Fourier transforming the functions with respect to θ using the fact that they are periodic, we can rewrite H_{res} as follows:

$$\begin{aligned} H_{res} &= J_z^2 f(\theta)\left[\cos 4\delta_z \cos 4\phi_z - \sin 4\delta_z \sin 4\phi_z + \right. \\ &\quad \left. 4\cos 2\delta_z \cos 2\phi_z - 4\sin 2\delta_z \sin 2\phi_z + 3\right], \qquad (2.25) \\ &= J_z^2 \left[\left(A_0 + \sum_n A_n \cos(n\theta + a_n)\right)\cos 4\phi_z \right. \\ &\quad - \left(B_0 + \sum_n B_n \sin(n\theta + b_n)\right)\sin 4\phi_z \\ &\quad + \left(C_0 + \sum_n C_n \cos(n\theta + c_n)\right)\cos 2\phi_z \\ &\quad - \left(D_0 + \sum_n D_n \sin(n\theta + d_n)\right)\sin 2\phi_z \\ &\quad \left. + G_0 + \sum_n G_n \cos(n\theta + g_n)\right], \qquad (2.26) \end{aligned}$$

where a_n, b_n,..., and g_n are the phase of the nth harmonic and A_n, B_n,..., and G_n are the amplitude of the nth harmonic under Fourier transformation with respect to θ. Reshuffling the terms using the properties of trigonometric functions, we get:

$$\begin{aligned} H_{res} &= J_z^2 \{A_0 \cos 4\phi_z - B_0 \sin 4\phi_z + C_0 \cos 2\phi_z - D_0 \sin 2\phi_z + G_0 \\ &\quad + \frac{1}{2}\sum_n [A_n \cos(4\phi_z + n\theta + a_n) + A_n \cos(4\phi_z - n\theta - a_n) \\ &\quad + B_n \cos(4\phi_z + n\theta + b_n) - B_n \cos(4\phi_z - n\theta - b_n) \\ &\quad + C_n \cos(2\phi_z + n\theta + c_n) + C_n \cos(2\phi_z - n\theta - c_n) \\ &\quad + D_n \cos(2\phi_z + n\theta + d_n) - D_n \cos(2\phi_z - n\theta - d_n) \\ &\quad + 2G_n \cos(n\theta + g_n)]\}. \qquad (2.27) \end{aligned}$$

Retaining only the most slowly varying components and neglecting all the other rapidly varying terms in the vicinity of the $\nu_z = 3/4$ resonance, we obtain as a final form of the resonant Hamiltonian to be used for analysis:

$$H_{res} \approx J_z^2 \left[G_0 + \frac{A_3}{2} \cos\left(4\phi_z - 3\theta - a_3\right) - \frac{B_3}{2} \cos\left(4\phi_z - 3\theta - b_3\right) \right], \tag{2.28}$$

$$= J_z^2 \left[G_0 + Q \cos\left(4\phi_z - 3\theta + \psi_0\right) \right], \tag{2.29}$$

where

$$Q \equiv \frac{1}{2} \left(A_3^2 + B_3^2 - 2A_3 B_3 \cos\left(a_3 - b_3\right) \right)^{\frac{1}{2}},$$

$$\tan\psi_0 \equiv \frac{B_3 \sin b_3 - A_3 \sin a_3}{A_3 \cos a_3 - B_3 \cos b_3}.$$

When we follow again a similar procedure for H_{coupl} just as for H_{res}, using angle and action variables defined by

$$x = (2J_x\beta_x)^{\frac{1}{2}} \cos\left(\phi_x + \delta_x\right),$$

$$z = (2J_z\beta_z)^{\frac{1}{2}} \cos\left(\phi_z + \delta_z\right),$$

H_{coupl} can be rewritten as follows:

$$H_{coupl} = J_x^{\frac{1}{2}} J_z g\left(\theta\right) \frac{1}{2} \left(e^{i(\phi_x + \delta_x)} + e^{-i(\phi_x + \delta_x)} \right) \frac{1}{4} \left(e^{2i(\phi_z + \delta_z)} + e^{-2i(\phi_z + \delta_z)} + 2 \right), \tag{2.30}$$

with

$$g\left(\theta\right) = \frac{q}{2} \left(\frac{\Pi_r}{p_\theta} \frac{\partial^2 B}{\partial\theta \partial r} - \frac{\partial B}{\partial r} - r \frac{\partial^2 B}{\partial r^2} \right)_0 (2\beta_x)^{\frac{1}{2}} 2\beta_z. \tag{2.31}$$

It should be noted that $g\left(\theta\right)$ is a real function of θ.

After separating functions dependent on ϕ's from those depending on θ and reshuffling the terms, we get:

$$H_{coupl} = J_x^{\frac{1}{2}} J_z \frac{g\left(\theta\right)}{8} \left[2e^{i\delta_x} e^{i\phi_x} + 2e^{-i\delta_x} e^{-i\phi_x} + e^{i(2\delta_z + \delta_x)} e^{i(2\phi_z + \phi_x)} + \right.$$

$$\left. e^{-i(2\delta_z + \delta_x)} e^{-i(2\phi_z + \phi_x)} + e^{i(2\delta_z - \delta_x)} e^{i(2\phi_z - \phi_x)} + e^{-i(2\delta_z - \delta_x)} e^{-i(2\phi_z - \phi_x)} \right], \tag{2.32}$$

$$\equiv J_x^{\frac{1}{2}} J_z \left[S(\theta) e^{i\phi_x} + S^*(\theta) e^{-i\phi_x} + T(\theta) e^{i(2\phi_z+\phi_x)} + T^*(\theta) e^{-i(2\phi_z+\phi_x)} + U(\theta) e^{i(2\phi_z-\phi_x)} + U^*(\theta) e^{-i(2\phi_z-\phi_x)} \right], \tag{2.33}$$

where $*$ stands for complex conjugate and where

$$S(\theta) \equiv \frac{g(\theta)}{4} e^{i\delta_x},$$

$$T(\theta) \equiv \frac{g(\theta)}{8} e^{i(2\delta_z+\delta_x)},$$

$$U(\theta) \equiv \frac{g(\theta)}{8} e^{i(2\delta_z-\delta_x)}.$$

Fourier transforming complex functions $S(\theta)$, $T(\theta)$, and $U(\theta)$ with respect to θ exploiting the fact that they are periodic functions of θ, we can rewrite H_{coupl} as follows:

$$H_{coupl} = J_x^{\frac{1}{2}} J_z \left[\sum_n \left(S_n e^{i(\phi_x+n\theta)} + S_n^* e^{-i(\phi_x+n\theta)} \right) + \sum_n \left(T_n e^{i(2\phi_z+\phi_x+n\theta)} + T_n^* e^{-i(2\phi_z+\phi_x+n\theta)} \right) + \sum_n \left(U_n e^{i(2\phi_z-\phi_x+n\theta)} + U_n^* e^{-i(2\phi_z-\phi_x+n\theta)} \right) \right], \tag{2.34}$$

where S_n, T_n, and U_n are the complex amplitudes of $e^{in\theta}$ components of $S(\theta)$, $T(\theta)$, and $U(\theta)$ respectively.

Just as in the case of H_{res}, we again assume that the most slowly varying components of each part contribute most. Keeping only the most slowly varying components while taking into account the operating points near $\nu_z = 3/4$, we get:

$$H_{coupl} \approx J_x^{\frac{1}{2}} J_z \left[S_0 e^{i\phi_x} + S_0^* e^{-i\phi_x} + T_{-3} e^{i(2\phi_z+\phi_x-3\theta)} + T_{-3}^* e^{-i(2\phi_z+\phi_x-3\theta)} + U_0 e^{i(2\phi_z-\phi_x)} + U_0^* e^{-i(2\phi_z-\phi_x)} \right]. \tag{2.35}$$

Defining $S_0 \equiv C_1 e^{i\psi_1}/2$, $T_{-3} \equiv C_2 e^{i\psi_2}/2$, and $U_0 \equiv C_3 e^{i\psi_3}/2$ where $(C_j,\ \psi_j)$ for $j = 1, 2, 3$ are real constants, we then obtain, as a final form of H_{coupl} to be used for

analysis:

$$H_{coupl} \approx J_x^{\frac{1}{2}} J_z \left[C_1 \cos\left(\phi_x + \psi_1\right) + C_2 \cos\left(2\phi_z + \phi_x - 3\theta + \psi_2\right) + C_3 \cos\left(2\phi_z - \phi_x + \psi_3\right)\right]. \quad (2.36)$$

When this procedure is completed, as a summary the results are:

$$H_{res} \approx G_0 J_z^2 + Q J_z^2 \cos\left(4\phi_z - 3\theta + \psi_0\right), \quad (2.37)$$

$$H_{coupl} \approx J_x^{\frac{1}{2}} J_z \left[C_1 \cos\left(\phi_x + \psi_1\right) + C_2 \cos\left(2\phi_z + \phi_x - 3\theta + \psi_2\right) + C_3 \cos\left(2\phi_z - \phi_x + \psi_3\right)\right], \quad (2.38)$$

where G_0, Q, ψ_0, and the set (C_j, ψ_j) for $j = 1, 2, 3$ are all constants which are defined above and numerical values are given in the following sections.

To see how slowly these terms vary, consider the tune values for a case that will be discussed later in considerable detail: $\nu_z = 0.740$ and $\nu_r = 1.129$, which occur at 34.8 MeV/u. In this case, the cosine term in Eq. 2.37 has the (zero-order) frequency: $(3 - 4\nu_z) = 0.040$. The corresponding frequencies of the three terms in Eq. 2.38 are: $\nu_r = 1.129$, $(3 - 2\nu_z - \nu_r) = 0.391$, and $(2\nu_z - \nu_r) = 0.351$. These frequencies are obviously much greater than the 0.040 in the resonant term, but in spite of this, the coupling terms play an important role in the $\nu_z = 3/4$ resonance (as will be seen below), and this is presumably because they are of lower order.

Chapter 3

Comparison of theory and orbit computations

In this chapter, we compare the results obtained from the Z^{2N} Orbit Code with $N = 2$ and those obtained from the Hamiltonian derived in the previous chapter. To emphasize the difference between the new and old orbit codes, we called the new one the Z^{2N} Orbit Code with $N = 2$ to distinguish it from the old Z^4 Orbit Code. Further information about the new code can be found in Chapter 4.

3.1 Study of $\nu_z = 3/4$ resonance at $\nu_z = 0.740$

Consider first the results obtained from the simple theory of the $\nu_z = 3/4$ resonance, assuming it is "isolated". In this case, the Hamiltonian is obtained by combining Eq. 2.22 and Eq. 2.37, that is,

$$H_\theta \approx \nu_z J_z + G_0 J_z^2 + Q J_z^2 \cos\left(4\phi_z - 3\theta + \psi_0\right), \tag{3.1}$$

where the values of the constants depend on the energy chosen.

We find that the "tune-shifting" term $G_0 J_z^2$ is positive and, moreover, $G_0 > Q > 0$, so that the resonance produces no instability. More specifically, the phase space diagram shows four stable as well as four unstable fixed points for $\nu_z < 3/4$, but none

at all for $\nu_z > 3/4$. In addition, the theory shows that these fixed points have the following angle and action values:

$$\cos\left(4\phi_z - 3\theta + \psi_0\right)_{fp} = \pm 1, \tag{3.2}$$

and

$$\left(J_z\right)_{fp} = \left(3/4 - \nu_z\right)/2\left(G_0 \pm Q\right), \tag{3.3}$$

where the $+(-)$ sign applies to the unstable (stable) fixed points. These conclusions are in good qualitative agreement with the computational results given below.

Although the theory is expressed in terms of angle and action variables, the input/output of the Z^{2N} Orbit Code are in terms of $(r,\, p_r)$ or $(x,\, p_x)$. In order to make direct comparisons, the orbit code results are translated into ϕ's and J's by using the inverse of the transformation Eq. 2.20 together with the definitions of Π_z and Π_x in Eq. 2.21. We should also note that for linear motion, $2\pi J$ is the invariant area of an eigenellipse, and we will therefore use

$$\rho = (2J)^{\frac{1}{2}} \tag{3.4}$$

as a "radius" in phase space. In the phase space diagrams presented here, we plot $\rho \sin\phi$ vs. $\rho\cos\phi$ since such plots provide the symmetric diagrams shown in theoretical papers [7, 8, 9]. Moreover, for linear motion, such a plot yields a circle of radius ρ.

As an example, take the case where $(3/4 - \nu_z) = 0.010$ occurring at 34.8 MeV/u. Here, numerical analysis yields the following values of the constants:

$$(G_0, Q) = (9.75, 3.42) \times 10^{-5}\,(\mathrm{mm})^{-2}, \tag{3.5}$$

and

$$\psi_0 = -44.3^{\circ}. \tag{3.6}$$

All of the orbit computations reported on here start with various initial values of $(z,\ p_z)$, but with initial $(r,\ p_r)$ values always on the EO in order to avoid added complications. The two z-space diagrams shown in Fig. 3.1 were obtained by plotting points once per sector at $\theta = 2\pi n/3$. The diagram at the top came from the output of the Z^{2N} Orbit Code with $N = 2$ while the diagram at the bottom was derived from the simple Hamiltonian in Eq. 3.1. The two diagrams are plotted to the same scale and as can be seen, the fixed points in the top diagram are closer to the origin than those in the bottom one. The $(\rho_z,\ \phi_z)$ coordinates of the fixed points in the first quadrant have the following values:

$$(\rho_z, \phi_z)_u = \begin{cases} (6.13 \text{ mm},\ 9.7 \text{ deg}) \\ (8.72 \text{ mm},\ 11.1 \text{ deg}) \end{cases} \tag{3.7}$$

$$(\rho_z, \phi_z)_s = \begin{cases} (10.6 \text{ mm},\ 54.1 \text{ deg}) \\ (12.6 \text{ mm},\ 56.1 \text{ deg}) \end{cases} \tag{3.8}$$

where the subscripts "u" and "s" refer to the unstable and stable fixed points, and where the top and the bottom lines on the right give the values obtained from the top and the bottom diagrams in Fig. 3.1. The fractional difference in the ρ_z for stable (unstable) fixed point is 19 % (42 %).(Actually, the bottom values are derived from the formulas in Eq. 3.2 and 3.3 above with the given ν_z value.)

In addition to the significant differences in the fixed point locations, the plots obtained from the orbit code (especially those near the stable fixed points) show a complicated fine structure that is completely missing from the theoretical plots.

To see if the differences between the theoretical results and those from the Z^{2N} Orbit Code with $N = 2$ can be traced to the third-order coupling terms, consider next the complete theoretical Hamiltonian obtained by combining Eq. 2.22, 2.37, 2.38. Again using as an example the numerical constants determined analytically for 34.8

MeV/u where $\nu_z = 0.740$, this Hamiltonian becomes:

$$\begin{aligned} H_\theta &= \nu_z J_z + \nu_r J_x + J_z^2 \left[9.75 + 3.42\cos\left(4\phi_z - 3\theta - 44.3°\right)\right] \times 10^{-5} \\ &\quad + J_x^{\frac{1}{2}} J_z \left[5.65\cos\left(\phi_x - 77.4°\right) + 7.19\cos\left(2\phi_z + \phi_x - 3\theta - 146.2°\right)\right. \\ &\quad \left. + 4.30\cos\left(2\phi_z - \phi_x + 104.4°\right)\right] \times 10^{-3}. \end{aligned} \tag{3.9}$$

Evidently, when $J_x = 0$, this H_θ reduces to that in Eq. 3.1 with the constants given in Eq. 3.5 and 3.6.

The equations of motion derived from H_θ in Eq. 3.9 can be integrated and the results compared to those obtained from the Z^{2N} Orbit Code with $N = 2$. Such a comparison is shown in the phase space diagrams presented in Fig. 3.2 with the orbit code results given at the top and the theoretical results given at the bottom, just as in Fig. 3.1. But here in Fig. 3.2, we restrict ourselves to phase plots for three particular orbits that have special interest. Plot # 1 circulates around the stable fixed points coming close to the separatrices and the unstable fixed points; this plot closes in about 200 turns. Plot # 2 resembles a flower with many petals that encloses each of the stable fixed points; this plot requires about 180 turns. (These two plots are also shown at the top of Fig. 3.1.) Finally, plot # 3 (which runs about 100 turns) is a small blur of points that are as close as one can get to the stable fixed points. Comparison of the diagrams in Figs. 3.2 and 3.1 clearly shows that the qualitative and quantitative agreement between the theoretical and orbit code results is significantly improved by inclusion of the coupling terms in the Hamiltonian.

This conclusion is reinforced by the evidence presented in Fig. 3.3 which show the x-space phase plots associated with the three orbits whose z-space plots are given in Fig. 3.2. Here, the three plots on the left come from the Z^{2N} Orbit Code with $N = 2$ while those on the right come from the theoretical results. The good agreement between these results is quite impressive. One should keep in mind that all

of these plots are simply two-dimensional projections of the four-dimensional phase space trajectories traced out by the three orbits.

As a test of the quantitative agreement between the two sets of results, we again compare the locations of the fixed points shown in the two diagrams of Fig. 3.2. Using the same notation as in Eq. 3.7 and 3.8 above for the data in Fig. 3.1, we now find:

$$(\rho_z, \phi_z)_u = \begin{cases} (6.13 \text{ mm}, 9.7 \text{ deg}) \\ (6.85 \text{ mm}, 10.0 \text{ deg}) \end{cases} \tag{3.10}$$

$$(\rho_z, \phi_z)_s = \begin{cases} (10.6 \text{ mm}, 54.1 \text{ deg}) \\ (12.7 \text{ mm}, 56.4 \text{ deg}) \end{cases} \tag{3.11}$$

where the top and bottom numbers represent the orbit code and theoretical results, respectively. The fractional difference in the ρ_z for the stable (unstable) fixed point is 20 % (12 %). Comparison with the data in Eq. 3.7 and Eq. 3.8 above shows that including the coupling effects provides a very significant improvement in the location of the unstable fixed points, but practically no change at all in the location of the stable fixed points. The accuracy of the theory is, of course, limited by its reliance on an expansion of the Hamiltonian in Eq. 2.9 with many "small" terms omitted.

It should also be pointed out that in producing the diagrams shown in Figs. 3.2 and 3.3, we used slightly different initial conditions for the two sets of orbits. As noted in the beginning of section 3.1, all of the Z^{2N} Orbit Code runs were started with (r, p_r) values on the EO so that initially, $x = p_x = 0$. But since $\Pi_x = p_x + qA_r$, and since $A_r \neq 0$ for $z \neq 0$, the initial values of Π_x and hence J_x and ρ_x differ from zero. In all cases reported here, computer runs based on the theory were started with the same values of (ρ_x, ϕ_x) as those from the Z^{2N} Orbit Code with $N = 2$. However, the initial values of (ρ_z, ϕ_z) for the theory runs were changed slightly so as to match as well as possible the resultant phase plots with those obtained from the Z^{2N} Orbit

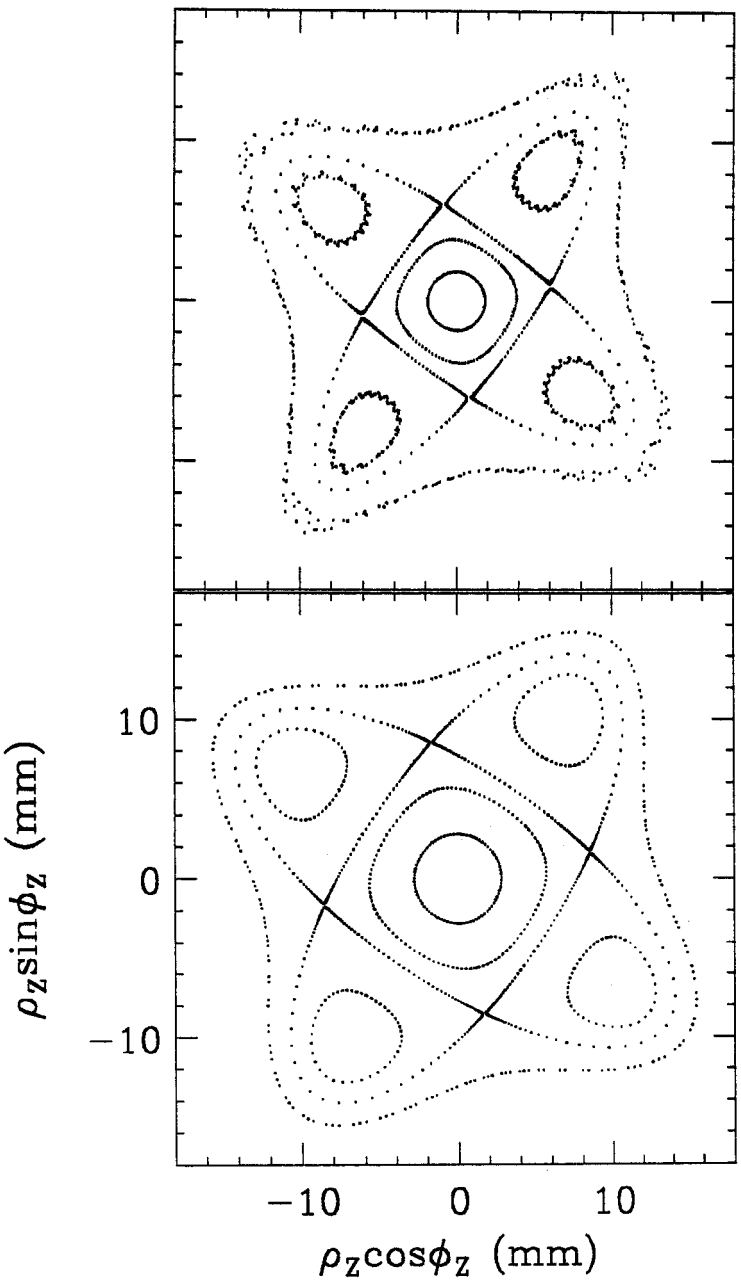

Figure 3.1: Two z-space diagrams at $\nu_z = 0.740$ ($E = 34.8$ MeV/u) obtained by plotting $\rho_z \sin\phi_z$ vs. $\rho_z \cos\phi_z$ once per sector for two sets of five orbits. One set (shown at top) is obtained from the Z^{2N} Orbit Code with $N = 2$ and the other set (shown at bottom) is derived from the simple Hamiltonian in Eq. 3.1 with its constants evaluated at the given energy. The simple theory obviously fails to reproduce quantitatively the results from the orbit code, including the location of the fixed points. It also fails to account for the fine structure in the phase plots from the orbit code which, as shown below, are produced by the coupling effects. Note that (ϕ, J) are angle-action variables and that $\rho = (2J)^{1/2}$ corresponds to a "radius" in phase space.

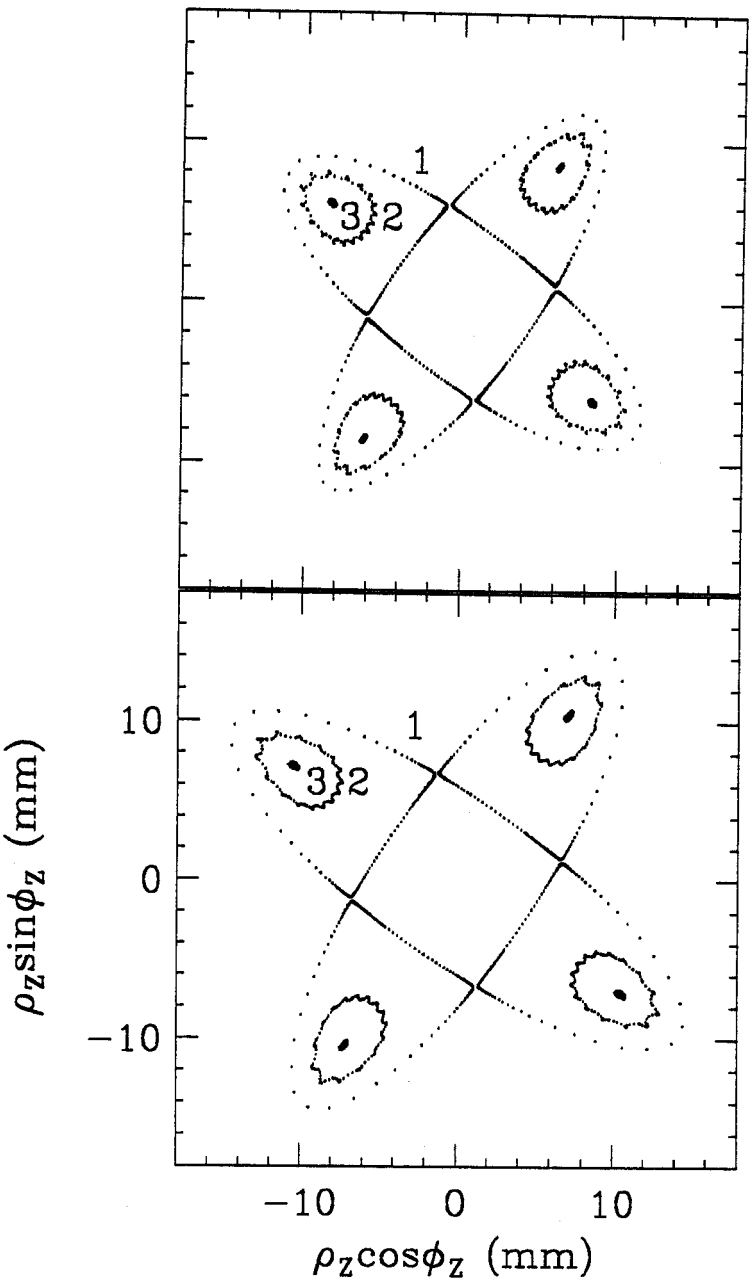

Figure 3.2: Two z-space diagrams (just like those in Fig. 3.1) for two sets of three orbits obtained by plotting once per sector, again at 34.8 MeV/u where $\nu_z = 0.740$. The set at the top was obtained using the Z^{2N} Orbit Code with N=2, while the set at the bottom was derived from the Hamiltonian in Eq. 3.9 that includes the third-order coupling terms. In contrast to the comparable situation in Fig. 3.1, the results presented here show that this Hamiltonian provides a relatively good explanation of the orbit code results, including the location of the fixed points and the fine structure in the phase plots. Note that all the orbits from the Z^{2N} Orbit Code with $N = 2$ reflect coupling effects. Unlike the situation predicted by the simple theory in Fig. 3.1, the stable and unstable fixed points are not sharply defined due to the coupling effects.

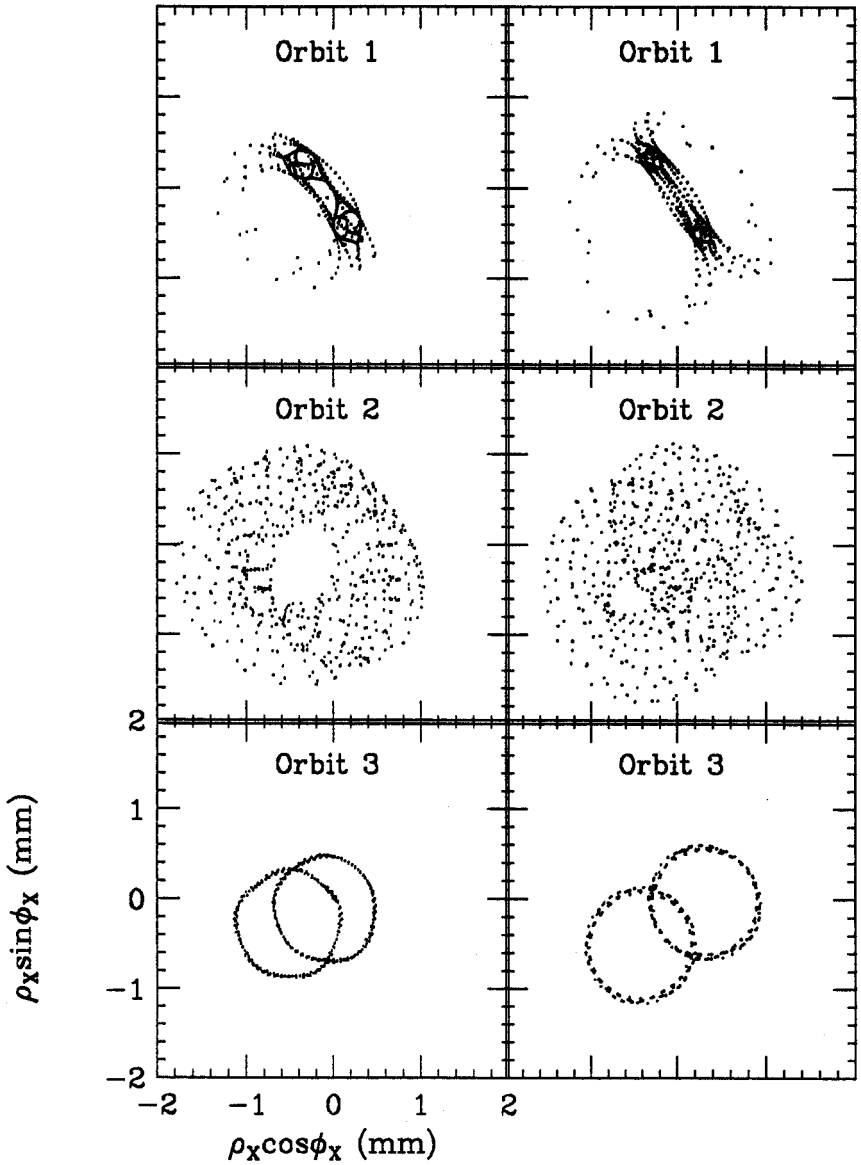

Figure 3.3: Six x-space phase plots obtained by plotting $\rho_x \sin\phi_x$ vs. $\rho_x \cos\phi_x$ once per sector for the same two sets of three orbits whose z-space phase plots are shown in Fig. 3.2. The three plots on the left were obtained using the Z^{2N} Orbit Code with $N = 2$, while the three on the right were derived from the Hamiltonian in Eq. 3.9 that includes the third-order coupling terms. The orbits labeled 1, 2, and 3 in Fig. 3.2 appear here at the top, center, and bottom, respectively. Since all of the orbits start with $(r,\ p_r)$ values on the equilibrium orbit, the phase plots here demonstrate the coupling of the z-motion into the x-motion. Moreover, the values of ρ_x here are an order of magnitude smaller than the values of ρ_z in Fig. 3.2 so that the coupling is not very strong. However, this coupling is quite significant and it is clear from a comparison of the two sets of phase plots that the theoretical Hamiltonian in Eq. 3.9 provides a good representation of the coupling effects found with the Z^{2N} Orbit Code with $N = 2$. Note that all six plots have exactly the same scales although only the one at the bottom left is labeled.

Code with $N = 2$. The size of this change for the orbit # 3 representing the stable fixed points can be gauged from the numbers given in Eq. 3.11; the changes for the other two orbits are about the same.

3.2 Study of $\nu_z = 3/4$ resonance at $\nu_z = 0.749$

Similar calculations were carried out for ($\nu_r = 1.136$, $\nu_z = 0.749$) at 35.5 MeV/u to see if the third-order coupling terms still play an essential role just as in the case for $\nu_z = 0.740$. One difference from the $\nu_z = 0.740$ case is that the scale of the major features of z-space diagrams are reduced by about three times compared with those for $\nu_z = 0.740$. Because $3/4 - \nu_z = 0.001$ is ten times smaller than $3/4 - 0.740 = 0.01$ for $\nu_z = 0.740$, the subsequent values of $(J_z)_{fp}$ is reduced by a factor of ten approximately, assuming the other constants remain about the same (refer to Eq. 3.3). So $(\rho_z)_{fp}$ is reduced by about three times.

Assuming again the $\nu_z = 3/4$ resonance is "isolated", the Hamiltonian without the coupling terms is:

$$H_\theta = \nu_z J_z + J_z^2 \left[11.0 + 3.98 \cos\left(4\phi_z - 3\theta - 45.5°\right)\right] \times 10^{-5}, \tag{3.12}$$

and the phase space diagram and its features can therefore be determined. Remembering that (G_0, Q)=$(9.75, 3.42) \times 10^{-5}$ and $\psi_0 = -44.3°$ for $\nu_z = 0.740$, the values for G_0 and Q for $\nu_z = 0.749$ are larger than those for $\nu_z = 0.740$ by 13 % and 16 % respectively and the value of ψ_0 differs by 1.2°.

Just as in the case for $\nu_z = 0.740$, all of the orbit computations reported on here start with various initial values of (z, p_z), but with initial (r, p_r) values always on the EO in order to avoid added complications. Figure 3.4 corresponds to Fig. 3.1 for $\nu_z = 0.740$ and shows two different z-dimension phase space diagrams. The diagram

at the top is obtained from the numerical orbit integration using the Z^{2N} Orbit Code with $N = 2$ and the bottom diagram is obtained by integrating the equations of motion derived from the Hamiltonian in Eq. 3.12. It should be noted that Fig. 3.4 uses two orbits while Fig. 3.1 uses five orbits. The diagrams in this figure are very similar to those in Fig. 3.1 except for the difference in the scale.

Again as a test of the quantitative agreement, the (ρ_z, ϕ_z) coordinates of the fixed points in the first quadrant are given here:

$$(\rho_z, \phi_z)_u = \begin{cases} (1.87 \text{ mm}, 9.9 \text{ deg}) \\ (2.59 \text{ mm}, 11.4 \text{ deg}) \end{cases} \tag{3.13}$$

$$(\rho_z, \phi_z)_s = \begin{cases} (3.24 \text{ mm}, 54.8 \text{ deg}) \\ (3.79 \text{ mm}, 56.4 \text{ deg}) \end{cases} \tag{3.14}$$

where the subscripts "u" and "s" refer to the unstable and stable fixed points, and where the top and the bottom lines on the right give the values obtained from the top and the bottom diagrams in Fig. 3.4. For the stable (unstable) fixed point, the values of ρ_z differ by 17 % (39 %) while they differ by 19 % (42 %) for the $\nu_z = 0.740$ case. (The bottom values are derived from the formulas in Eqs. 3.2 and 3.3 above with the given ν_z value just as in the case for $\nu_z = 0.740$.)

The fractional differences in the fixed point locations are almost equal. In addition to that, the plots obtained from the orbit code show a complicated fine structure because of the coupling between the z and x dimensions when the plots are magnified.

Now consider the complete theoretical Hamiltonian including the third-order coupling terms just as in the case of $\nu_z = 0.740$. Using the numerical constants determined analytically for 35.5 MeV/u where $\nu_z = 0.749$, this Hamiltonian becomes:

$$\begin{aligned} H_\theta &= \nu_z J_z + \nu_r J_x + J_z^2 \left[11.0 + 3.98 \cos\left(4\phi_z - 3\theta - 45.5°\right)\right] \times 10^{-5} \\ &\quad + J_x^{\frac{1}{2}} J_z \left[5.78 \cos\left(\phi_x - 79.0°\right) + 7.37 \cos\left(2\phi_z + \phi_x - 3\theta - 154.9°\right)\right. \end{aligned}$$

$$+ 4.48 \cos(2\phi_z - \phi_x + 107.8°)] \times 10^{-3}. \tag{3.15}$$

Compared with the corresponding values of C_j and ψ_j for $\nu_z = 0.740$, the values of C_j differ by at most 4 % and the values of ψ_j vary by 1.6°, 8.7°, and 3.4° respectively for $j = 1, 2, 3$.

Similar comparisons between theory and orbit computations are shown in the phase space diagrams presented in Fig. 3.5, which corresponds to Fig. 3.2 with the orbit code results given at the top and the theoretical results given at the bottom. We restrict ourselves to three particular orbits, just as in Fig. 3.2. Plot # 1 closes in about 1800 turns. Plot # 2 requires about 400 turns. Finally, plot # 3 runs about 400 turns. It should be noted that in Fig. 3.2 for $\nu_z = 0.740$, it takes about 200 turns for plot # 1, about 180 turns for plot # 2, and about 100 turns for plot # 3. Because $\nu_z = 0.749$ is closer to the $\nu_z = 3/4$ resonance, it naturally takes more turns to close in. When considering only linear motion, it should take ten times more turns to close in than the case for $\nu_z = 0.740$. Comparison of the diagrams in Fig. 3.4 and Fig. 3.5 clearly shows that the qualitative and quantitative agreement between the theoretical and orbit code results is significantly improved by inclusion of the coupling terms in the Hamiltonian for $\nu_z = 0.749$, just as for $\nu_z = 0.740$.

Figure 3.6 which corresponds to Fig. 3.3 shows the two sets of three x-space phase plots associated with the corresponding orbits whose z-space plots are given in Fig. 3.5. The three plots on the left come from the Z^{2N} Orbit Code with $N = 2$ while those on the right from the theoretical results. Again the Hamiltonian with the coupling terms provides good agreement between these results. Except for the scale of the plots and the turn numbers, these plots are very similar to those in Fig. 3.3.

As a test of the quantitative agreement between the two sets of results, we again compare the locations of the fixed points shown in the two diagrams of Fig. 3.5. Using

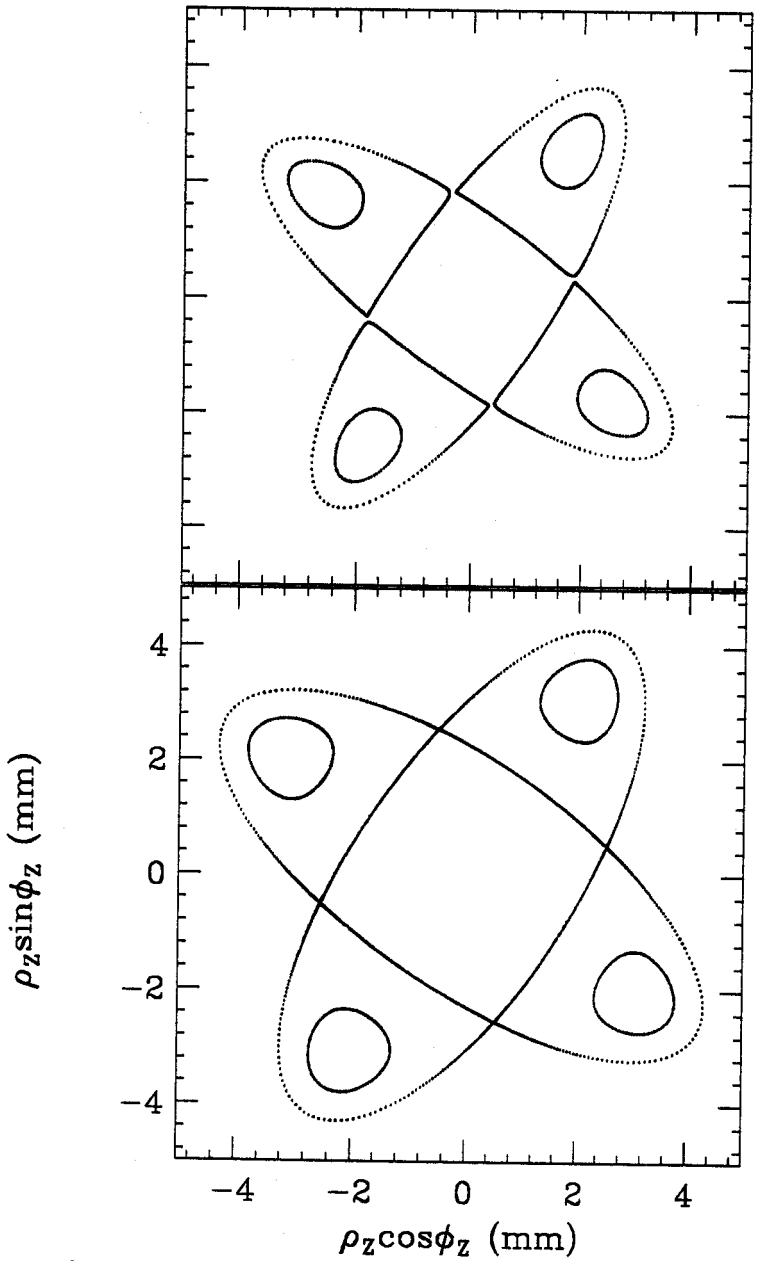

Figure 3.4: Two z-space diagrams at $\nu_z = 0.749$ ($E = 35.5$ MeV/u) for two sets of two orbits obtained by plotting $\rho_z \sin\phi_z$ vs. $\rho_z \cos\phi_z$ once per turn. These diagrams were obtained by plotting once per turn instead of once per sector as in Fig. 3.1, and the scale is 3.6 times smaller. One set (at the top) was obtained from the Z^{2N} Orbit Code with $N = 2$ and the other set (at the bottom) was derived from the simple Hamiltonian in Eq. 3.12. Unlike the plots in Fig. 3.1, the fine structure is not clearly observable to the eye. Otherwise, the plots are very similar except for the scale and the turn numbers of the orbits when compared with those in Fig. 3.1.

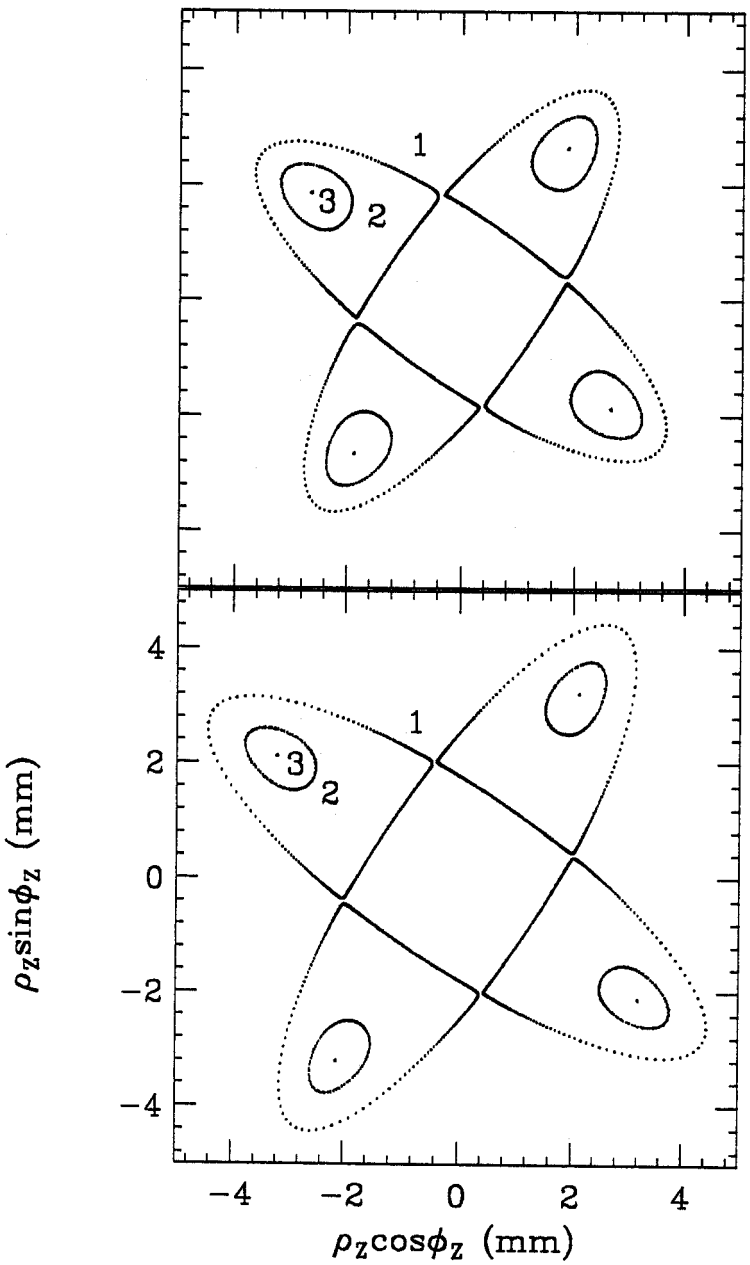

Figure 3.5: Two z-space diagrams (like those in Fig. 3.2) for two sets of three orbits obtained by plotting $\rho_z \sin\phi_z$ vs. $\rho_z \cos\phi_z$ once per turn at 35.5 MeV/u where $\nu_z = 0.749$. But Fig. 3.2 was plotted once per sector and its scale is 3.6 times larger. The set at the top was obtained using the Z^{2N} Orbit Code with $N = 2$, while the set at the bottom was derived from the Hamiltonian in Eq. 3.15 that includes the third-order coupling terms. The plots are very similar except for the scale and the turn numbers of the orbits compared with those in Fig. 3.2. Even though the fine structure may not be observable for the given scale, it becomes apparent when the plots are magnified.

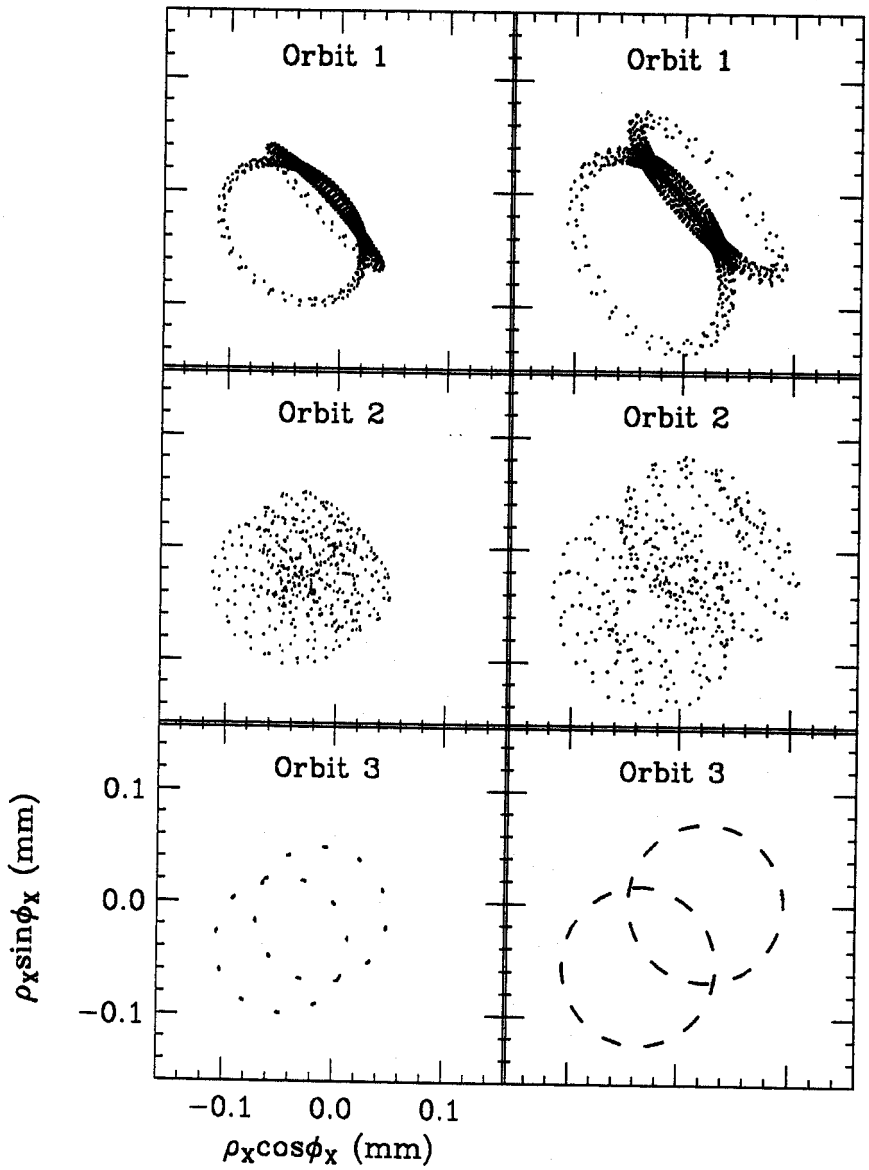

Figure 3.6: Six x-space phase plots (like those in Fig. 3.3) obtained by plotting $\rho_x \sin\phi_x$ vs. $\rho_x \cos\phi_x$ once per turn for the same two sets of three orbits whose z-space phase plots are shown in Fig. 3.5. But Fig. 3.3 was plotted once per sector and its scale is 12.5 times larger. Because ρ_x is proportional to ρ_z^2 and because ρ_z is reduced by about 3.2 times for $\nu_z = 0.749$ compared with that for $\nu_z = 0.740$, ρ_x is reduced by about ten times. The three plots on the left were obtained using the Z^{2N} Orbit Code with $N = 2$, while the three on the right were derived from the Hamiltonian in Eq. 3.15 that includes the third-order coupling terms. The orbits labeled 1, 2, and 3 in Fig. 3.5 appear here at the top, center, and bottom, respectively. The plots are very similar except for the scale and the turn numbers of the orbits compared with those in Fig. 3.3 for $\nu_z = 0.740$. Note that all six plots have exactly the same scales although only the one at the bottom left is labeled.

the same notation as in Eq. 3.13 and 3.14 above for the data in Fig. 3.4, we now find:

$$(\rho_z, \phi_z)_u = \begin{cases} (1.87 \text{ mm}, 9.9 \text{ deg}) \\ (2.05 \text{ mm}, 11.6 \text{ deg}) \end{cases} \tag{3.16}$$

$$(\rho_z, \phi_z)_s = \begin{cases} (3.24 \text{ mm}, 54.8 \text{ deg}) \\ (3.85 \text{ mm}, 56.6 \text{ deg}) \end{cases} \tag{3.17}$$

where the top and bottom numbers represent the orbit code and theoretical results, respectively. The fractional difference in the ρ_z for the stable (unstable) fixed point is 19 % (10 %) while the corresponding value for the stable (unstable) fixed point is 20 % (12 %) for $\nu_z = 0.740$. A comparison with the data in Eq. 3.13 and Eq. 3.14 above shows that including the coupling effects provides a very significant improvement in the location of the unstable fixed points, but little change in the location of the stable fixed points.

It should also be pointed out that in producing the diagrams shown in Fig. 3.5 and Fig. 3.6, we used again slightly different initial conditions for the two sets of orbits as in the case for $\nu_z = 0.740$. In all cases reported here, computer runs based on the theory were started with the same values of (ρ_x, ϕ_x) as those from the Z^{2N} Orbit Code with $N = 2$. However, the initial values of (ρ_z, ϕ_z) for the theory runs were changed slightly so as to match as well as possible the resultant phase plots with those obtained from the Z^{2N} Orbit Code with $N = 2$.

3.3 Conclusions

From the results of the two different cases for $\nu_z = 0.740$ and $\nu_z = 0.749$, we can conclude that the $\nu_z = 3/4$ resonance is not "isolated" and that the coupling terms have significant effects on the orbits. Moreover, the coupling effects between the z and x motion can be reproduced, within a reasonable accuracy, using only the most

slowly varying components of the lowest order coupling terms in the Hamiltonian. By inclusion of the coupling terms, both the qualitative and quantitative agreement between the Z^{2N} Orbit Code results and the theoretical results is significantly improved. In addition, the success of the theory here also provides evidence that the Z^{2N} Orbit Code is functioning properly.

Chapter 4

Effects of higher order terms

Up to this point, we have ruled out the effects of the terms of the magnetic field components which are of order higher than four in z. It's very important to decide whether it is worth going to the trouble of including higher order terms in orbit computations and hence at what order one can safely truncate the series. For the field components given in Eqs. 2.1- 2.5, the higher order increments up to z^8 are:

$$\Delta B_z = -\left[-\frac{z^6}{6!}\nabla_2^6 B + \frac{z^8}{8!}\nabla_2^8 B\right], \tag{4.1}$$

$$\Delta B_r = -\frac{\partial}{\partial r}\Delta C, \tag{4.2}$$

$$\Delta B_\theta = -\frac{\partial}{r\partial\theta}\Delta C, \tag{4.3}$$

with

$$\Delta C \equiv \frac{z^5}{5!}\nabla_2^4 B - \frac{z^7}{7!}\nabla_2^6 B. \tag{4.4}$$

Before setting out on actual comparisons based on orbit computations, there are several points we should note.

First of all, the representation for the magnetic field components assumes there are no sources (no singularities). As the value of z increases, one approaches various sources such as trim coils and pole face, and the representation becomes less appropriate. However, in actual operation of the K1200 superconducting cyclotron, the

maximum vertical displacement of beam, z_m, is usually limited to be $z_m < 5$ mm, while the height of the liner is about 19 mm. Because the effects of higher order terms of the magnetic field components become significant only for large z amplitudes, higher order terms beyond a certain order can be neglected without making much difference if one is interested in motion within a z_m much less than the magnet gap.

Secondly, including higher order terms requires more orbit computation time and more memory capacity of a computer. Determining the lowest possible order of truncation is therefore crucial in the light of cost-effectiveness.

Effects of the terms of the magnetic field components that are of order higher than four were studied by comparing the results of orbit computations obtained by using the magnetic field components up to z^6 or z^8 terms with those derived by using the magnetic field up to z^4. Three different calculations were carried out. One was carried out using an orbit with the same initial conditions as those of the orbit # 1 in the top diagram of Fig. 3.2. Another was done using an eigenellipse in z phase space at $E = 10$ MeV/u. This eigenellipse was accelerated until the energy of the central ray reached the final energy $E_f = 40$ MeV/u to see how much difference the higher order terms make. For both cases, the Z^{2N} Orbit Code was used with $N = 2$, $N = 3$, and $N = 4$ for comparison. And thirdly, a brief study of one of the sixth-order resonances, the $\nu_z = 3/6$ resonance, was carried out using the Z^{2N} Orbit Code with $N = 2$ and $N = 3$ to show the effects of higher order terms.

4.1 The Z^{2N} Orbit Code

Before the results are presented, a brief description of the orbit code used for the orbit computations is given here. The Z^{2N} Orbit Code is a modified version of the

Z^4 Orbit Code based on the development of new differentiation schemes using a finite difference technique as was pointed out in the beginning of Chapter 1 (for details, refer to the appendix). There are two differences between the two orbit codes.

One difference is that the Z^{2N} Orbit Code has an option specified by N while the Z^4 Orbit Code uses the magnetic field components only up to z^4 terms. For each choice of $N = 1, 2, 3,$ or 4, the magnetic field components up to z^{2N} terms are used. (For example, with $N = 2$, the magnetic field components up to z^4 terms are used, which corresponds to the Z^4 Orbit Code.) This option enables one to study nonlinear effects order by order.

The other difference is that the Z^{2N} Orbit Code uses the improved differentiators for evaluating various derivatives while the Z^4 Orbit Code utilizes the simple "old differentiators" (see Eqs. A.1 and A.2 in the appendix). In order to maintain consistency in differentiation, the Z^{2N} Orbit Code needs to store $3N$ maps of derivatives and a map of the midplane field data before orbit computations. For example, for $N = 1$, the Z^{2N} Orbit Code needs the maps of $\frac{\partial B}{\partial r}$ (related with B_r) and $\frac{\partial B}{r\partial \theta}$ (related with B_θ), in addition to the map of $\nabla_2^2 B$ (related with B_z). But the maps of $\frac{\partial B}{\partial r}$ and $\frac{\partial B}{r\partial \theta}$ are automatically computed and stored by a subroutine in the Z^{2N} Orbit Code when the map of B is given as an input. The Z^{2N} Orbit Code with $N = 2$ requires six maps of derivatives besides a map of the midplane field data, while the old Z^4 Orbit Code needs only two maps of derivatives plus the map of the midplane field data. Thus, improved accuracy in the evaluation of derivatives is achieved at the expense of computation time and memory space.

Except for the two differences mentioned above, the two nonlinear orbit codes are the same, including the use of exact equations of motion that can be derived from a Hamiltonian given in Eq. 2.9.

4.2 Effects of higher order terms on certain orbits

The orbit computation results presented in section 3.1 using the Z^{2N} Orbit Code with $N = 2$ reflect the effects of the magnetic field components only up to z^4. To see the significance of the higher order terms in the magnetic field components, we chose the orbits # 1 and # 3 in the top diagram of Fig. 3.2 and repeated similar calculations using the Z^{2N} Orbit Code with $N = 2$, $N = 3$, and $N = 4$. The orbit # 1 was chosen again because it defines the separatrices for the resonance and because of the existence of a chaotic layer surrounding the separatrices which greatly amplifies small differences in the orbits.

Figure 4.1 shows three z-space maps of orbits for which one can get as close as possible to the separatrices at $\nu_z = 0.740$ without jumping out of the island. These three maps were obtained by plotting $\rho_z \sin\phi_z$ vs. $\rho_z \cos\phi_z$ once per sector for 190 turns using the Z^{2N} Orbit Code with $N = 2$ (top diagram), with $N = 3$ (bottom left diagram), and with $N = 4$ (bottom right diagram). The orbit in the top diagram has the same initial conditions as those of the orbit # 1 in Fig. 3.2, which are ($z_0 = 3.9192$, $p_{z0} = 0$). But the corresponding initial conditions for the bottom left (right) orbit are ($z_0 = 3.9243$ (3.9522), $p_{z0} = 0$) for $N = 3$ ($N = 4$), which differ by less than 1 %. All these initial conditions are in units of mm. It should be noted that the basic features of the diagrams, such as the location of the unstable fixed points, remain almost unchanged even with inclusion of the terms of order higher than four in z to the magnetic field components. In these diagrams, the maximum ρ_z is 12 mm which corresponds to a maximum z value of 15 mm while, as noted above, the usual beam height $z_m = 5$ mm and the height of the liner is about 19 mm.

Figure 4.2 shows three maps of an orbit that has the same initial conditions as those of the orbit # 3 in the top diagram of Fig. 3.2. These were obtained by plotting

$\rho_z \sin\phi_z$ vs. $\rho_z \cos\phi_z$ at every sector $\theta = 2n\pi/3$ for 100 turns using three different options of the Z^{2N} Orbit Code with $N = 2$ (top diagram), $N = 3$ (bottom left diagram), and $N = 4$ (bottom right diagram). The length and width of the small blur of points expand by less than 1 % compared with the average ρ_z values of the points. It is clear from this figure that inclusion of higher order terms does not make a significant difference in the location of the "stable fixed points".

As a second investigation, we chose an eigenellipse in z phase space at $E = 10$ MeV/u at $\theta = 0°$ with emittance $2\pi J_z/p = 7.64$ πmm-mrad (assuming $p = 1.0$ m) and accelerated the orbits until the energy of the central ray reached $E_f = 40$ MeV/u in order to determine the integrated effects of higher order terms. Figure 4.3 portrays the resultant "ellipse" in z-phase space at every 10 MeV/u during the acceleration, which ran for 619 turns from 10 MeV/u to 40 MeV/u. Initially, all the points on the eigenellipse share the same values of (r_0, p_{r0}) which are on the accelerated equilibrium orbit. Figure 4.4 shows the corresponding x-phase space diagrams depicted at every 10 MeV/u. During the course of acceleration, the eigenellipse passes through various resonances depicted in Fig. 1.1 and some of these resonances couple the z-motion into the x-motion as shown in Fig. 4.4. (A similar calculation was performed over a limited range of energy across the $\nu_z = 3/4$, resonance and is presented in Figs. 1.2 and 1.3.)

Table 4.1 shows the rms differences in the final values of (z, p_z), (x, p_x), and (E, Φ) for the orbits at the final energy $E_f = 40$ MeV/u. The left and right columns show the rms differences in the results derived from the Z^{2N} Orbit Code with $N = 2$ and $N = 3$, and with $N = 2$ and $N = 4$, respectively. The final ellipse has $\Delta z = 8$ mm at $\theta = 0°$ and for all θ values, $\Delta z = 12$ mm, which is only 20 % greater than the assumed beam height $2z_m = 10$ mm. The rms differences listed in the table are negligible compared with the corresponding values.

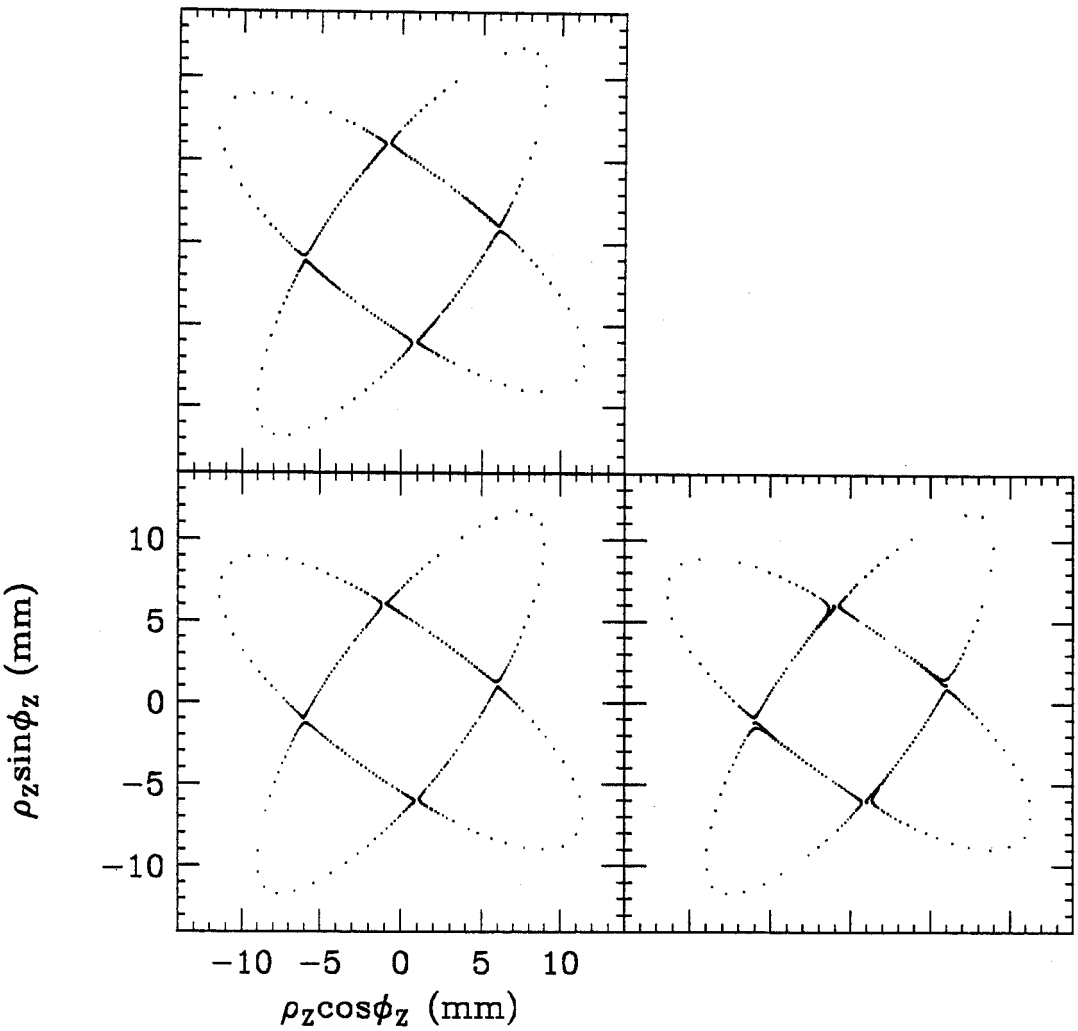

Figure 4.1: Three maps of orbits for which one can get as close as possible to the separatrices at $\nu_z = 0.740$ without jumping out of the island. These were obtained by plotting $\rho_z \sin\phi_z$ vs. $\rho_z \cos\phi_z$ at every sector $\theta = 2n\pi/3$ for 190 turns. The orbit at the top (with $N = 2$) has the same initial conditions as those of the orbit # 1 in the top diagram of Fig. 3.2, which are ($z_0 = 3.9192$, $p_{z0} = 0$). The orbit at the bottom left (right) has the initial conditions ($z_0 = 3.9243$ (3.9522), $p_{z0} = 0$) for $N = 3$ ($N = 4$). Here all the initial values are in units of mm. The variation in the initial conditions is less than 1 % and the basic features, such as the location of the unstable fixed points remain almost unchanged even with inclusion of higher order terms proportional up to z^6 and z^8.

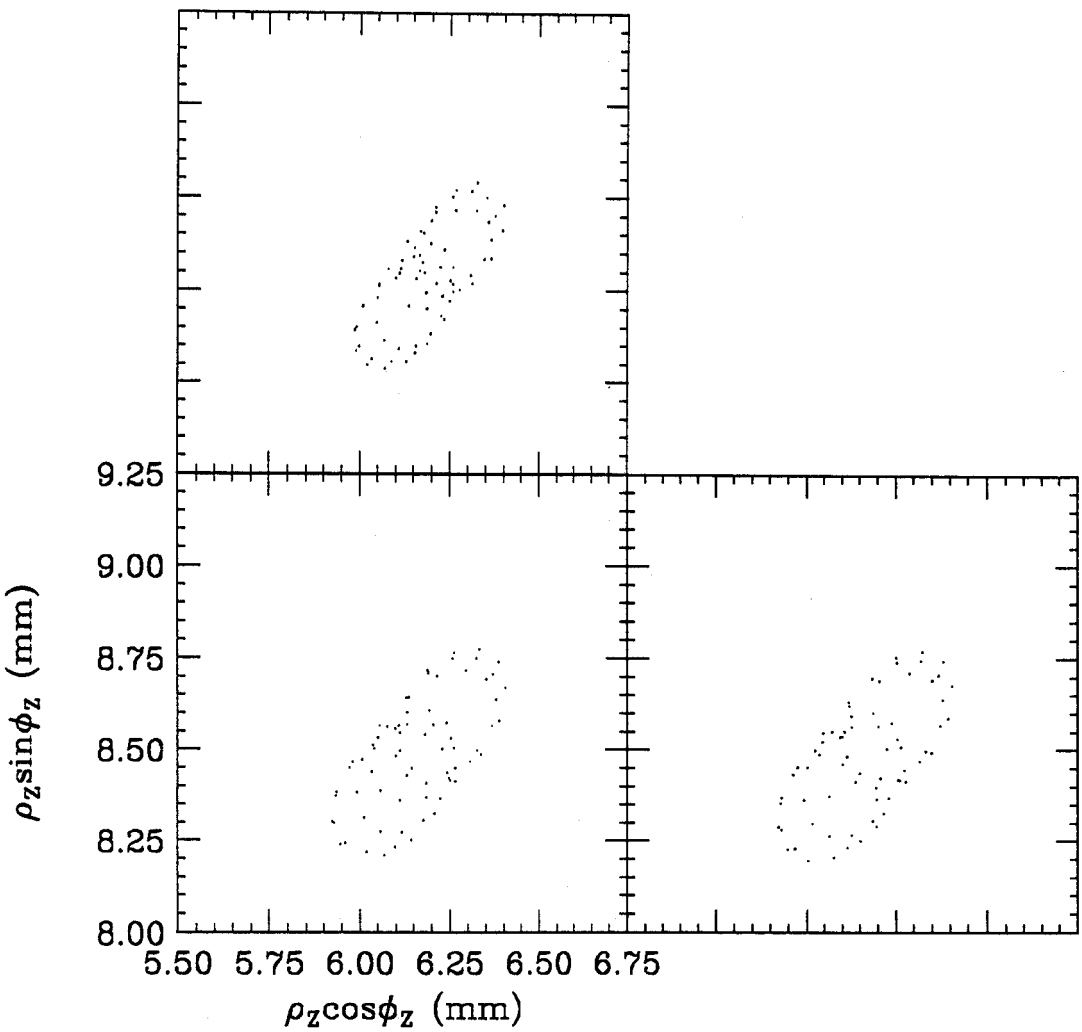

Figure 4.2: Three maps of an orbit that has the same initial conditions as those of the orbit # 3 in the top diagram of Fig. 3.2. These were obtained by plotting $\rho_z \sin\phi_z$ vs. $\rho_z \cos\phi_z$ at every sector $\theta = 2n\pi/3$ for 100 turns using the three different options of the Z^{2N} Orbit Code with $N = 2$ (top diagram), $N = 3$ (bottom left diagram), and $N = 4$ (bottom right diagram). The length and width of the small blur of points expand by less than 1 % compared with the average ρ_z values of the points. It is clear from this figure that inclusion of higher order terms does not significantly affect the location of the "stable fixed points".

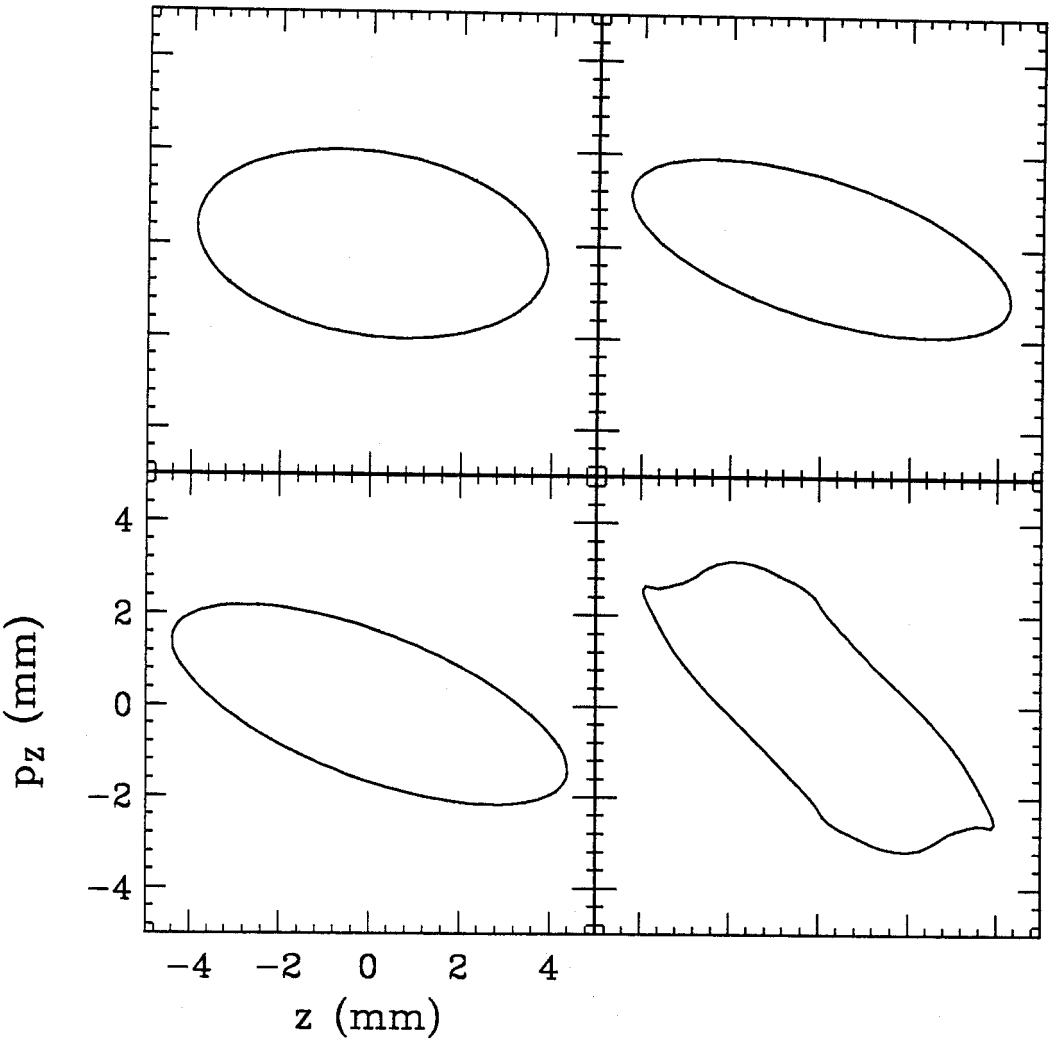

Figure 4.3: Evolution of an eigenellipse in z-phase space starting at 10 MeV/u (top left diagram) depicted at every 10 MeV/u during its acceleration for 619 turns after which the central ray reaches the final energy $E_f = 40$ MeV/u (bottom right diagram). These plots obtained by using the Z^{2N} Orbit Code with $N = 2$ show the evolution of the ellipse at 20 MeV/u (top right diagram), at 30 MeV/u (bottom left diagram) and at 40 MeV/u (bottom right diagram). It should be noted that the initial emittance is $2\pi J_z/p = 7.64$ πmm-mrad (assuming $p = 1.0$ m) for the initial eigenellipse at 10 MeV/u. (These diagrams should be compared with the those in Fig. 1.2 which are the results of a similar calculation.) Initially, all the points on the eigenellipse share the same values of (r_0, p_{r0}) which is on the accelerated equilibrium orbit at 10 MeV/u. The bottom right diagram is deformed appreciably due to the traversal of the $\nu_z = 3/4$ resonance between 30 MeV/u and 40 MeV/u. Almost exactly the same results were obtained with the $N = 3$, and $N = 4$ options for the Z^{2N} Orbit Code. (The same is true for the results in Fig. 4.4 below.)

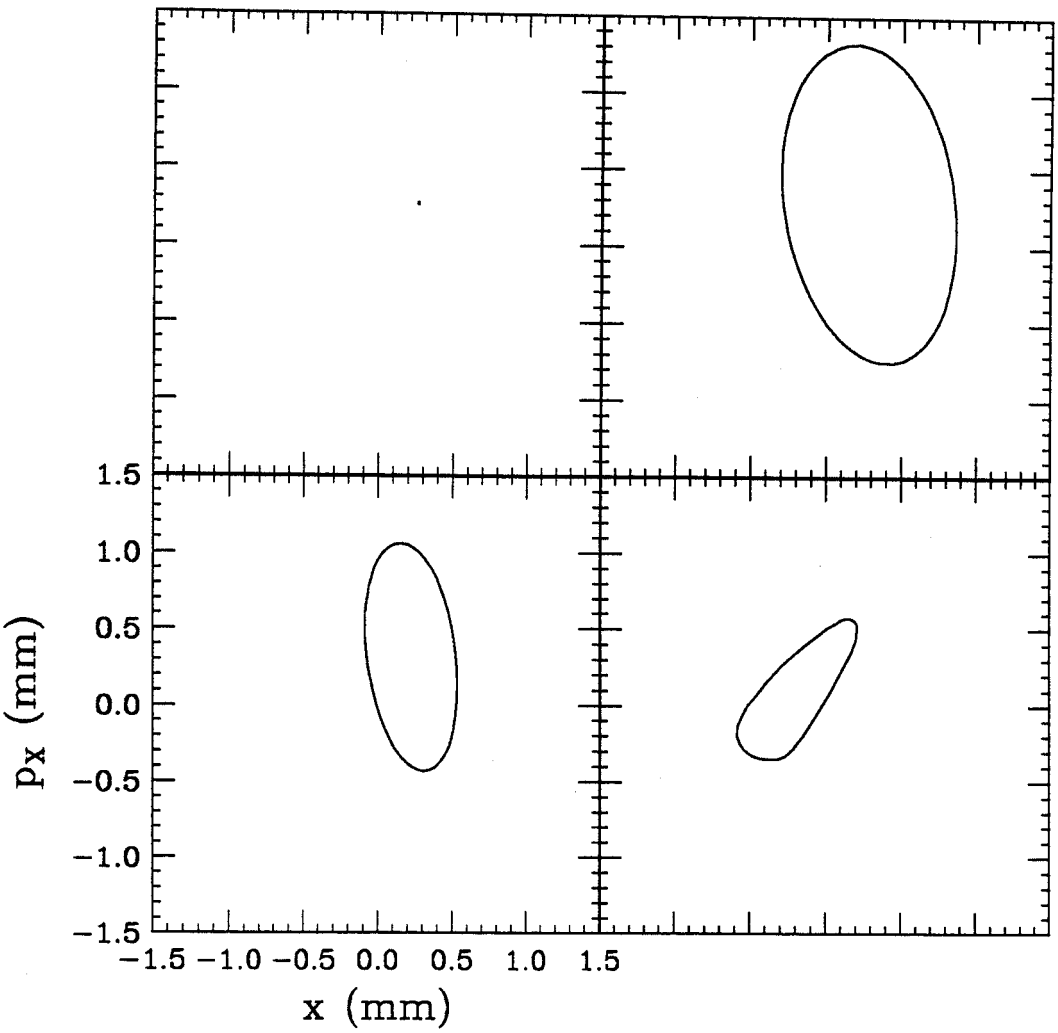

Figure 4.4: The evolution in x-phase space of the orbits in Fig. 4.3 obtained by using the Z^{2N} Orbit Code with $N = 2$. These plots show the evolution from 10 MeV/u (top left) to 20 MeV/u (top right) to 30 MeV/u (bottom left) to 40 MeV/u (bottom right). Initially, all the points share the same values of $(r_0,\ p_{r0})$ which are on the accelerated equilibrium orbit at $E = 10$ MeV/u (thus depicted as a point in top left diagram). Due to the traversal of the coupling resonances $2\nu_z = \nu_r$ and $2\nu_z + 2\nu_r = 3$ depicted in Fig. 1.1 between 10 MeV/u and 20 MeV/u, relatively large x-p_x spreads of $\Delta x \sim 1$ mm and $\Delta p_x \sim 2$ mm develop between the two top diagrams. Afterwards, the orbits do not cross any coupling resonances up to fourth order, and the area of the x-phase space diagram shrinks. These diagrams should be compared with those in Fig. 1.3.

Table 4.1: rms differences in orbit computations obtained from the Z^{2N} Orbit Code with $N = 2$ and $N = 3$, and with $N = 2$ and $N = 4$

	$N = 2$ and $N = 3$	$N = 2$ and $N = 4$
Δz	6.74×10^{-3} mm	6.81×10^{-3} mm
Δp_z	5.77×10^{-3} mm	5.80×10^{-3} mm
Δx	6.38×10^{-4} mm	6.53×10^{-4} mm
Δp_x	3.85×10^{-4} mm	4.01×10^{-4} mm
ΔE	1.72×10^{-2} keV	1.83×10^{-2} keV
$\Delta\Phi$	1.08×10^{-3} deg	1.14×10^{-3} deg

From the results shown in Figs. 4.1-4.4 together with Table 4.1, it can be concluded that the Z^{2N} Orbit Code with $N = 2$ can be used for all orbit computations relevant to the K1200 cyclotron. This restriction makes orbit computations relatively inexpensive as far as computing time and memory are concerned.

4.3 Effects of higher order terms on the $\nu_z = 3/6$ resonance at $\nu_z = 0.497$

The effects of higher order terms were studied near the $\nu_z = 3/6$ resonance at $\nu_z = 0.497$ with $E = 16.63$ MeV/u using the Z^{2N} Orbit Code with $N = 2$ and $N = 3$. The $\nu_z = 3/6$ resonance is at $E = 16.73$ MeV/u where $\nu_r = 1.070$. At $\nu_z = 0.495$, we could not find clear separatrices, and for ν_z values even closer to the resonance, it takes a large number of turns to get the results. Because of these reasons, $\nu_z = 0.497$ was chosen as a point in between. It should be noted that at $\nu_z = 0.50$, there are many overlapping resonances such as $\nu_z = 1/2$, $\nu_z = 2/4$, $\nu_z = 3/6$, and so forth. The $\nu_z = 3/6$ resonance is excited by the third harmonic component of the magnetic field which is one of the main harmonics of the K1200 superconducting cyclotron with three-fold symmetry in the magnet. On the other hand, the $\nu_z = 1/2$ resonance and the $\nu_z = 2/4$ resonance are generated by imperfection field components which

were excluded for this study by making the magnetic field symmetric for the sake of simplicity.

Figure 4.5 shows two z-space diagrams of an orbit obtained by plotting $\rho_z \sin\phi_z$ vs. $\rho_z \cos\phi_z$ once per sector. The top diagram was obtained by using the Z^{2N} Orbit Code with $N = 3$ for 1000 turns at ($\nu_r = 1.070$, $\nu_z = 0.497$) with $E = 16.63$ MeV/u. The initial conditions ($z_0 = 7.11$ mm, $\Pi_{z0} = 0$ mm) of this orbit were chosen in such a way that one can get as close as possible to the separatrices using the Z^{2N} Orbit Code with $N = 3$. The initial values (r_0, p_{r0}) are again on the EO to avoid added complexity.

The bottom diagram in Fig. 4.5 showing maps of two different orbits was derived from the Z^{2N} Orbit Code with $N = 2$. The inner orbit in bottom diagram obtained by running for 250 turns has the same initial conditions as those of the orbit in the top diagram. The outer orbit was derived by running 1300 turns in such a way that one can again get as close as possible to the separatrices. But it has different initial conditions, ($z_0 = 8.13$ mm, $\Pi_{z0} = 0$ mm).

The distinct features of a sixth-order resonance are observed for the top diagram which are composed of six islands and a central stable region. But the inner orbit, which has the same initial conditions as those of the orbit at the top, is still inside the central stable region. On the other hand, as is also depicted in Fig. 4.5, when the initial conditions are changed into ($z_0 = 8.13$ mm, $\Pi_{z0} = 0$ mm), the characteristic structure pertaining to the sixth-order resonance emerges here also. (See the outer orbit in the bottom diagram.) This originates from the z^6 terms coming from the terms proportional to A_r^2 or A_r^3 that are obtained when the square root term of the Hamiltonian in Eq. 2.9 is expanded, even though the magnetic field components contain terms only up to fourth-order in z. But the width of the six islands of the bottom diagram is less than that of the top diagram, which suggests a weaker driving

force for the $\nu_z = 3/6$ resonance in the case of the orbit at the bottom.

Due to coupling effects, the maps of the orbit in z-space have finite thickness and this thickness grows as the value of J_z grows. Figure 4.6 shows a diagram of the coupled motion in x-space for the orbit at the top in Fig. 4.5. The maximum value of ρ_x of the coupled motion is about 20 % of the maximum value of ρ_z, and this percentage is about two times larger than the ratio of the maximum value of ρ_x to that of ρ_z for the orbit # 1 in Fig. 3.3. Besides, all the unstable fixed points are fuzzier than for $\nu_z = 3/4$. All these results indicate that coupling effects are stronger here than for the $\nu_z = 3/4$ resonance.

From Figs. 4.5 and 4.6, it is interesting to find that even though all the sixth-order terms in the magnetic field components are omitted, the typical phase space structure for a sixth-order resonance emerges and that the value of ρ_z for the unstable fixed points differs only by 14% compared with the results obtained by using the magnetic field components up to z^6 terms. However, it is clear that one can not obtain accurate results for the $\nu_z = 3/6$ resonance without using the Z^{2N} Orbit Code with $N = 3$, at least.

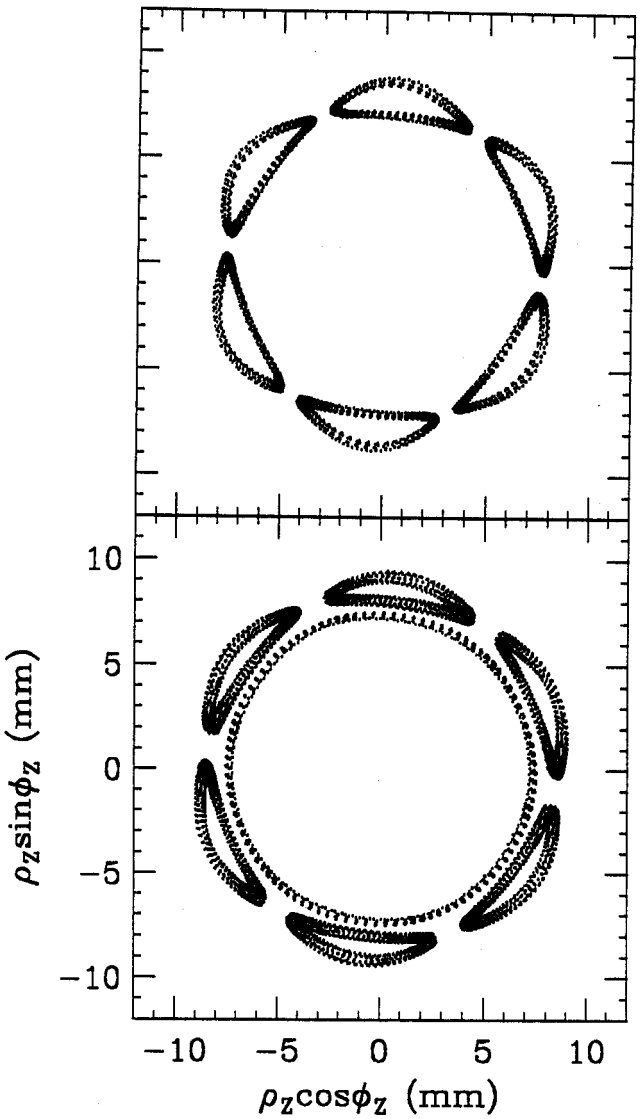

Figure 4.5: Two z-space diagrams for $\nu_z = 0.497$ at $E = 16.63$ MeV/u obtained by plotting $\rho_z \sin\phi_z$ vs. $\rho_z \cos\phi_z$ once per sector. The top diagram was obtained by using the Z^{2N} Orbit Code with $N = 3$ for 1000 turns with the initial conditions ($z_0 = 7.11$ mm, $\Pi_{z0} = 0$ mm). These are chosen in such a way that one can get as close as possible to the separatrices. The bottom diagram showing maps of two different orbits was derived from the Z^{2N} Orbit Code with $N = 2$. The inner orbit in the bottom diagram obtained by running for 250 turns has the same initial conditions as the top diagram. The outer orbit was derived by running 1300 turns with ($z_0 = 8.13$ mm, $\Pi_{z0} = 0$ mm). These turn numbers are required to make approximately one revolution in the diagram. Without the higher order terms in the magnetic field components, the inner orbit is still inside the central stable region without showing any sign of the sixth-order resonance. But as shown for the outer orbit, even with the magnetic field components containing terms only up to z^4, the typical phase space structure of a sixth-order resonance still emerges. Besides, all the unstable fixed points are fuzzier than those for the $\nu_z = 3/4$ resonance due to stronger coupling effects here.

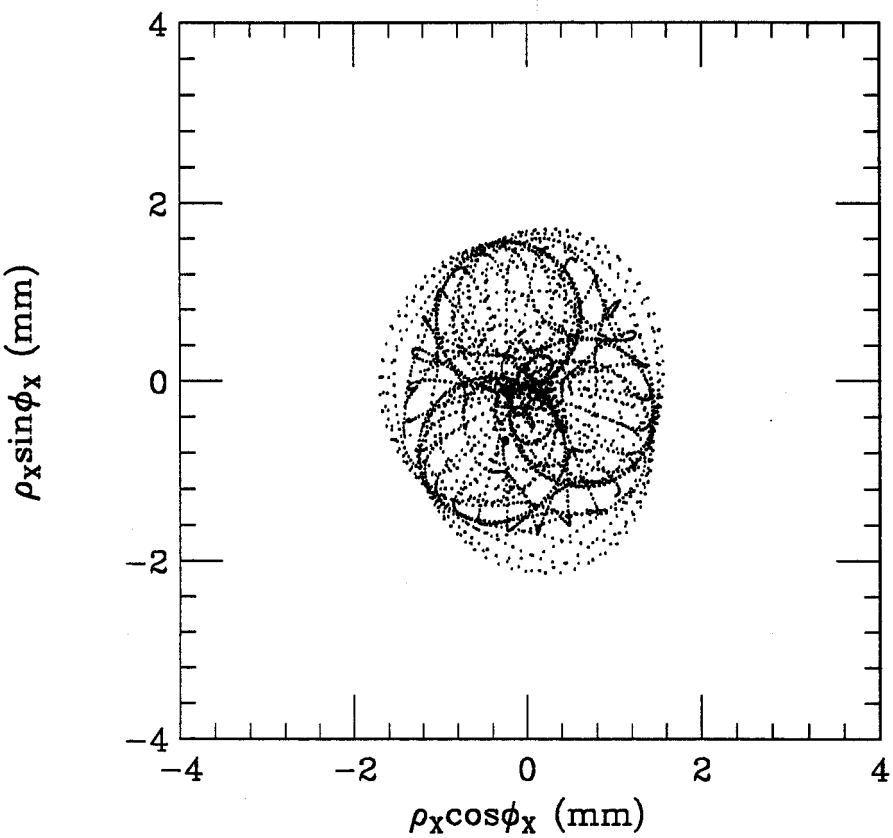

Figure 4.6: The x-space diagram showing the result of coupled motion in x space near the $\nu_z = 3/6$ resonance at $\nu_z = 0.497$ for the same orbit shown in the top diagram of Fig. 4.5. This was obtained by plotting $\rho_x \sin\phi_x$ vs. $\rho_x \cos\phi_x$ once per sector using the Z^{2N} Orbit Code with $N = 3$ for 1000 turns. The maximum value of ρ_x for this orbit is about 20 % of the maximum value of ρ_z, which is about two times larger than the ratio of the maximum value of ρ_x to that of ρ_z for the orbit # 1 in Fig. 3.3. This reflects stronger coupling effects here than for the $\nu_z = 3/4$ resonance.

Chapter 5

Comparison of old and new methods for computing field derivatives

Recently a new finite difference technique for evaluating the off median plane magnetic field components has been developed [3]. The main motivation was based on the observation that maps of the higher order terms in the magnetic field components obtained by using the "old differentiators" in the original Z^4 Orbit Code become increasingly more noisy. The objective was to design new differentiators to suppress noise effectively without destroying important components by maintaining reasonable accuracy over a sufficiently wide range of low frequencies. For a detailed discussion, refer to the appendix. In this chapter, some results on the comparison between the improved differentiators and the "old differentiators" are given.

As a direct test, we present maps of the second-order and fourth-order terms of B_z in Eq. 2.1 and the first-order term of B_r in Eq. 2.2 which are evaluated at $z = 0.5$ (in) by using the improved differentiators. We also present maps of the differences between these maps and those computed using the "old differentiators". In addition, as an indirect test, the results of orbit computations for three different orbits with distinct physical characteristics obtained from the Z^{2N} Orbit Code with $N = 2$ using

the improved differentiators are compared with those for the same three orbits derived from the Z^4 Orbit Code utilizing the "old differentiators". This is to show explicitly how a small amount of noise in the off median plane magnetic field components affects orbits when it is not suppressed effectively. It should also be pointed out that all the orbit computation results presented in the previous chapters were obtained by using the new Z^{2N} Orbit Code.

5.1 Application to K1200 cyclotron field

The magnetic field here is exactly the same as that used in the preceding chapters. The median plane field map was measured on a polar mesh with $\Delta\theta = 1°$ and $\Delta r = 0.1$ (in) while the pole radius is 42 (in). But for the orbit studies in Chapter 3, we used a field map restricted to the range from $r = 32$ (in) to $r = 40$ (in) and from $\theta = 0°$ to $\theta = 119°$. As shown in the appendix, the improved differentiators have a cutoff frequency $\omega_{cutoff} \approx 1.05$ and strongly suppress higher frequency signals. This cutoff frequency corresponds to the 20th harmonic obtained from a Fourier analysis of the field with perfect three-fold azimuthal symmetry. Moreover, the improved differentiators accurately evaluate the derivatives over a much broader range of low frequencies than the "old differentiators", while suppressing more effectively the high frequency signals associated with noise.

We have applied the improved differentiators and the "old differentiators" to evaluate the coefficients of the magnetic field components in Eq. 2.1 and Eq. 2.2 using the measured median plane magnetic field data shown in Fig. 5.1. The maximum and minimum field values here are 45 kG and 30 kG, respectively.

As an illustration, Fig. 5.2 shows at the top a map of the second-order term, $\nabla_2^2 B \times 0.5^2/2!$, evaluated at $z = 0.5$ (in) obtained by using the improved differentiators, and

the map of the difference at the bottom between this and the map for the same term obtained by utilizing the "old differentiators". The maximum and minimum of the map at the top for $\nabla_2^2 B \times 0.5^2/2!$ are (248 G, -352 G) respectively, and those of the difference map at the bottom are (13.0 G, -11.9 G). The map of the difference at the bottom shows the relative defects of the old differentiators in suppressing high frequency signals.

Similarly Fig. 5.3 shows, at the top, a map of the fourth-order term, $\nabla_2^4 B \times 0.5^4/4!$, evaluated at $z = 0.5$ (in) obtained by using the improved differentiators and at the bottom, a map of the difference between this and the map of the same term obtained by utilizing the "old differentiators". The maximum and minimum of the map at the top are (82.3 G, -104 G) respectively, and those of the difference map at the bottom are (33.9 G, -28.5 G). Because useful data which are slowly varying are washed out to an appreciable extent by the "old differentiators" when they are applied twice to get the fourth-order term, the values of the bottom map depicting the difference are significant compared with those of the fourth-order term itself. The amount of slowly varying components washed out by the old differentiators is so large compared with noise that it is difficult to observe rapidly varying noise compared with the case for the map portraying the difference in the second-order term shown in Fig. 5.2. Refer to Figs. A.10 and A.12 in the appendix for the wash out of physically important slowly varying components by the "old differentiators". For the case dealing with data with noise, refer to Figs. A.13 and A.14 in the appendix. As is discussed in detail in the appendix, the "old differentiators" are accurately evaluating derivatives only over a very limited range of low frequency.

Figure 5.4 shows the map of $\frac{\partial}{\partial r} zB$ evaluated at $z = 0.5$ (in) at the top which is the leading term of B_r in Eq. 2.2 obtained by using the improved differentiators, and at the bottom, a map of the difference between this and the map of the same

term obtained by using the old differentiators. The maximum and minimum values of $\frac{\partial}{\partial r}zB$ evaluated at $z = 0.5$ (in) are 1.96 kG and -1.92 kG respectively. This is the leading term of B_r, and B_r plays a dominant role compared with B_θ in the z focusing. Because of these reasons, $\frac{\partial}{\partial r}zB$ is a physically important term. The maximum and minimum values of the difference at the bottom are 14.7 G and -16.5 G respectively, and these values are less than 1 % compared with 1.96 kG and -1.92 kG. Just as in Fig. 5.2, the difference map shows the relative defects of the old differentiators in suppressing rapidly varying components of data.

5.2 Application to orbits near the $\nu_z = 3/4$ resonance

As an indirect test, comparison of the results of orbit computations was conducted near the $\nu_z = 3/4$ resonance at $\nu_z = 0.740$. Three different orbits were chosen. One set of orbit computations was carried out for the three orbits using the Z^{2N} Orbit Code with $N = 2$ and the other set of orbit computations was performed for the same three orbits using the old Z^4 Orbit Code.

One orbit exactly the same as # 1 in Fig. 3.2 was chosen again. This orbit is close to the separatrices and due to the chaotic layer, any kind of error in the computation can easily be amplified. Figure 5.5 shows clearly the difference in the orbit computation results which portray two maps of this orbit obtained by plotting $\rho_z \sin\phi_z$ vs. $\rho_z \cos\phi_z$ once per sector for 400 turns. The map at the bottom obtained from the Z^4 Orbit Code spirals inward and is asymmetric, while that at the top obtained by using the Z^{2N} Orbit Code with $N = 2$ exhibits a more physical behavior. It is remarkable that small differences in the various order terms of the magnetic field components can produce such a noticeable difference.

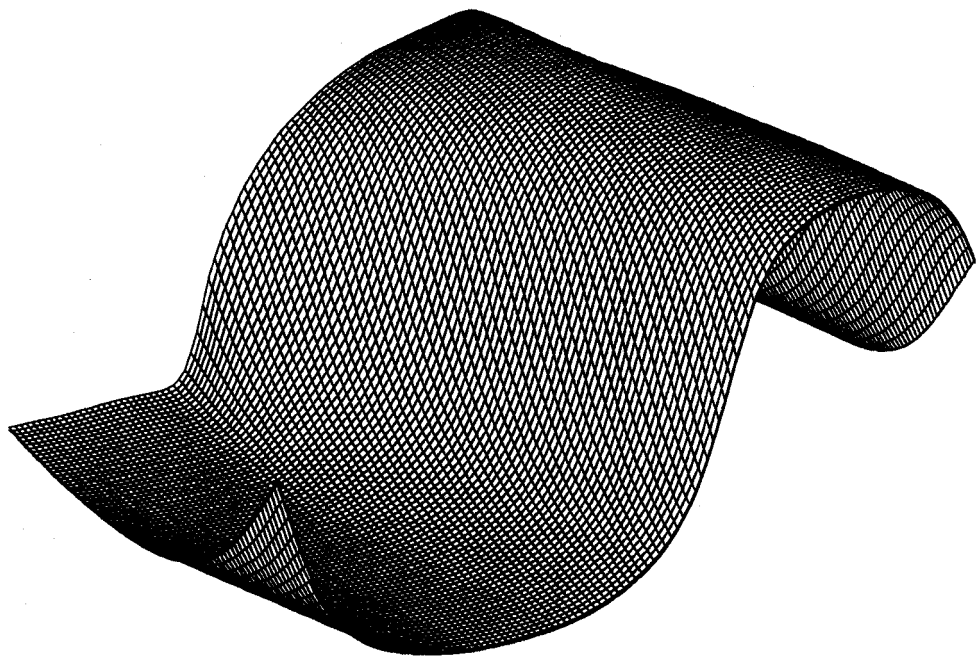

Figure 5.1: Map of $B(r,\theta) = -B_z(r,\theta,z=0)$ of a magnetic field of the K1200 superconducting cyclotron with $q/A = 0.25$ and a nominal final energy $E_f = 40$ MeV/u over the range 32 (in) $\leq r \leq$ 40 (in) and $0° \leq \theta \leq 119°$ used for orbit computations in the preceding chapters. This field has a perfect three-fold azimuthal symmetry. The maximum field value is 45 kG and the minimum is 30 kG. The magnetic field within this radius range is very nonlinear.

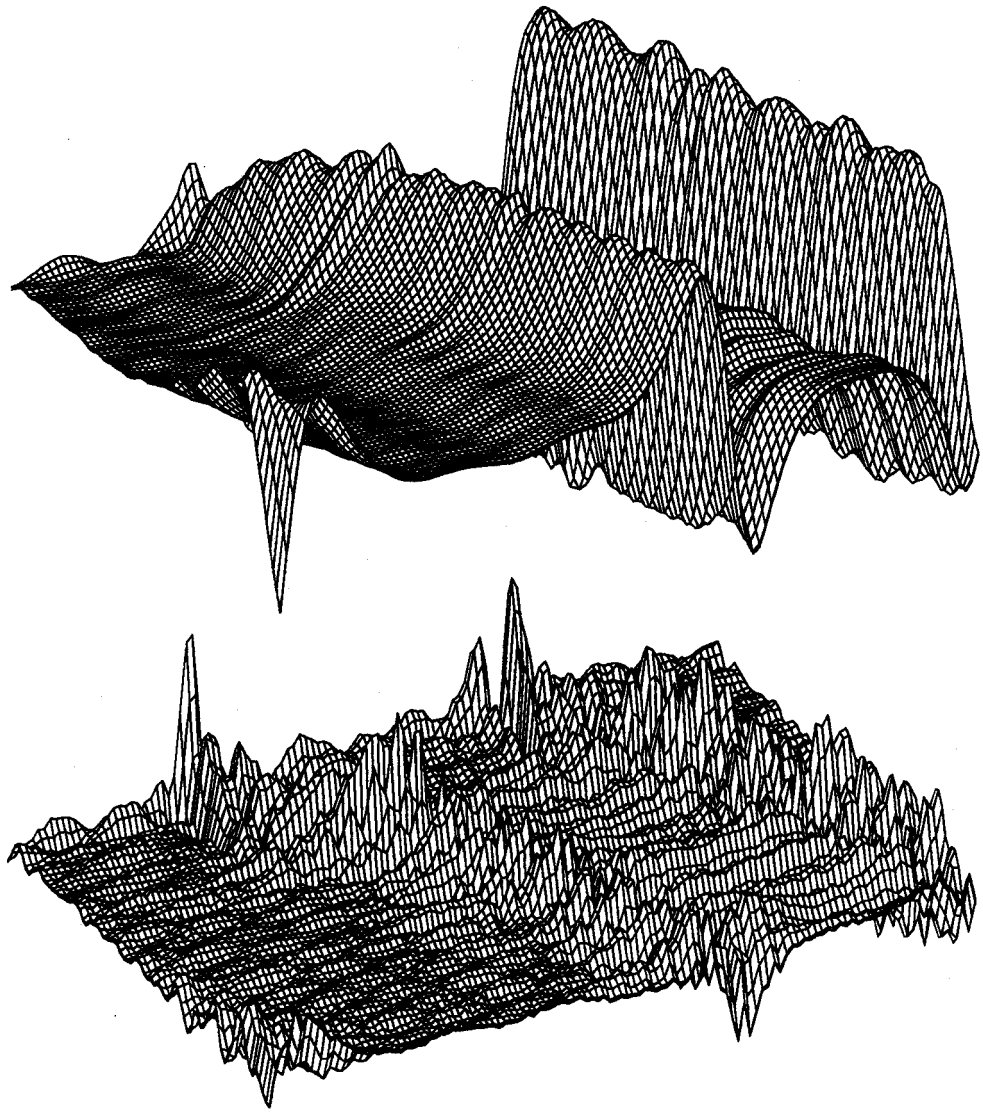

Figure 5.2: A map of $\nabla_2^2 B \times 0.5^2/2!$ evaluated at $z = 0.5$ (in) by using the improved differentiators (at the top) and a map of difference between this and the map for the same term computed using the "old differentiator" (at the bottom) for the magnetic field shown in Fig. 5.1. The maximum and minimum values of the map at the top are (248 G, -352 G) respectively while those of the difference map at the bottom are (13.0 G, -11.9 G). Note that the two maps are not plotted to the same scale. The map at the bottom depicting the difference shows the relative defects of the old differentiators in suppressing noise.

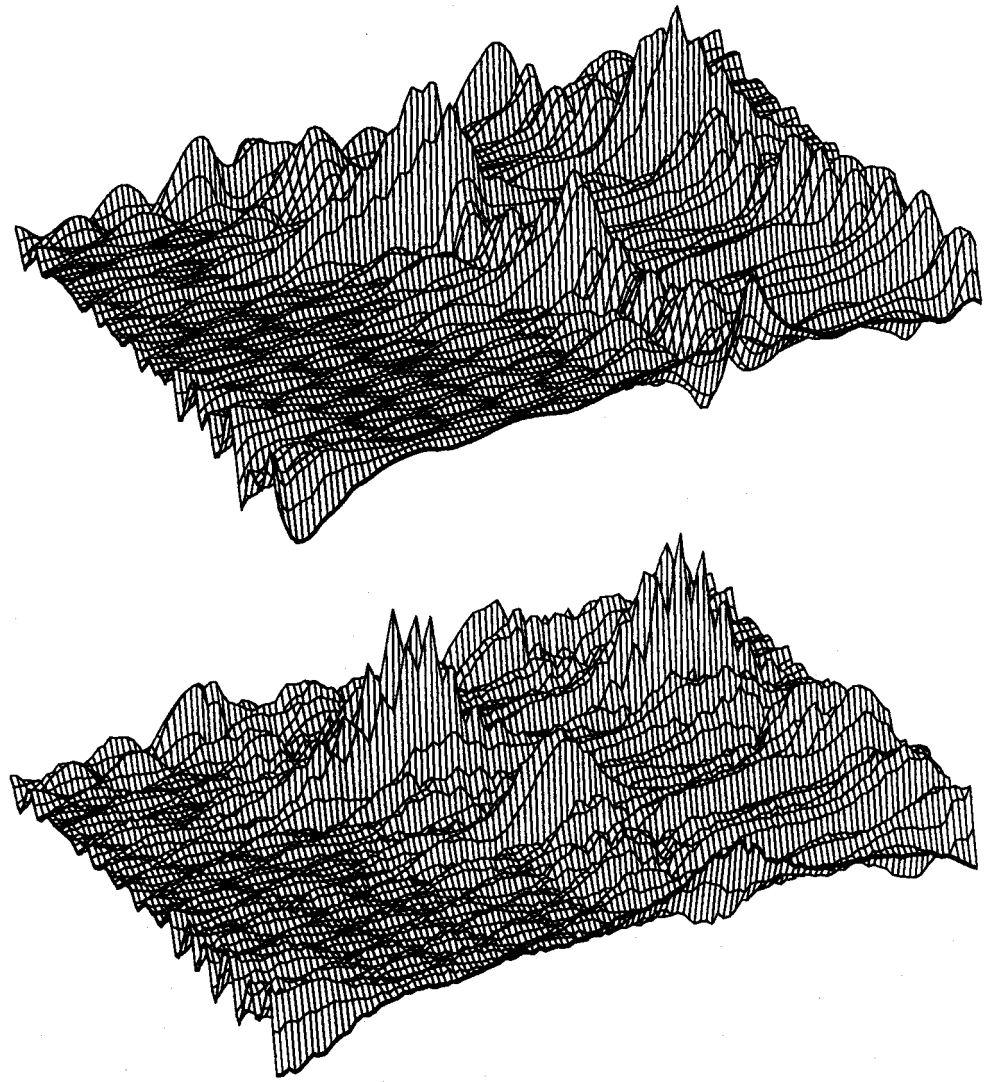

Figure 5.3: A map of $\nabla_2^4 B \times 0.5^4/4!$ evaluated at $z = 0.5$ (in) by using the improved differentiators (at the top) and a map of difference between this and the map for the same term computed using the "old differentiator" (at the bottom) for the magnetic field shown in Fig. 5.1. The maximum and minimum values of the map at the top are (82.3 G, -104 G) respectively while those of the difference map at the bottom are (33.9 G, -28.5 G). Note that the two maps are not plotted to the same scale. Because useful slowly varying components of data are washed out to an appreciable extent by the "old differentiators" when they are applied twice to get the fourth-order term, the values of the bottom map depicting the difference are significant compared with those of the fourth-order term itself at the top. (See Figs. A.10 and A.12 in the appendix for the wash-out of physically important slowly varying components of data.) Moreover it is not easy to observe the rapidly varying small noise because it is buried in the washed out data.

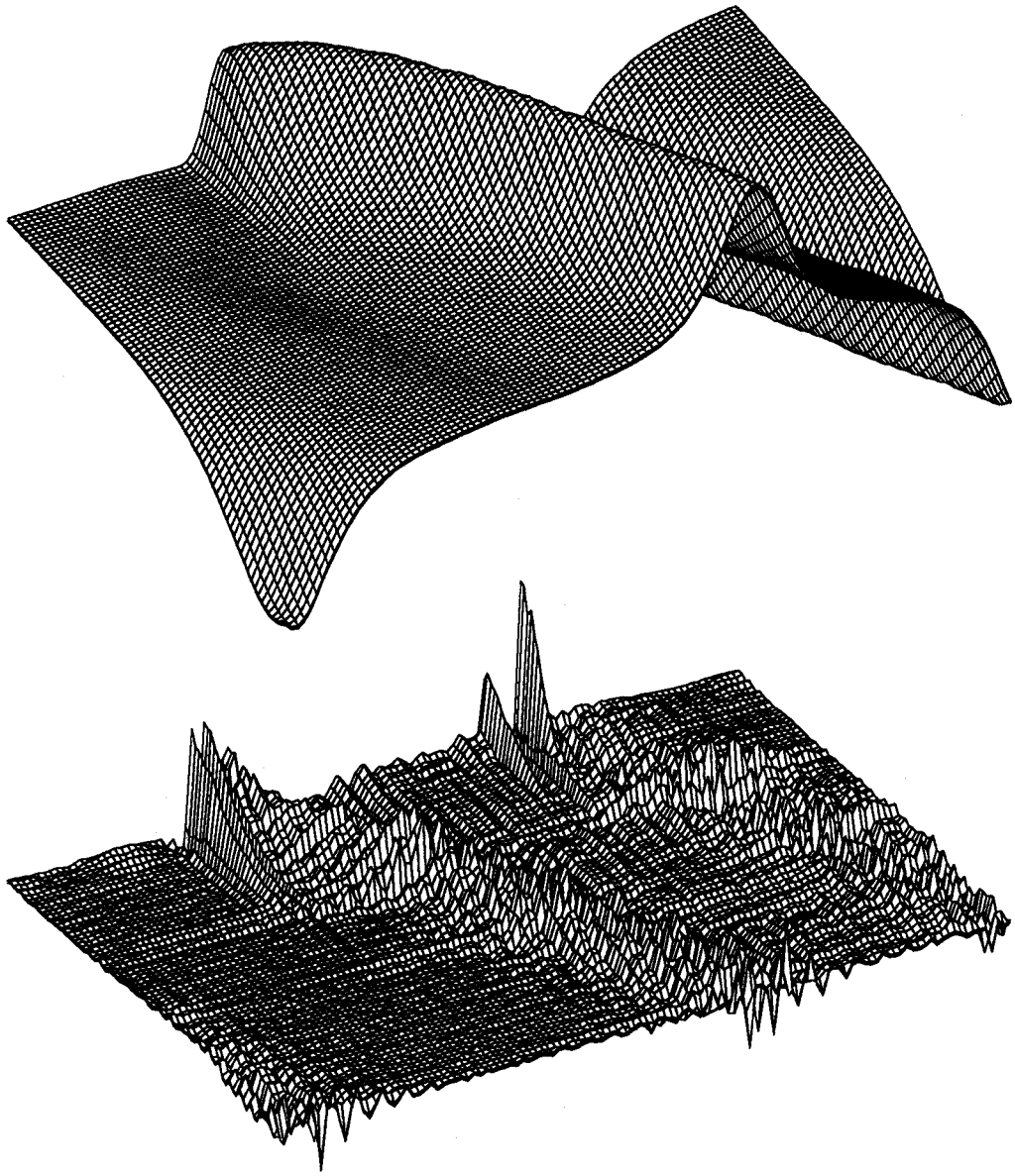

Figure 5.4: A map of $\frac{\partial}{\partial r}zB$ evaluated at $z = 0.5$ (in) by using the improved differentiators (at the top) and a map of difference between this and the map for the same term computed using the "old differentiator" (at the bottom) for the magnetic field shown in Fig. 5.1. This is the leading term of B_r and B_r plays a dominant role in z-focusing. The maximum and minimum values of the map at the top are (1.96 kG, -1.92 kG) respectively while those of the difference map at the bottom are (14.7 G, -16.5 G). Note that the two maps are not plotted to the same scale. The map at the bottom depicting the difference shows the relative defects of the old differentiators in suppressing noise.

Figure 5.6 shows two z-space diagrams of an orbit just outside of the separatrices obtained by plotting $\rho_z \sin\phi_z$ vs. $\rho_z \cos\phi_z$ once per sector for 500 turns. The diagram at the top was obtained by using the Z^{2N} Orbit Code with $N = 2$ and that at the bottom by using the old Z^4 Orbit Code for the same orbit. Highly chaotic characteristics are observed for the map derived from the Z^4 Orbit Code, which reflects the effects of remaining rapidly varying components of field data that were not effectively suppressed by the old differentiators.

Figure 5.7 shows two z-space diagrams of an orbit just inside the inner separatrix obtained by plotting $\rho_z \sin\phi_z$ vs. $\rho_z \cos\phi_z$ once per turn (instead of once per sector) for 1000 turns. The map at the top was obtained from the Z^{2N} Orbit Code with $N = 2$ and that at the bottom was derived from the Z^4 Orbit Code. The corresponding values of z_{max} and z_{min} are 5.3 mm and -5.3 mm. The bottom map of this orbit slowly spirals outward as the turn number increases, while the map at the top remains almost unchanged and shows more physical behavior. This results from a rather inaccurate evaluation of field derivatives and poor suppression of rapidly varying components of data by the old differentiators.

It turns out that noise in the calculated magnetic field components makes numerically computed orbits highly chaotic especially near the chaotic region. Without a proper handling of the noise inherent in the measured median plane magnetic field map, one can apparently obtain orbit computation results that appear unrealistic.

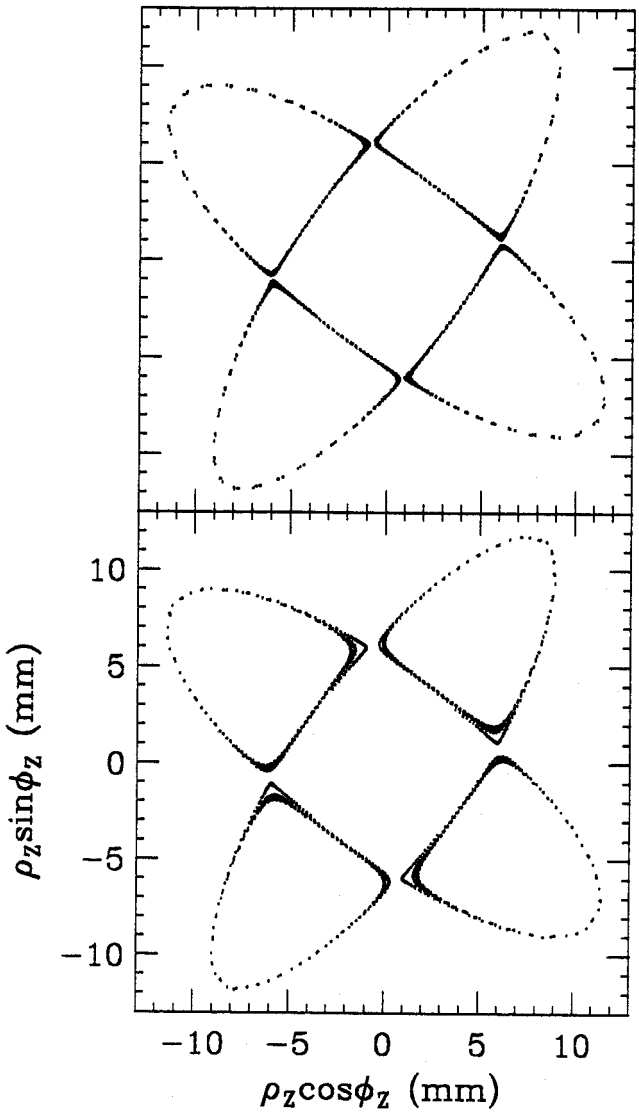

Figure 5.5: Two maps of an orbit close to the separatrix for $\nu_z = 0.740$ which is near the $\nu_z = 3/4$ resonance. This orbit has the same initial conditions as those of the orbit # 1 in top diagram of Fig. 3.2. These were obtained by plotting once per sector for 400 turns. Due to the chaotic layer on the separatrix, any kind of errors in orbit computations can be visualized with ease. The bottom diagram of this orbit obtained from the Z^4 Orbit Code using the "old differentiators" spirals inward and is asymmetric, while that obtained from the Z^{2N} Orbit Code with $N = 2$ exhibits more physical behavior (see the top diagram).

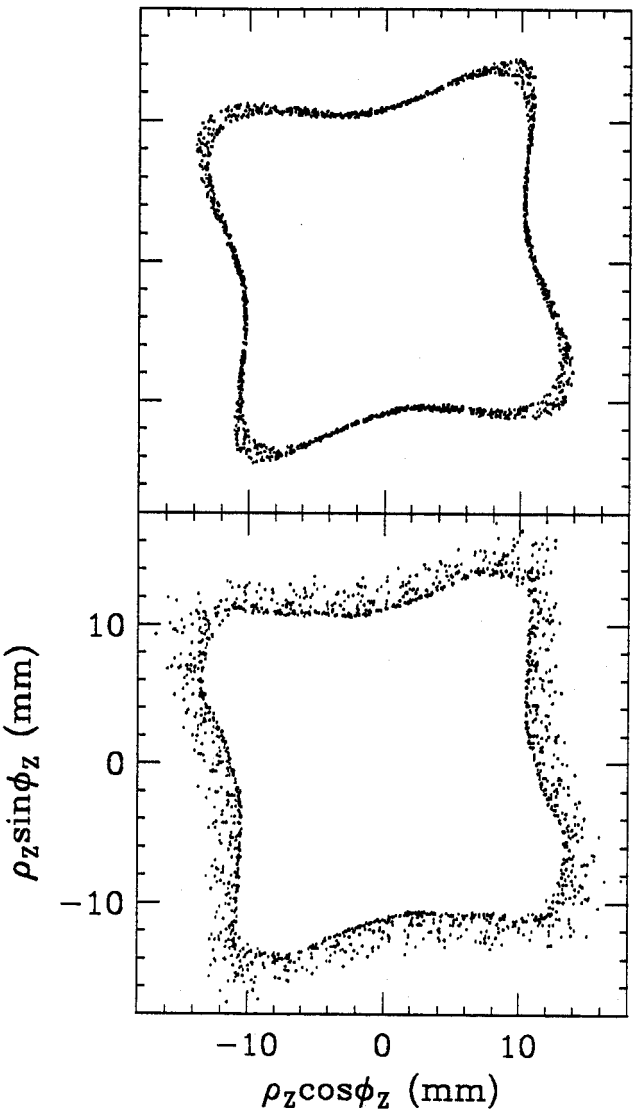

Figure 5.6: Two maps of an orbit in the z-dimensional phase space just outside the separatrices for $\nu_z = 0.740$ which is near the $\nu_z = 3/4$ resonance. The map at the top was obtained from the Z^{2N} Orbit Code with $N = 2$ and that at the bottom by using the Z^4 Orbit Code for the same orbit. These diagrams were obtained by plotting once per sector for 500 turns. The map at the bottom shows highly chaotic behavior, which is a result of poor suppression of noise in numerical computation of magnetic field components by the "old differentiators".

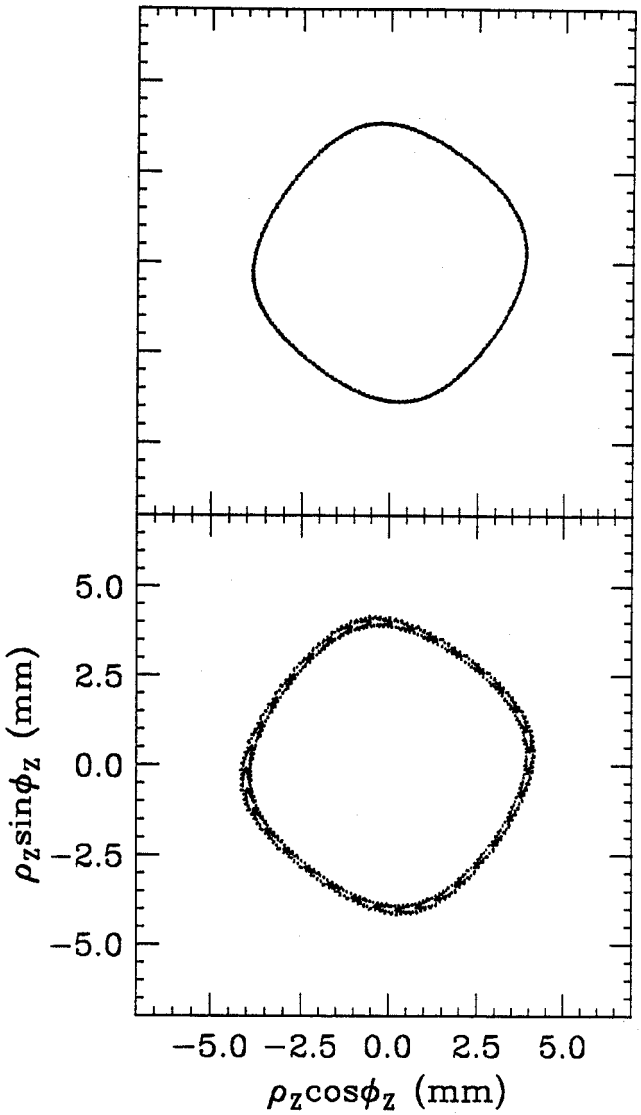

Figure 5.7: Two maps of an orbit in the z-dimensional phase space just inside the inner separatrix for $\nu_z = 0.740$ which is near the $\nu_z = 3/4$ resonance. The map at the bottom was obtained from the Z^4 Orbit Code and that at the top was derived from the Z^{2N} Orbit Code with $N = 2$ for the same orbit. These were obtained by plotting once per turn (instead of once per sector) for 1000 turns. The map at the bottom slowly spirals outward while that at the top remains almost the same.

Appendix A

Finite difference method for calculating magnetic field components off the median plane using median plane data

Gordon and Taivassalo [1, 14] evaluated the coefficients in Eqs. 2.1- 2.3 using the second-order central difference scheme as follows:

$$f_i' = (f_{i+1} - f_{i-1})/2\Delta \tag{A.1}$$

$$f_i'' = (f_{i+2} + f_{i-2} - 2f_i)/4\Delta^2 \tag{A.2}$$

where $f_i = f(x_i)$ and Δ is the step size of the mesh. These are what we call the old differentiators which are used by the Z^4 Orbit Code. This scheme presents difficulties both in accuracy and maximum order of expansion due to amplified noise produced by taking derivatives. By "noise", we mean any high frequency components like those usually associated with noise.

In an effort to overcome the difficulties, new differentiators using a finite difference technique were developed and we call them the "improved differentiators". Here, a detailed description is presented.

The finite difference scheme, which is a special case of the compact finite difference

scheme, is used to avoid additional complexity imposed by compact schemes. If one wants to enhance accuracy, a plausible way would be to use compact finite difference schemes. A lot of work has been done for compact finite difference schemes [15, 16, 17, 18], and work for non-uniform mesh has also been done [19, 20]. Especially Lele [18] did recent work on compact finite difference schemes. Even though the operators designed by Lele have a frequency response reasonably close to that of mathematical differentiation over the complete frequency range, they are not adequate for processing measured data containing noise because sufficient suppression of high frequency signals is not provided.

The frequency ω which is going to be used extensively later is defined as follows. Let's suppose there is a uniform mesh and a sinusoidal signal e^{ikx} is applied to it where k is the wavenumber. When the distance between two consecutive mesh points is Δ, the subsequent phase advance is $k\Delta$. Thus we define $\omega \equiv k\Delta$. So the largest ω without the problems of "aliasing" is π.

There are two possible ways to compute derivatives of a magnetic field. One way to do so is to process a magnetic field with a certain filter to remove high frequency components before taking any derivatives. If the undesirable high frequency components are suppressed to a satisfactory extent, comparatively simple and standard differentiators can be used for computing derivatives. The other way is to mix processes of computing derivatives and filtering. We decided to take the latter approach for the following reasons. First of all, there are many orbit codes used in this laboratory (and many other laboratories) to calculate various orbit properties which do not require any of the off median plane magnetic field components, but only the median plane field map itself, and all the researchers in this laboratory prefer having the field data unaltered for orbit computations. Secondly, it is vital to preserve the consistency between the results obtained by the orbit codes using only the unprocessed median

plane field map and those obtained by the nonlinear orbit codes utilizing both the median plane field map and the off median plane field components.

We will use a composite operator of more than two finite difference operators that use only three nodes. In this case, the use of separate algorithms to evaluate derivatives at nodes near the boundaries can be avoided by imposing simple conditions for each 3-node operator. The following property is useful to get the frequency response of composite operator obtained in this way.

Let's consider a composite operator of two linear operators $L_1 = \sum h_1(n) f_n$ and $L_2 = \sum h_2(m) g_m$ with the corresponding frequency response H_1 and H_2. Then the frequency response of the composite operator of these two is $H_1 H_2$, which is independent of the ordering of application of the linear operators. If one considers the properties of Z transformations [21, 22], it is straightforward to verify the previous statements. We are going to use this for the design of the operators.

A.1 Design of the first and second order differentiators in one dimension

The standard second-order central difference scheme composed with a filter is used to improve the frequency response of differentiators. The use of such a filter is to provide a strong suppression of high frequency signals and by adjusting a parameter Q of the filter, to improve the low frequency response at the same time.

First of all, the filter F is introduced that transforms $\{f_n\}$ to $\{\hat{f}_n\}$ suppressing high frequency signals. For the first-order and the second-order differentiator, the parameter Q is adjusted respectively to produce a reasonable result. It is given below:

f_n, for $n = 0, \ldots, N+1$

$$\Downarrow$$

$$g_n = \left(f_{n-1} + 2f_n + f_{n+1}\right)/4$$

$$g_0 = f_0, \quad g_{N+1} = f_{N+1}$$

$$\Downarrow$$

$$h_n = g_n - \frac{Q}{4}\left(g_{n-1} + g_{n+1} - 2g_n\right)$$

$$h_0 = g_0, \quad h_{N+1} = g_{N+1}$$

$$\Downarrow$$

$$k_n = \left(h_{n-1} + 2h_n + h_{n+1}\right)/4$$

$$k_0 = h_0, \quad k_{N+1} = h_{N+1}$$

$$\Downarrow$$

$$\hat{f}_n = k_n - \frac{1}{4}\left(k_{n-1} + k_{n+1} - 2k_n\right)$$

$$\hat{f}_0 = k_0, \quad \hat{f}_{N+1} = k_{N+1}.$$

The frequency response $H^{(F)}$ of the filter is as follows:

$$H^{(F)}(\omega) = \left[\cos^2(\omega/2) + \frac{Q}{4}\sin^2(\omega)\right]\left[\cos^2(\omega/2) + \frac{1}{4}\sin^2(\omega)\right]. \tag{A.3}$$

The improved first-order differentiator is a combination of the central difference scheme (refer to Eq. A.1) and a filter, which ends up with being an eleven-point formula. With the choice of $Q = 1.70$, reasonable low frequency response was obtained for the first-order differentiator. More detailed discussion about the choice $Q = 1.70$ is given at the section for resolving efficiency. The operator $D^{(1)}$ which approximates first-order derivative $\{\frac{d}{dx}f(x_n)\}$ for $n = 1, \ldots, N$ from a given set of data $\{f_n = f(x_n)\}$ for $n = 0, \ldots, N+1$ is as follows:

$$f_n, \text{ for } n = 0, \ldots, N+1$$

$$\Downarrow$$

$$d_n = (f_{n+1} - f_{n-1})/2\Delta, \text{ for } n = 1, \ldots, N$$

$$\Downarrow$$

$$s_n = (d_{n+1} + 2d_n + d_{n-1})/4$$

$$s_1 = d_1, \quad s_N = d_N$$

$$\Downarrow$$

$$g_n = s_n - \frac{1.7}{4}(s_{n+1} + s_{n-1} - 2s_n)$$

$$g_1 = s_1, \quad g_N = s_N$$

$$\Downarrow$$

$$h_n = (g_{n+1} + 2g_n + g_{n-1})/4$$

$$h_1 = g_1, \quad h_N = g_N$$

$$\Downarrow$$

$$\frac{d}{dx}f(x_n) = h_n - \frac{1}{4}(h_{n+1} + h_{n-1} - 2h_n)$$
$$\frac{d}{dx}f(x_1) = h_1, \quad \frac{d}{dx}f(x_N) = h_N.$$

Complete expression of the operator $D^{(1)}$ is applied for the nodes with $n = 5$ to $n = N - 4$ but we can still get good evaluation of derivatives for the rest of nodes at the same time. It is convenient to express an operator as a composition of several 3-node linear operators with simple treatment of nodes at end. This keeps us from the trouble of using a separate algorithm to evaluate derivatives at each of the nodes with $n = 1, \ldots, 4$ and $n = N - 3, \ldots, N + 1$.

The frequency response $H^{(1)}$ of the first-order differential operator, $D^{(1)}$, is:

$$H^{(1)}(\omega) = i \sin(\omega) \left[\cos^2(\omega/2) + \frac{1.7}{4}\sin^2(\omega)\right] \left[\cos^2(\omega/2) + \frac{1}{4}\sin^2(\omega)\right]. \qquad (A.4)$$

Notice that this is pure imaginary, so it doesn't have any phase shift. Additionally it has a frequency response reasonably close to that of mathematical differentiation

Table A.1: Resolving Efficiency $e_1(\epsilon)$ of the First-Order Derivative Schemes

Scheme	$\epsilon = 0.1$	$\epsilon = 0.01$	$\epsilon = 0.001$
Improved first-order differentiator	0.29	0.16	0.10
Old first-order differentiator	0.25	0.08	0.02

for low frequency, and suppresses high frequency signals sufficiently. The fractional differences of frequency response for the old and improved differentiators are depicted in Fig. A.1 to show the low frequency characteristics. By composing the central difference scheme with the filter, low frequency response was improved considerably compared with that of the old differentiator (refer to Fig. A.1).

Before making comparison, let's define resolving efficiency of approximate first-order differentiators, $e_1(\epsilon) \equiv \omega_f/\pi$ [18]. The value ω_f is the maximum wave-number of well-resolved wave satisfying the error tolerance relation $\mid H^{(1)}(\omega) - i\omega \mid /\omega \leq \epsilon$ for any given positive value of ϵ. The resolution characteristics of the old and improved differentiators are tabulated in Table A.1. In this paper, $Q = 1.70$ was chosen to maximize the resolving efficiency for $\epsilon = 1.0 \times 10^{-4}$ (refer to Fig. A.1). If one wants to maximize the resolving efficiency for $\epsilon = 5.2 \times 10^{-4}$, the natural choice would be $Q = 1.75$ (refer to Fig. A.1). According to Fig. A.1 and Table A.1, the improved first-order differentiation scheme is better than the old differentiator. At the same time, it is superior to the old differentiator in suppressing high frequency signals (refer to Fig. A.2). It should be pointed out that the cutoff frequency ω_{cutoff} is about 1.05 for this improved first-order differentiator judging from the frequency response.

A second-order differentiator is designed separately because when we apply the first-order differentiator twice (which is acceptable in the light of mathematics), it effectively is a 22 point formula and is computationally inadequate if we can get results with comparable accuracy with small number of points to be used. The

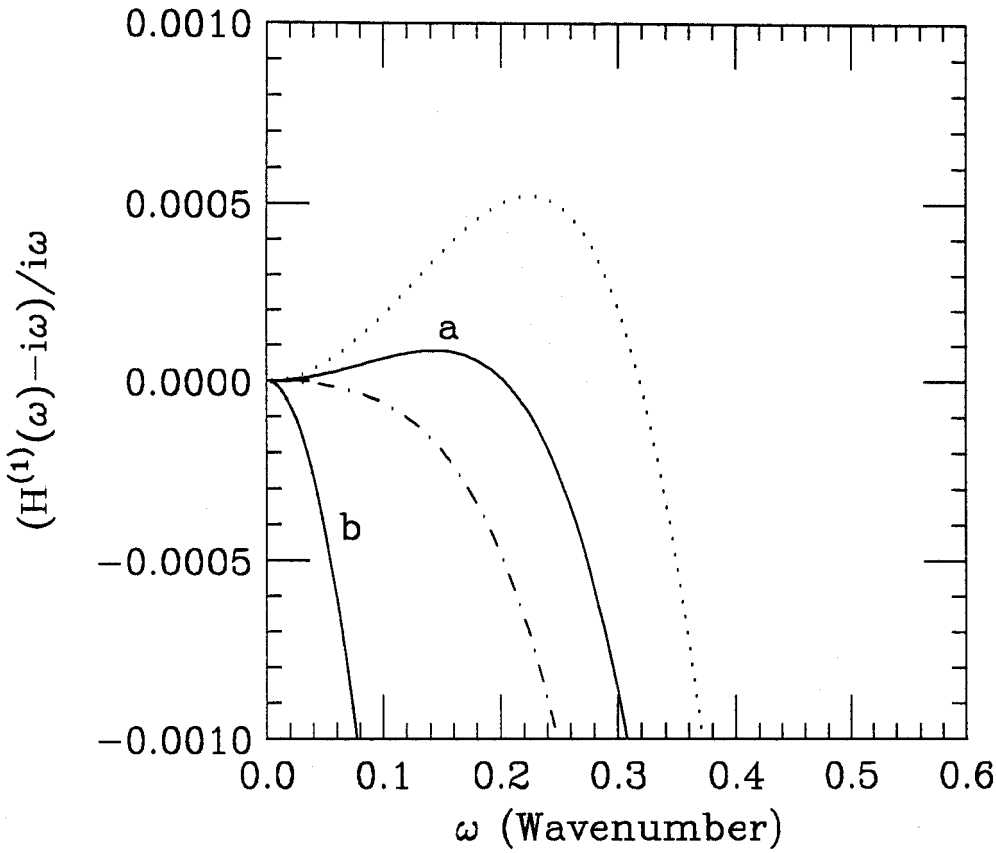

Figure A.1: Plot of $(H^{(1)}(\omega) - i\omega)/i\omega$ over the range $0 \leq \omega \leq 0.6$ for the old differentiator (real line "b"), and that for the improved differentiator (solid line "a") with $Q = 1.70$. The dotdash line corresponds to $Q = 1.65$ and the dotted line to $Q = 1.75$. Composition of the central difference scheme "b" with the filter improves the low frequency behavior significantly, which results in "a" with $Q = 1.70$.

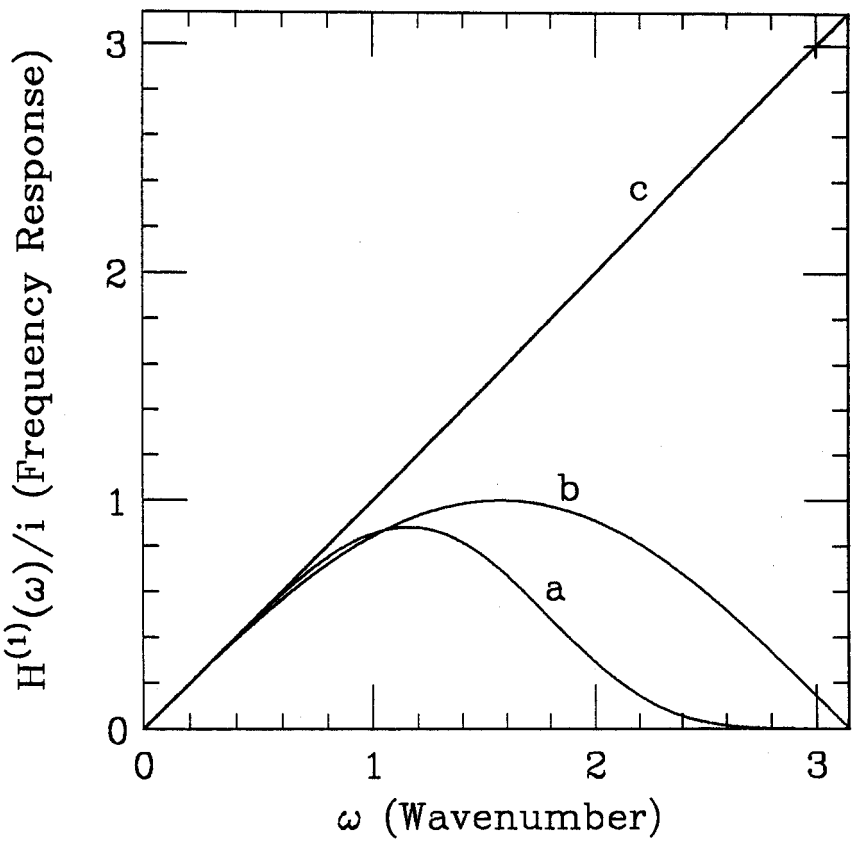

Figure A.2: Plots of $H^{(1)}(\omega)/i$, as a function of the wavenumber ω over the range $0 \leq \omega \leq \pi$. Curve "a" is for our improved differentiator, curve "b" for the old differentiator, and curve "c" for the mathematical first-order differentiator. "a" is superior to "b" in suppressing high frequency signals and shows a frequency response reasonably close to that of the mathematical differentiator for low frequency as well. It should be pointed out that the cutoff frequency ω_{cutoff} is about 1.05.

improved second-order differentiator again is a combination of the central difference scheme (refer to Eq. A.5) and a filter, which ends up with being an eleven-point formula, just like the improved first-order differentiator presented previously. The second-order central difference scheme is defined as follows:

$$f_i'' = \left(f_{i+1} + f_{i-1} - 2f_i\right)/\Delta^2 \tag{A.5}$$

where $f_i = f(x_i)$ and Δ is the step size of mesh. With the choice of $Q = 1.36$, reasonable low frequency response was obtained for the second-order differentiator. More detailed discussion about the choice $Q = 1.36$ is given at the section for resolving efficiency. The operator $D^{(2)}$ that approximates second-order derivatives $\{\frac{d^2}{dx^2} f(x_n)\}$ for $n = 1, \ldots, N$ from a given set of data $\{f_n\}$ for $n = 0, \ldots, N+1$ is given below:

f_n, for $n = 0, \ldots, N+1$

$\Downarrow$

$d_n = \left(f_{n+1} + f_{n-1} - 2f_n\right)/\Delta^2$, for $n = 1, \ldots, N$

$\Downarrow$

$s_n = \left(d_{n+1} + 2d_n + d_{n-1}\right)/4$

$s_1 = d_1, \quad s_N = d_N$

$\Downarrow$

$g_n = s_n - \dfrac{1.36}{4}\left(s_{n+1} + s_{n-1} - 2s_n\right)$

$g_1 = s_1, \quad g_N = s_N$

$\Downarrow$

$h_n = \left(g_{n+1} + 2g_n + g_{n-1}\right)/4$

$h_1 = g_1, \quad h_N = g_N$

$\Downarrow$

$$\frac{d^2}{dx^2} f(x_n) = h_n - \frac{1}{4}\left(h_{n+1} + h_{n-1} - 2h_n\right)$$

$$\frac{d^2}{dx^2} f(x_1) = h_1, \quad \frac{d^2}{dx^2} f(x_N) = h_N.$$

The frequency response $H^{(2)}$ of the second-order differential operator, $D^{(2)}$, is:

$$\begin{aligned} H^{(2)}(\omega) &= -4\sin^2(\omega/2)\left[\cos^2(\omega/2) + \frac{1.36}{4}\sin^2(\omega)\right] \\ &\quad \times \left[\cos^2(\omega/2) + \frac{1}{4}\sin^2(\omega)\right]. \end{aligned} \tag{A.6}$$

Notice that this is purely real, so it doesn't have any phase shift. The cutoff frequency ω_{cutoff} is about 1.05 for this improved second-order differentiator judging from this frequency response. The fractional differences of frequency response for the old and improved differentiators are depicted in Fig. A.3. By composing the standard central difference scheme with the filter, the low frequency response was improved considerably compared with that of the old differentiator (refer to Fig. A.3).

In a similar way, let's define a resolving efficiency of approximate second-order differentiators, $e_2 \equiv \omega_f/\pi$ where the value ω_f is the maximum wave-number of well-resolved wave satisfying the tolerance relation $\mid H^{(2)} + \omega^2 \mid /\omega^2 \leq \epsilon$ for any given value of ϵ. In this paper, $Q = 1.36$ was chosen to maximize the resolving efficiency for $\epsilon = 1.0 \times 10^{-4}$ (refer to Fig. A.3). If one wants to maximize the resolution characteristics for $\epsilon = 4.3 \times 10^{-4}$, the natural choice would be $Q = 1.40$ (refer to Fig. A.3). The resolving efficiency for the old and improved differentiators are tabulated in Table A.2. The improved second-order differentiation scheme is better than the old differentiator for low frequency signals (refer to Fig. A.3 and Table A.2). At the same time, it is superior to the old differentiator in suppressing high frequency signals (refer to Fig. A.4).

The reason why Gordon and Taivassalo [1, 14] used Eq. A.2 instead of Eq. A.5 is that the frequency response of Eq. A.2 at $\omega = \pi$ is equal to 0 while that of Eq. A.5 is not equal to 0. Due to this, Eq. A.5 does not properly suppresses high frequency

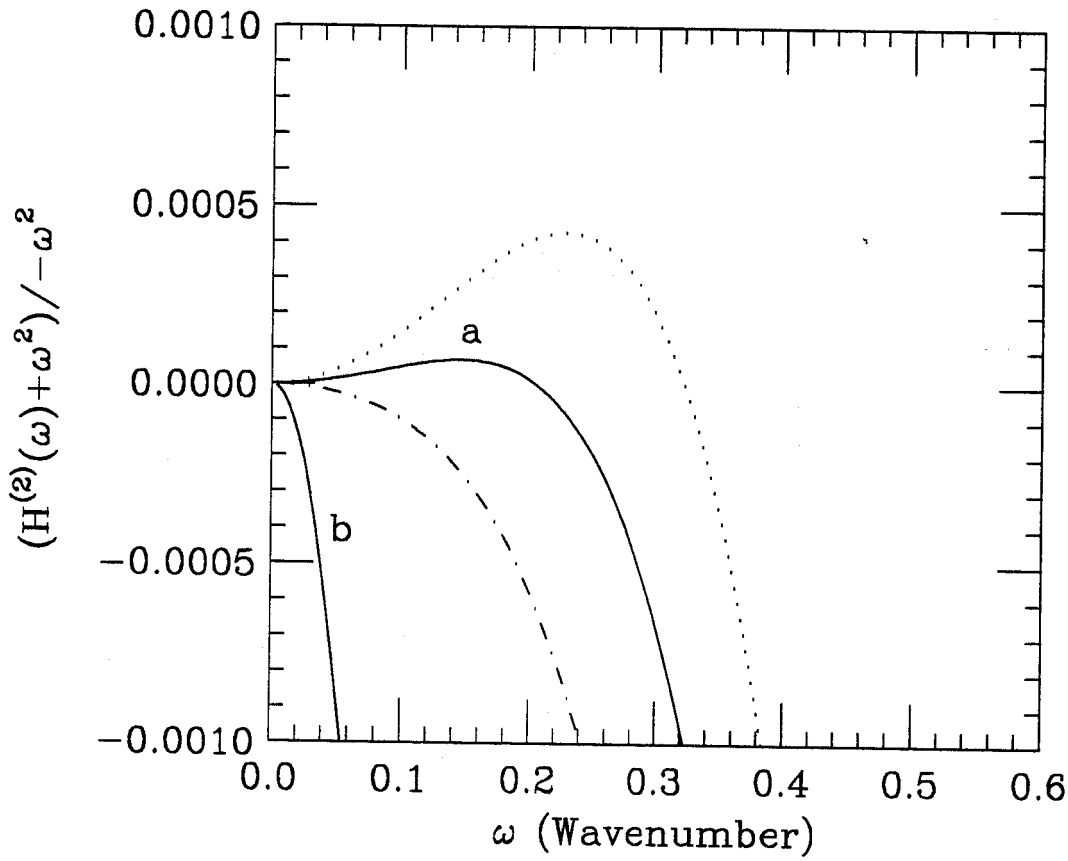

Figure A.3: Plot of $(H^{(2)}(\omega) + \omega^2)/ - \omega^2$ over the range $0 \leq \omega \leq 0.6$ for the old differentiator (solid line "b"), and that for the improved differentiator (solid line "a") with $Q = 1.36$. The dotdash line corresponds to $Q = 1.30$ and the dotted line to $Q = 1.40$. Composition of the central difference scheme with the filter improves the low frequency behavior significantly, which results in "a" with $Q = 1.36$.

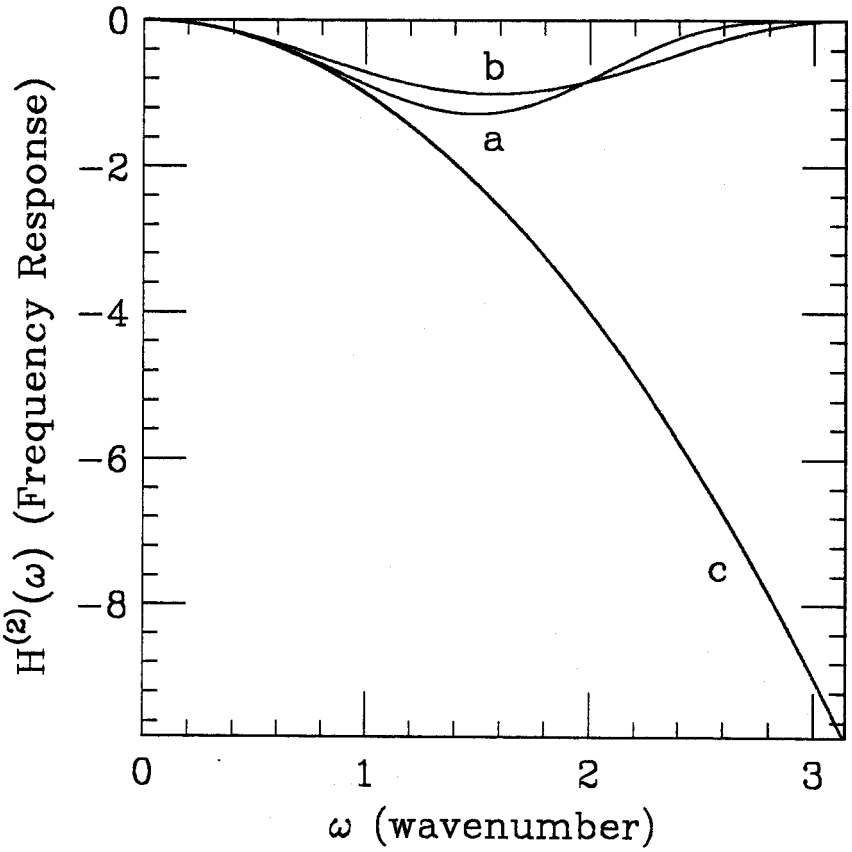

Figure A.4: Plot of the frequency response $H^{(2)}(\omega)$ as a function of the wavenumber ω over the range $0 \leq \omega \leq \pi$. Curve "a" is for our improved second-order differentiator, curve "b" for the old differentiator, and curve "c" for the mathematical second-order differentiator. "a" is superior to "b" in suppressing high frequency signals and shows a low frequency response reasonably close to that of the mathematical differentiator as well. It should be noted that the cutoff frequency ω_{cutoff} is about 1.05.

Table A.2: Resolving Efficiency $e_2(\epsilon)$ of the Second-Order Derivative Schemes

Scheme	$\epsilon = 0.1$	$\epsilon = 0.01$	$\epsilon = 0.001$
Improved second-order differentiator	0.30	0.17	0.10
Old second-order differentiator	0.18	0.06	0.02

signals, which makes it difficult to apply these schemes successively to get higher order derivatives of data with noise.

A.2 Design of the first and second order differentiators in two dimensions

Mathematically one can evaluate a partial derivative in two-dimension only by applying the differentiator designed for one-dimensional data to two-dimensional data. It is true for data which do not contain any noise at all. As is presented at the later section of this appendix (see section A.4), it turns out to be very useful to add an additional filtering in y when a partial derivative with respect to x is taken of data which contain noise from any source including truncation errors.

For the partial differentiators in two dimension, the differentiators for one dimensional data presented in the previous section composed with a filter in y are used, when partial derivative is taken with respect to x. For the sake of convenience, x filter in the differentiators in one-dimension will be called "primary filter" and y filter will be called "secondary filter" when a partial derivatives with respect to x is taken. In other words, the difference between the differentiators in one-dimension and two-dimension is the addition of "secondary filter" such that when partial differentiation with respect to x (y) is performed, suppression of high frequency signals with respect to y (x) should be performed at the same time which passes through low

frequency signals and provides a strong suppression of high frequency signals. This ensures the suppression of noise signals when partial differential operators are applied successively to get higher order derivatives. The importance of this filter is very well demonstrated in Table A.6.

The filter F_y that transforms $\{f_{n,m}\}$ to $\{\hat{f}_{n,m}\}$ suppressing high frequency signals with respect to y with a choice of $Q = 1.01$ is given below:

$$f_{n,m}, \text{ for } n = 0, \ldots, N+1, \text{ and } m = 0, \ldots, M+1$$

$$\Downarrow$$

$$g_{n,m} = \left(f_{n,m-1} + 2f_{n,m} + f_{n,m+1}\right)/4$$

$$g_{n,0} = f_{n,0}, \quad g_{n,M+1} = f_{n,M+1}$$

$$\Downarrow$$

$$h_{n,m} = g_{n,m} - \frac{1.01}{4}\left(g_{n,m-1} + g_{n,m+1} - 2g_{n,m}\right)$$

$$h_{n,0} = g_{n,0}, \quad h_{n,M+1} = g_{n,M+1}$$

$$\Downarrow$$

$$k_{n,m} = \left(h_{n,m-1} + 2h_{n,m} + h_{n,m+1}\right)/4$$

$$k_{n,0} = h_{n,0}, \quad k_{n,M+1} = h_{n,M+1}$$

$$\Downarrow$$

$$\hat{f}_{n,m} = k_{n,m} - \frac{1}{4}\left(k_{n,m-1} + k_{n,m+1} - 2k_{n,m}\right)$$

$$\hat{f}_{n,0} = k_{n,0}, \quad \hat{f}_{n,M+1} = k_{n,M+1}.$$

The frequency response $H_y^{(F)}$ of the filter, F_y, with $Q = 1.01$ is as follows:

$$H_y^{(F)}(\omega_x, \omega_y) = \left[\cos^2(\omega_y/2) + \frac{1.01}{4}\sin^2(\omega_y)\right]\left[\cos^2(\omega_y/2) + \frac{1}{4}\sin^2(\omega_y)\right], \qquad (A.7)$$

and Fig. A.5 shows the plot of this frequency response.

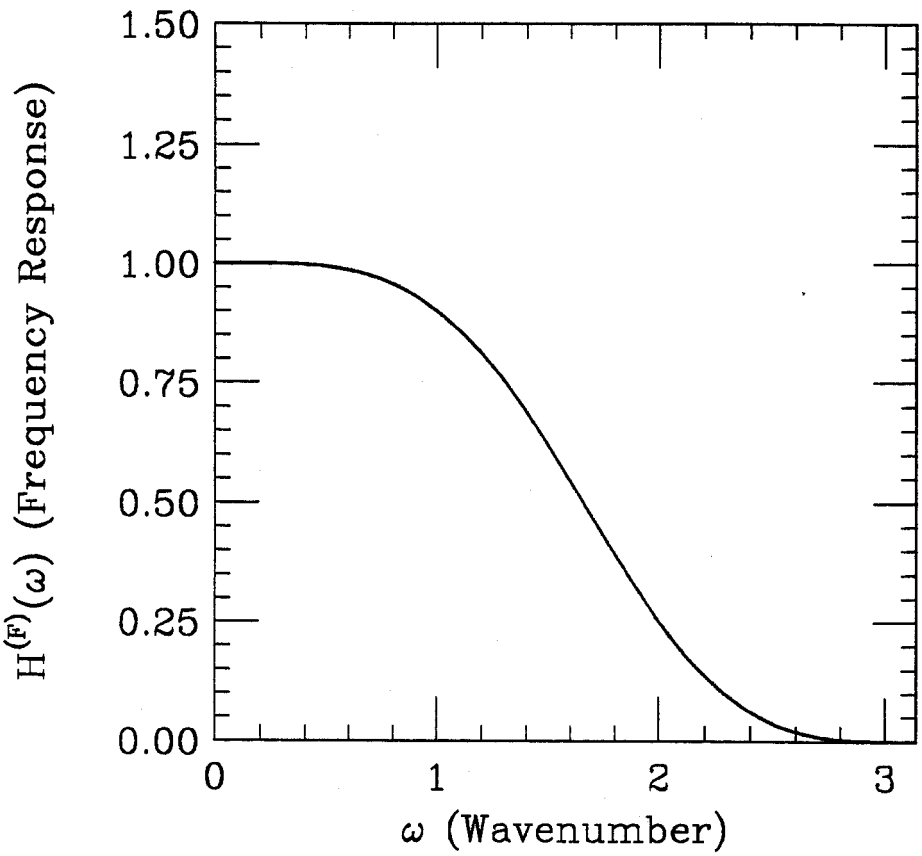

Figure A.5: Plot of the frequency response, $H^{(F)}(\omega)$ over the range $0 \leq \omega \leq \pi$, of the filter used for the improved partial differentiators with $Q = 1.01$ as a function of wavenumber, ω. The nice low frequency response and the suppression of high frequency signals are shown.

Let's define a resolving efficiency of the filter, $e_F \equiv \omega_f/\pi$ where the value ω_f is the maximum wave-number of well-resolved wave satisfying the tolerance relation $\mid H^{(F)} - 1 \mid \leq \epsilon$. $e_F(\epsilon = 0.1) = 0.32$, $e_F(\epsilon = 0.01) = 0.17$, and $e_F(\epsilon = 0.001) = 0.10$.

A first-order partial differentiator with respect to x is considered. A combination of the standard central difference scheme (refer to Eq. A.1) and a x filter (with $Q = 1.70$) and a y filter (with $Q = 1.01$) is used. In this case, the x filter will be called "primary filter" and the y filter "secondary filter". The differential operator $D_x^{(1)}$ that approximates first-order partial derivatives with respect to x, $\{\frac{\partial}{\partial x} f(x_n, y_m)\}$ for $n = 1, \ldots, N$ and $m = 0, \ldots, M+1$ from the data $\{f_{n,m} = f(x_n, y_m)\}$ for $n = 0, \ldots, N+1$ and $m = 0, \ldots, M+1$ is:

$$f_{n,m}, \text{ for } n = 0, \ldots, N+1, \text{ and } m = 0, \ldots, M+1$$

$$\Downarrow$$

$$d_{n,m} = (f_{n+1,m} - f_{n-1,m})/2\Delta_x$$

$$\text{for } n = 1, \ldots, N, \text{ and } m = 0, \ldots, M+1$$

$$\Downarrow$$

$$sx_{n,m} = (d_{n+1,m} + 2d_{n,m} + d_{n-1,m})/4$$

$$sx_{1,m} = d_{1,m}, \; sx_{N,m} = d_{N,m}$$

$$\Downarrow$$

$$gx_{n,m} = sx_{n,m} - \frac{1.7}{4}(sx_{n+1,m} + sx_{n-1,m} - 2sx_{n,m})$$

$$gx_{1,m} = sx_{1,m}, \; gx_{N,m} = sx_{N,m}$$

$$\Downarrow$$

$$hx_{n,m} = (gx_{n+1,m} + 2gx_{n,m} + gx_{n-1,m})/4$$

$$hx_{1,m} = gx_{1,m}, \; hx_{N,m} = gx_{N,m}$$

$$\Downarrow$$

$$kx_{n,m} = hx_{n,m} - \frac{1}{4}\left(hx_{n+1,m} + hx_{n-1,m} - 2hx_{n,m}\right)$$

$$kx_{1,m} = hx_{1,m},\ kx_{N,m} = hx_{N,m}$$

$$\Downarrow$$

$$sy_{n,m} = \left(kx_{n,m+1} + 2kx_{n,m} + kx_{n,m-1}\right)/4$$

$$sy_{n,0} = kx_{n,0},\ sy_{n,M+1} = kx_{n,M+1}$$

$$\Downarrow$$

$$gy_{n,m} = sy_{n,m} - \frac{1.01}{4}\left(sy_{n,m+1} + sy_{n,m-1} - 2sy_{n,m}\right)$$

$$gy_{n,0} = sy_{n,0},\ gy_{n,M+1} = sy_{n,M+1}$$

$$\Downarrow$$

$$hy_{n,m} = \left(gy_{n,m+1} + 2gy_{n,m} + gy_{n,m-1}\right)/4$$

$$hy_{n,0} = gy_{n,0},\ hy_{n,M+1} = gy_{n,M+1}$$

$$\Downarrow$$

$$\frac{\partial}{\partial x} f\left(x_n, y_m\right) = hy_{n,m} - \frac{1}{4}\left(hy_{n,m+1} + hy_{n,m-1} - 2hy_{n,m}\right)$$
$$\frac{\partial}{\partial x} f\left(x_n, y_0\right) = hy_{n,0},\ \frac{\partial}{\partial x} f\left(x_n, y_{M+1}\right) = hy_{n,M+1},$$

where Δ_x is the step size of x-mesh.

Evaluation of derivatives at nodes near boundaries is handled properly and with simplicity without introducing additional algorithms to handle them. In a similar way, the approximate first-order partial differentiator $D_y^{(1)}$ with respect to y can be obtained. The corresponding frequency response of $D_x^{(1)}$ is:

$$\begin{aligned} H_x^{(1)}\left(\omega_x, \omega_y\right) &= i \sin\left(\omega_x\right)\left[\cos^2\left(\omega_x/2\right) + \frac{1.7}{4}\sin^2\left(\omega_x\right)\right] \\ &\quad \times \left[\cos^2\left(\omega_x/2\right) + \frac{1}{4}\sin^2\left(\omega_x\right)\right]\left[\cos^2\left(\omega_y/2\right) + \frac{1.01}{4}\sin^2\left(\omega_y\right)\right] \\ &\quad \times \left[\cos^2\left(\omega_y/2\right) + \frac{1}{4}\sin^2\left(\omega_y\right)\right], \end{aligned} \tag{A.8}$$

and Fig. A.6 shows the plot of the frequency response in frequency domain. It should

be noted that because this is pure imaginary there isn't any phase shift.

A second-order partial differentiator with respect to x is considered. The standard central difference scheme (refer to Eq. A.5) composed with a x filter (with $Q = 1.36$) and a y filter (with $Q = 1.01$) is used. In this case, x filter is called "primary filter" and y filter is called "secondary filter". The differential operator $D_x^{(2)}$ that approximates second-order partial differentiation $\{\frac{\partial^2}{\partial x^2} f(x_n, y_m)\}$ with respect to x for $n = 1, \ldots, N$ and $m = 0, \ldots, M+1$ from data $\{f_{n,m} = f(x_n, y_m)\}$ for $n = 0, \ldots, N+1$ and $m = 0, \ldots, M+1$ is as follows:

$$f_{n,m}, \text{ for } n = 0, \ldots, N+1, \text{ and } m = 0, \ldots, M+1$$

$$\Downarrow$$

$$d_{n,m} = \left(f_{n+1,m} + f_{n-1,m} - 2f_{n,m}\right)/\Delta^2$$

$$\text{for } n = 1, \ldots, N, \text{ and } m = 0, \ldots, M+1$$

$$\Downarrow$$

$$sx_{n,m} = \left(d_{n+1,m} + 2d_{n,m} + d_{n-1,m}\right)/4$$

$$sx_{1,m} = d_{1,m}, \; sx_{N,m} = d_{N,m}$$

$$\Downarrow$$

$$gx_{n,m} = sx_{n,m} - \frac{1.36}{4}\left(sx_{n+1,m} + sx_{n-1,m} - 2sx_{n,m}\right)$$

$$gx_{1,m} = sx_{1,m}, \; gx_{N,m} = sx_{N,m}$$

$$\Downarrow$$

$$hx_{n,m} = \left(gx_{n+1,m} + 2gx_{n,m} + gx_{n-1,m}\right)/4$$

$$hx_{1,m} = gx_{1,m}, \; hx_{N,m} = gx_{N,m}$$

$$\Downarrow$$

$$kx_{n,m} = hx_{n,m} - \frac{1}{4}\left(hx_{n+1,m} + hx_{n-1,m} - 2hx_{n,m}\right)$$

$$kx_{1,m} = hx_{1,m}, \; kx_{N,m} = hx_{N,m}$$

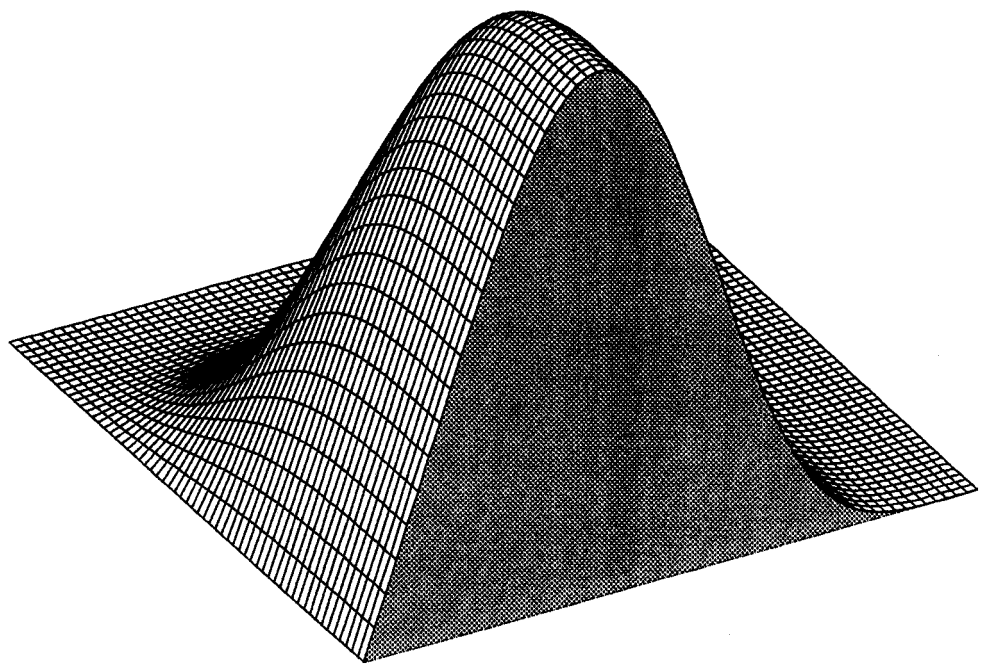

Figure A.6: Plot of the frequency response of the improved first-order partial differentiator with respect to x divided by i, $H_x^{(1)}(\omega_x, \omega_y)/i$, for $0 \leq \omega_x \leq \pi$ and $0 \leq \omega_y \leq \pi$. The suppression of high frequency signals both in x and y should be noted. It also shows the correct linear behavior for low frequencies.

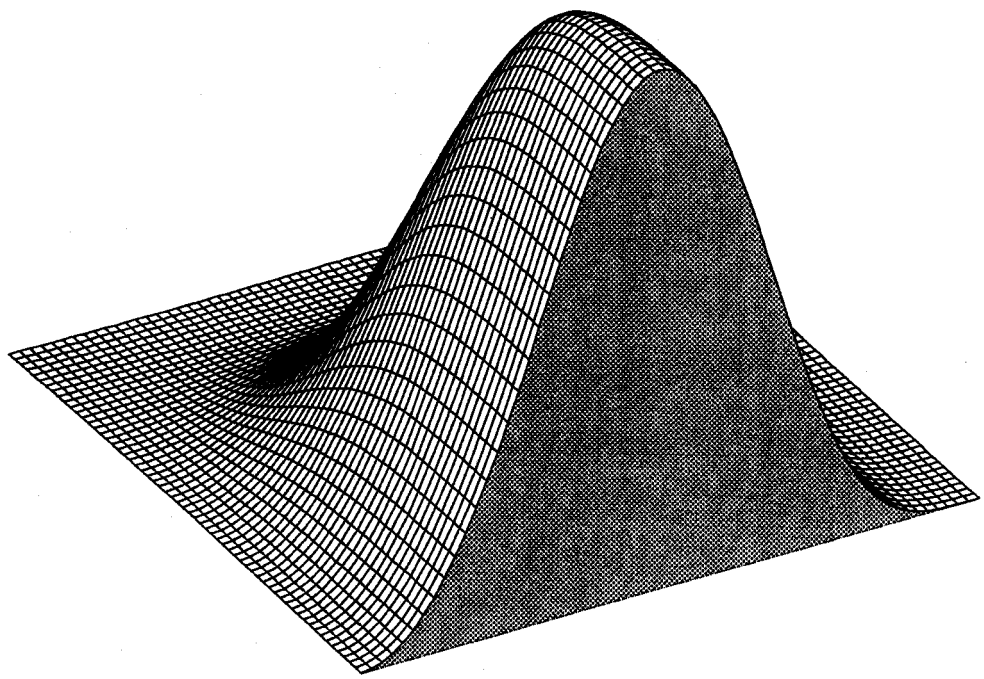

Figure A.7: Plot of the frequency response of the improved second-order partial differentiator with respect to x multiplied by (-1), $-H_x^{(2)}(\omega_x, \omega_y)$, for $0 \leq \omega_x \leq \pi$ and $0 \leq \omega_y \leq \pi$. The suppression of high frequency signals both in x and y should be noted. It shows the correct quadratic behavior for low frequency components as well.

$$\Downarrow$$

$$sy_{n,m} = \left(kx_{n,m+1} + 2kx_{n,m} + kx_{n,m-1}\right)/4$$

$$sy_{n,0} = kx_{n,0},\ sy_{n,M+1} = kx_{n,M+1}$$

$$\Downarrow$$

$$gy_{n,m} = sy_{n,m} - \frac{1.01}{4}\left(sy_{n,m+1} + sy_{n,m-1} - 2sy_{n,m}\right)$$

$$gy_{n,0} = sy_{n,0},\ gy_{n,M+1} = sy_{n,M+1}$$

$$\Downarrow$$

$$hy_{n,m} = \left(gy_{n,m+1} + 2gy_{n,m} + gy_{n,m-1}\right)/4$$

$$hy_{n,0} = gy_{n,0},\ hy_{n,M+1} = gy_{n,M+1}$$

$$\Downarrow$$

$$\frac{\partial^2}{\partial x^2} f\left(x_n, y_m\right) = hy_{n,m} - \frac{1}{4}\left(hy_{n,m+1} + hy_{n,m-1} - 2hy_{n,m}\right)$$

$$\frac{\partial^2}{\partial x^2} f\left(x_n, y_0\right) = hy_{n,0},\ \frac{\partial^2}{\partial x^2} f\left(x_n, y_{M+1}\right) = hy_{n,M+1},$$

where Δ_x is the step size of x-mesh.

The approximate second-order partial differentiation $D_y^{(2)}$ with respect to y can be obtained in a similar way. The corresponding frequency response of $D_x^{(2)}$ is:

$$\begin{aligned} H_x^{(2)}\left(\omega_x, \omega_y\right) &= -4\sin^2\left(\omega_x/2\right)\left[\cos^2\left(\omega_x/2\right) + \frac{1.36}{4}\sin^2\left(\omega_x\right)\right] \\ &\quad \times \left[\cos^2\left(\omega_x/2\right) + \frac{1}{4}\sin^2\left(\omega_x\right)\right]\left[\cos^2\left(\omega_y/2\right) + \frac{1.01}{4}\sin^2\left(\omega_y\right)\right] \\ &\quad \times \left[\cos^2\left(\omega_y/2\right) + \frac{1}{4}\sin^2\left(\omega_y\right)\right] \end{aligned} \tag{A.9}$$

and Fig. A.7 shows the plot of the frequency response in frequency domain.

A.3 Application to the field produced by magnetized iron bars

Two long iron bars were considered with the geometry $-2 \leq x \leq 2$, $-2 \leq y \leq 2$ and $z \geq 1$ for one iron bar and $-2 \leq x \leq 2$, $-2 \leq y \leq 2$ and $z \leq -1$ for the other. These bars are uniformly magnetized in the $+z$ direction with a resultant internal field B_s. Let's define $x_1 = -2$, $x_2 = 2$, $y_1 = -2$ and $y_2 = 2$. The magnetic field due to the two sheets of surface charge [1, 23] is given by:

$$B_z(x,y,z) = \frac{B_s}{4\pi} \sum_{i,j} (-1)^{i+j} \left[\arctan\left(\frac{X_i Y_j}{Z_+ R_+}\right) + \arctan\left(\frac{X_i Y_j}{Z_- R_-}\right) \right] \tag{A.10}$$

where $i, j = 1, 2$, and B_s is taken to be 21.4 kG [1] and where:

$$\begin{aligned} X_i &= x - x_i, \\ Y_j &= y - y_j, \\ Z_+ &= 1 + z, \\ Z_- &= 1 - z, \\ R_\pm &= \left(X_i^2 + Y_j^2 + Z_\pm^2\right)^{1/2}. \end{aligned}$$

The map of the magnetic field $B_z(x, y, z = 0)$ in kG is shown in Fig. A.8 over the range $-4 \leq x \leq 4$ and $-4 \leq y \leq 4$ with $\Delta x = \Delta y = 0.1$.

B_z is Taylor expanded around $z = 0$ just as in Eq. 2.1. For the sake of convenience, let's define:

$$B(x,y) = B_z(x,y,z=0) \tag{A.11}$$

The program "Mathematica" was used to obtain the analytical expressions of various derivatives such as $\nabla_2^2 B, \ldots, \nabla_2^6 B$ with $\nabla_2^2 = \frac{\partial^2}{\partial x^2} + \frac{\partial^2}{\partial y^2}$.

We made comparisons between the results obtained from the analytically differentiated formulas using the program "Mathematica" and the results from the two

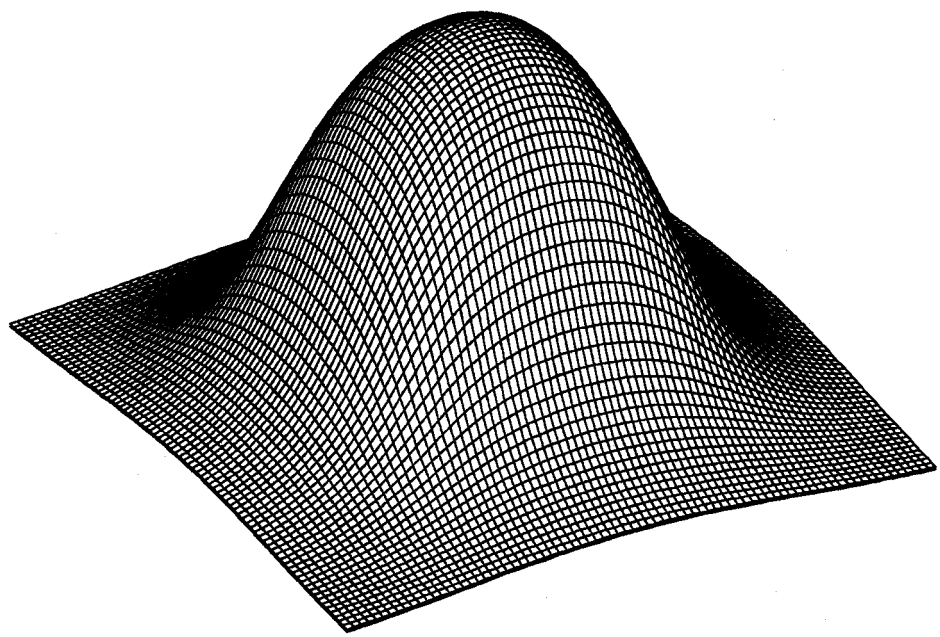

Figure A.8: Map of $B_z(x, y, z = 0)$ produced by two saturated semi-infinite iron bars which are magnetized in the $+z$ direction whose geometry is specified in the text. This field is plotted over the range $-4 \leq x \leq 4$ and $-4 \leq y \leq 4$ with $\Delta x = \Delta y = 0.1$. Notice how fast the field values decrease as the distance from the origin increases. The maximum field value is 12.6 kG.

Table A.3: Comparison of the improved and old differentiators using data without noise

	old differentiators	improved differentiators
term for comparison	$rms(D)$	$rms(D)$
$\nabla_2^2 B \times 0.5^2/2!$	5.34 G	0.360 G
$\nabla_2^4 B \times 0.5^4/4!$	3.79 G	0.598 G
$\nabla_2^6 B \times 0.5^6/6!$	1.59 G	0.454 G

different approximate second-order differential operators, one is the old differentiator used by Gordon and Taivassalo [1, 14] and the other is the improved differentiators described in section A.2.

The numerical calculations start with values of $B(x, y)$ stored in a uniform square mesh with $\Delta x = \Delta y = 0.1$. Data from $-4 \leq x \leq 4$ and $-4 \leq y \leq 4$ were chosen for comparison because this is the region where drastic changes occur. Exact evaluation of the derivatives of various order was done by analytically differentiating Eq. A.10 evaluated on the median plane where $z = 0$ using the program "Mathematica". Numerical evaluation of the derivatives of various order was done by applying the approximate differentiators to the field data of B. In obtaining numerical evaluation of the derivatives, the field data expressed in kG up to the 11th decimal place obtained from Eq. A.11 were used to keep truncation error as small as possible.

In each case, we calculated values of a particular term in the expansion of B_z for $z = 0.5$, which is halfway from the median plane to the poleface. The rms difference in G between the values obtained from the two different approximate methods and the exact values from the analytically differentiated expressions are given in Table A.3 where $rms(D)$ is the rms difference between the numerical and analytical results. The largest magnitudes of the second-order, the fourth-order, and the sixth-order terms of the expansion are 948 G, 140 G, and 25.2 G, respectively.

Figure A.9 shows the map of the second-order term in B_z, $\nabla_2^2 B \times 0.5^2/2!$, derived from the analytical expression whose maximum and minimum are 447 G and -948 G. Figure A.10 shows two maps of the difference in the second-order term in z between the analytical results and those obtained from the two different differentiators, the improved and old differentiators. The top map represents the difference between theory and the improved differentiators, while the bottom map depicts the difference between theory and the old differentiators. These two maps are plotted to the same scale.

In a similar manner, Fig. A.11 depicts the map of the fourth-order term in B_z, $\nabla_2^4 B \times 0.5^4/4!$, obtained from the analytical expression whose maximum and minimum are 140 G and -86.5 G, respectively. Figure A.12 shows two maps of the difference in the fourth-order term in z between the analytical results and those obtained from the two different differentiators. The top map represents the difference between theory and the improved differentiators, while the bottom map depicts the difference between theory and the old differentiators. These two maps are plotted to the same scale.

From these figures and Table A.3, it is clear that the improved differentiators are an order of magnitude more accurate than the old differentiators for the nonlinear terms in B_z at $z = 0.5$. This is because the old differentiators wash out physically important low-frequency components of the data.

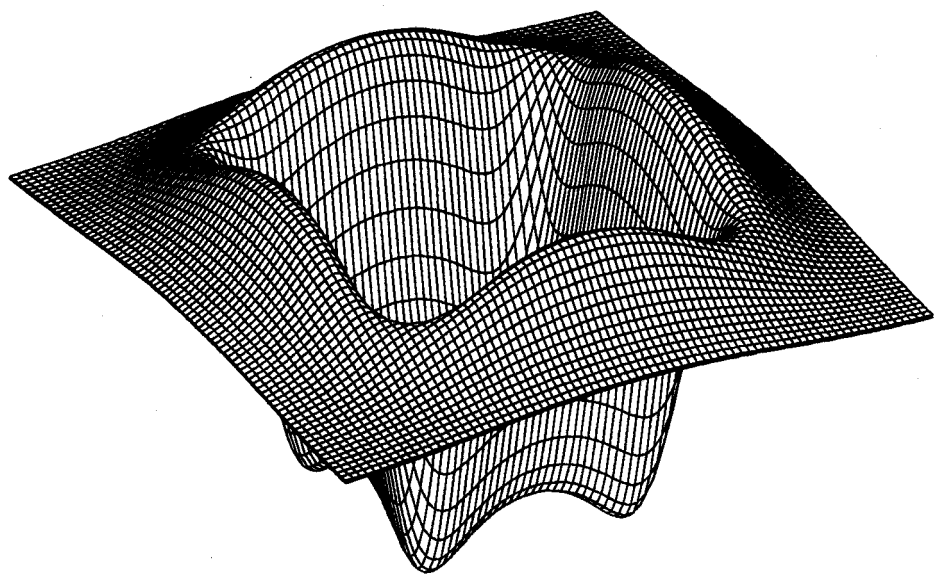

Figure A.9: Map of $\nabla_2^2 B \times 0.5^2/2!$ obtained from the analytical expression. This is plotted over $-4 \leq x \leq 4$ and $-4 \leq y \leq 4$ with $\Delta x = \Delta y = 0.1$. The maximum and the minimum are 446 G and -948 G, respectively.

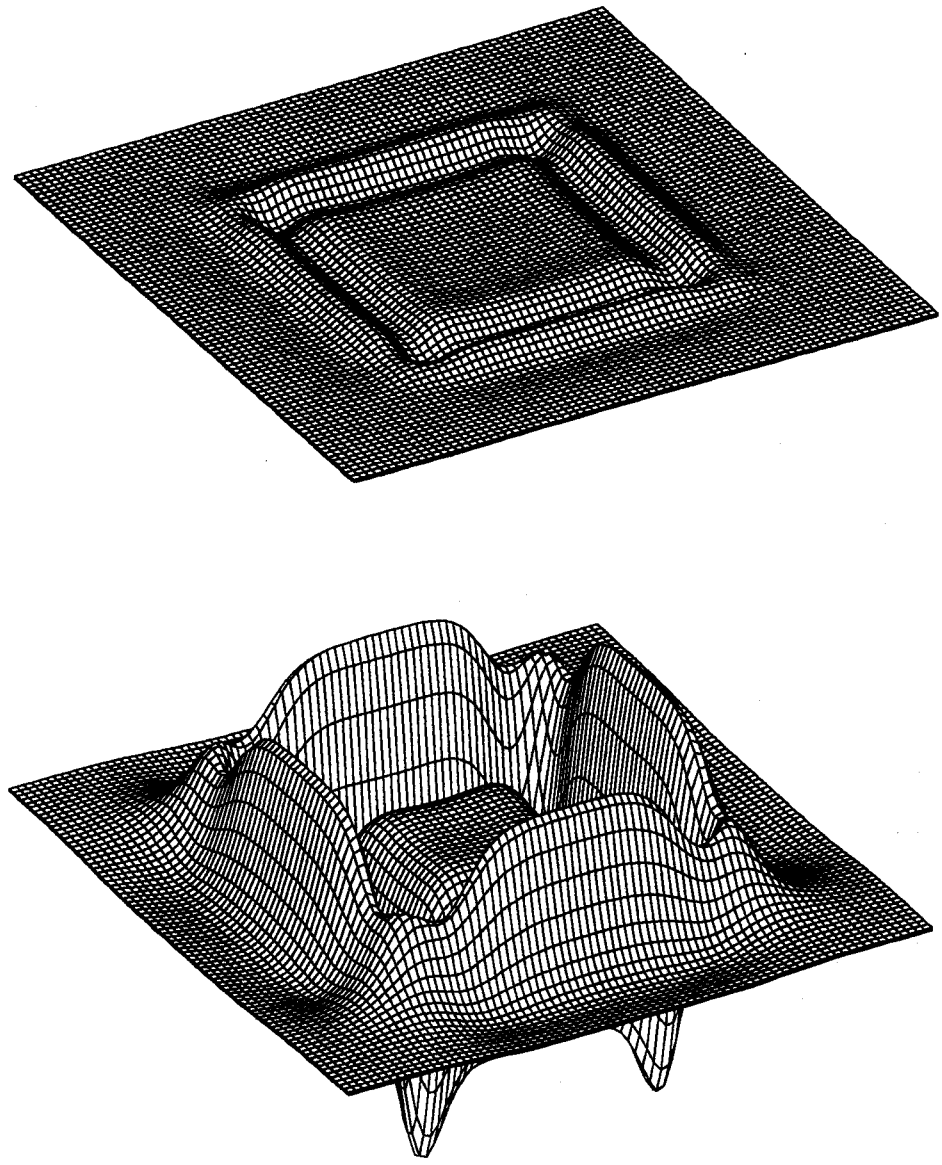

Figure A.10: Two maps of the difference between exact values and those from the two differentiators for $\nabla_2^2 B \times 0.5^2/2!$ term over the range $-4 \leq x \leq 4$ and $-4 \leq y \leq 4$ with $\Delta x = \Delta y = 0.1$. The top map depicts the difference between theory and the improved differentiators, while the bottom map portrays the difference between theory and the old differentiators. Both of these are plotted to the same scale. The maximum and the minimum of the top map are 1.1 G and -1.5 G respectively, while those of the bottom map are 13.2 G and -19.4 G. Clearly, the improved differentiators are about twelve times more accurate than the old differentiators.

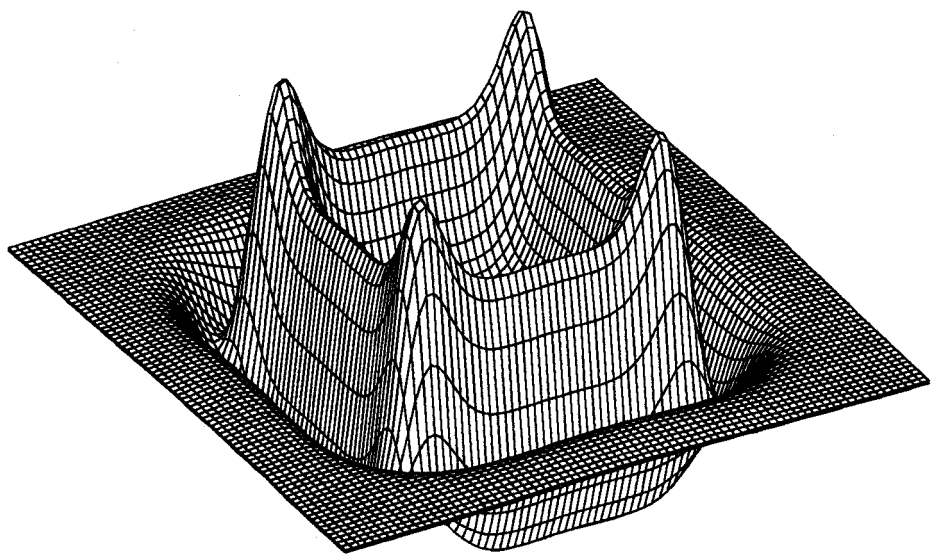

Figure A.11: Map of $\nabla_2^4 B \times 0.5^4/4!$ obtained from the analytical expression. This is plotted over $-4 \leq x \leq 4$ and $-4 \leq y \leq 4$ with $\Delta x = \Delta y = 0.1$. The maximum and the minimum are 140 G and -86.5 G, respectively.

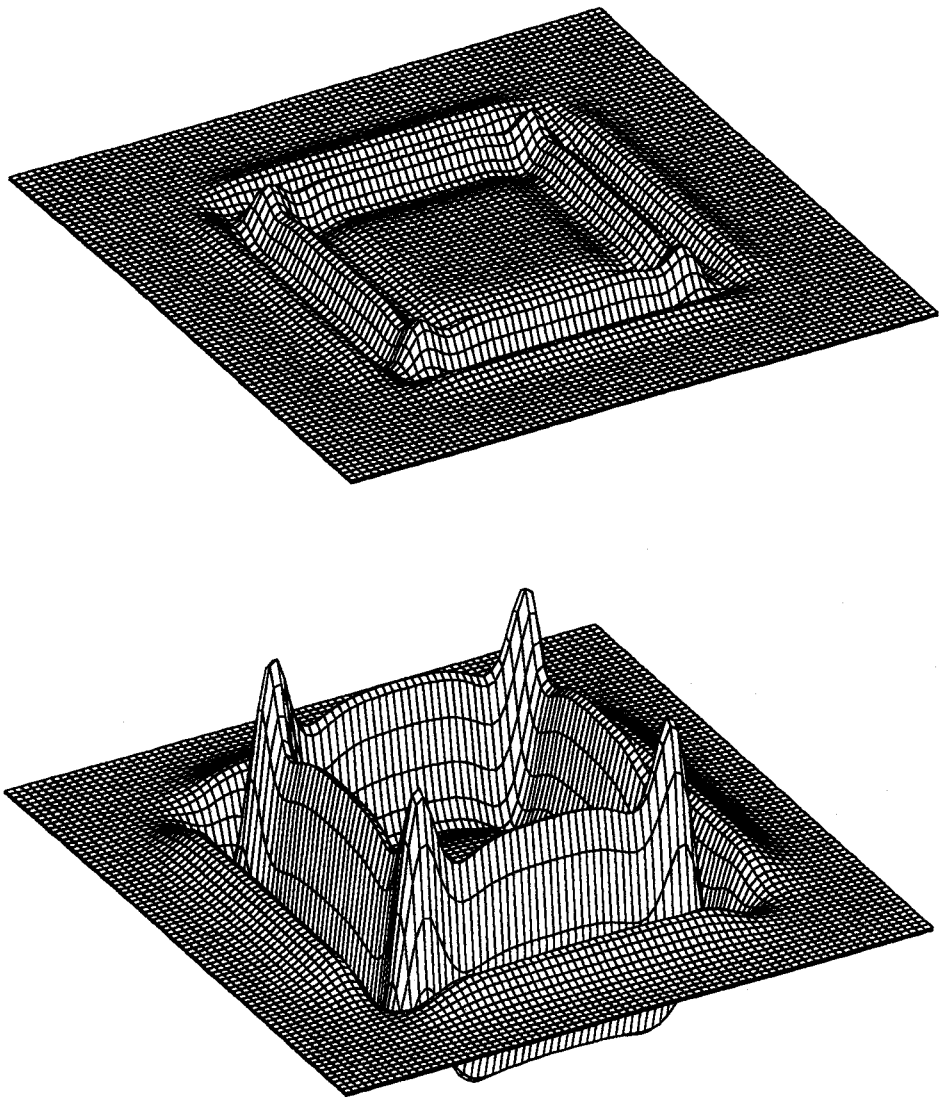

Figure A.12: Two maps of the difference between exact values and those from the two differentiators for $\nabla_2^4 B \times 0.5^4/4!$ term over the range $-4 \leq x \leq 4$ and $-4 \leq y \leq 4$ with $\Delta x = \Delta y = 0.1$. The top map depicts the difference between theory and the improved differentiators, while the bottom map portrays the difference between theory and the old differentiators. Both of these are plotted to the same scale. The maximum and the minimum of the top map are 2.9 G and -2.0 G respectively, while those of the bottom map are 16.3 G and -10.9 G. Clearly, the improved differentiators are about five times more accurate than the old differentiators for the fourth-order term in B_z at $z = 0.5$.

A.4 Application to data with noise

We assumed that noise in the data could be simulated by generating random numbers and adding them to the values of B stored in the square mesh described above. Comparison was then made between the results obtained from the improved and old differentiators to determine their characteristics when applied to data with noise. In order to compare the results with those in Table A.3 above, we used the same mesh spacing, $\Delta x = \Delta y = 0.1$. The random numbers added to the stored field data are within ± 0.1 G, which is around the limit of measurement accuracy. The rms difference between the field data with and without this noise is 5.75×10^{-2} G (which agrees quite well with the expected values, $\left(10/\sqrt{3}\right) \times 10^{-2}$ G).

Table A.4 shows the values of rms differences between the exact derivatives of the field without noise and the results derived from the two numerical differentiators for the field with the noise. This table shows the results for the second, fourth, and sixth-order terms in units of G. The rms values in Table A.4 are larger than those in Table A.3 due to the noise.

It should be noted that the magnitude of random noise is very small compared with the maximum field value of 12.6 kG (see Fig. A.8) for the field described in section A.3, and yet its effect on the derivatives is not negligible at all. The magnitude of the noise is also small compared with the largest magnitudes of the second, fourth, and sixth-order terms which are 948 G, 140 G, and 25.2 G evaluated at $z = 0.5$.

For a comparison, we took rms values of the differences between the values of numerically differentiated derivatives for the field data without the noise and those for the field data with the noise using the two numerical differentiators up to the sixth order. Table A.5 shows the values of rms differences for the two numerical differentiators. The results for the second, fourth, and sixth-order terms are presented

Table A.4: rms differences between the exact derivatives for the field without the noise and those for the field with the noise for the two different numerical differentiators

	old differentiators	improved differentiators
term for comparison	$rms(D)$	$rms(D)$
$\nabla_2^2 B \times 0.5^2/2!$	5.40 G	0.682 G
$\nabla_2^4 B \times 0.5^4/4!$	4.48 G	1.74 G
$\nabla_2^6 B \times 0.5^6/6!$	3.60 G	2.08 G

Table A.5: rms differences between the values of numerically differentiated derivatives for the field with the noise and those for the field without the noise for the two numerical differentiators

	old differentiators	improved differentiators
term for comparison	$rms(D)$	$rms(D)$
$\nabla_2^2 B \times 0.5^2/2!$	0.798 G	0.580 G
$\nabla_2^4 B \times 0.5^4/4!$	2.40 G	1.64 G
$\nabla_2^6 B \times 0.5^6/6!$	3.23 G	2.04 G

in units of G. Addition of noise within ± 0.1 G produced rms differences of 0.580 G (0.798 G) for the second-order term, 1.64 G (2.40 G) for the fourth-order term, and 2.04 G (3.23 G) for the sixth-order term when the improved (old) differentiators were used. It should be noted that these rms differences are large in comparison with the magnitude of the noise. From the rms differences given in Table A.5, it is clear that the improved differentiators are progressively superior to the old differentiators for higher order terms by from 37 % (the second-order term) to 58 % (the sixth-order term) in suppressing high frequency components. Besides, the differences between the rms values in Table A.4 and those in Table A.3 are smaller than the rms values in Table A.5.

Figure A.13 corresponds to Fig. A.10 depicting the map of the difference in $\nabla_2^2 B \times 0.5^2/2!$. The only difference is that in this case, median plane magnetic field data

contain random noise within ± 0.1 G. Figure A.13 shows the combined effects of the errors produced by the two numerical differentiators for the field without the noise and the additional errors due to the added noise. The surface of the top map derived from the improved differentiators is smoother than that at the bottom from the old differentiators.

Figure A.14 also corresponds to Fig. A.12 portraying the map of the difference in $\nabla_2^4 B \times 0.5^4/4!$. The only difference lies again in the inclusion of random noise within ± 0.1 G. Figure A.14 shows the combined effects of the errors produced by the two numerical differentiators for the field without the noise and the additional errors due to the added noise. The surface of the bottom map derived from the old differentiators becomes even sharper than that at the top from the improved differentiators. Besides, the height of individual spikes is larger than that in the top diagram.

As shown in section A.2, our approximate partial differentiators are accompanied by the "secondary filter" which filters data in y (x) direction when partial derivatives are taken with respect to x (y). If the data contain no noise at all and are perfectly analytical, the "secondary filter" makes little difference. But it becomes indispensable when data with noise must be dealt with. Table A.6 shows the values of the rms differences in units of G between results obtained from the improved differentiators with and without the "secondary filter". For the sake of convenience, let's call the former "with secondary filter" and the latter "without secondary filter". As can be seen from this table, the "secondary filter" becomes progressively more important with each succeeding term. Thus the "secondary filter" is indispensable for evaluating higher order derivatives of data with noise.

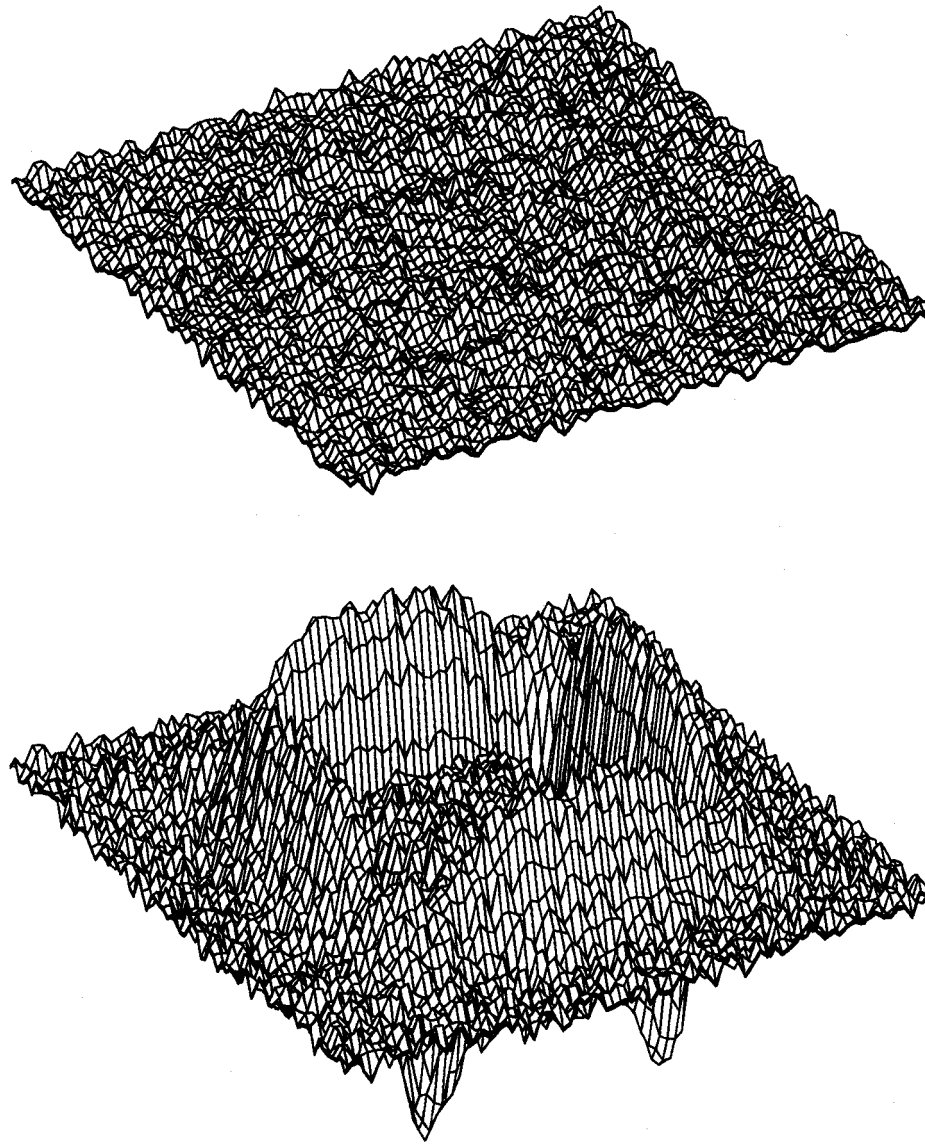

Figure A.13: Two maps of the difference in $\nabla_2^2 B \times 0.5^2/2!$ between the exact derivatives for the field without the noise and those obtained from the two numerical differentiators applied to the field with the random noise within ± 0.1 G. The magnitude of the noise is very small compared with the maximum field value of 12.6 kG of B. These are plotted to the same scale over the range $-4 \leq x \leq 4$ and $-4 \leq y \leq 4$ with $\Delta x = \Delta y = 0.1$. This figure should be compared with Fig. A.10. The top (bottom) map depicts the difference for the improved (old) differentiators. The maximum and the minimum field values of the top map are 2.4 G and -2.4 G respectively, while those of the bottom map are 14.8 G and -20.5 G. These figures show the combined effects of the errors produced by the two numerical differentiators for the field without the noise and the additional errors due to the noise. The surface of the top map is smoother than that at the bottom.

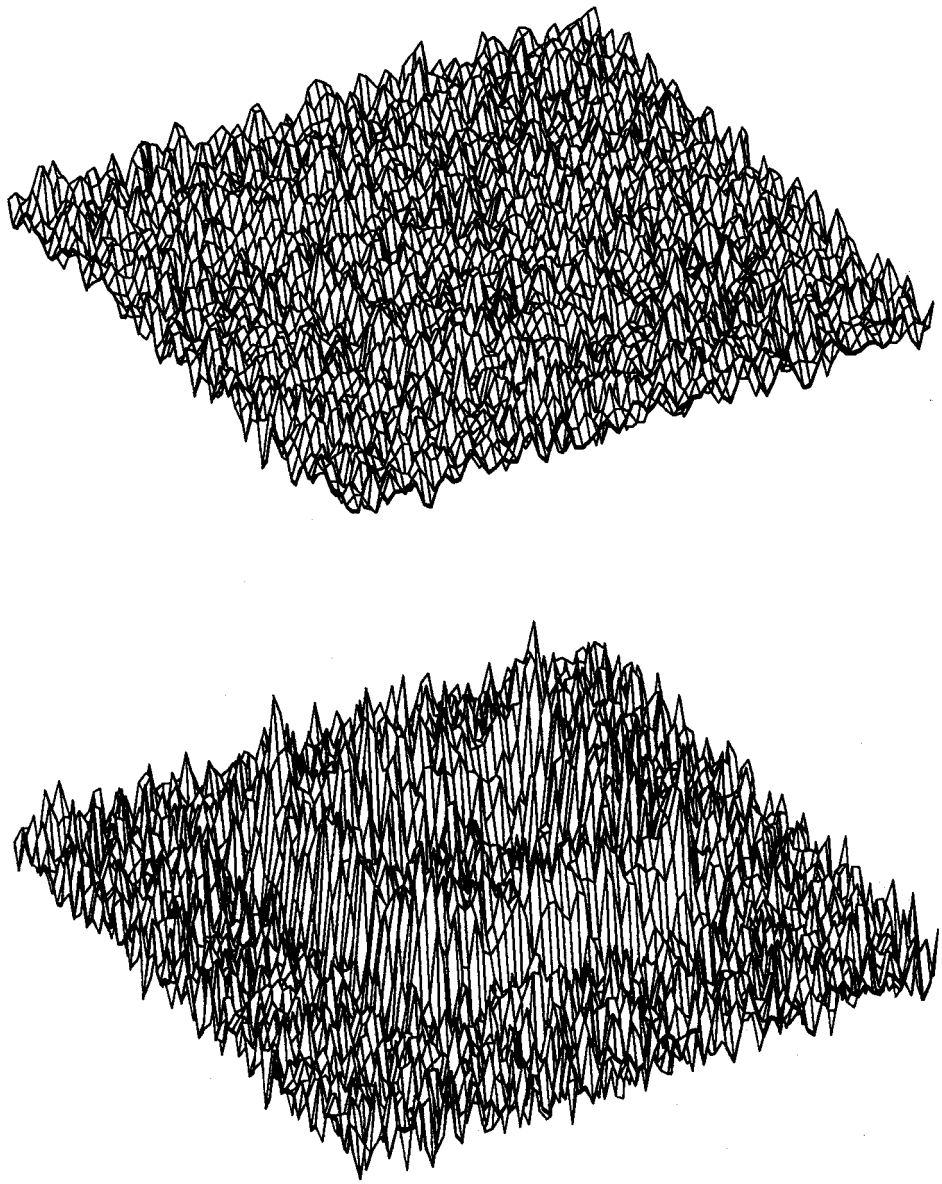

Figure A.14: Two maps of the difference in $\nabla_2^4 B \times 0.5^4/4!$ between the exact derivatives for the field without the noise and those obtained from the two numerical differentiators applied to the field with the random noise within ± 0.1 G. These are plotted to the same scale over the range $-4 \leq x \leq 4$ and $-4 \leq y \leq 4$ with $\Delta x = \Delta y = 0.1$. This figure should be compared with Fig. A.12. The top (bottom) map depicts the difference for the improved (old) differentiators. The maximum and the minimum of the top map are 6.1 G and -5.8 G respectively, while those of the bottom map are 20.3 G and -15.7 G. These figures again show the combined effects of the errors produced by the two numerical differentiators for the field without the noise and the additional errors due to the noise. The surface of the bottom map is even sharper than that at the top, and the height of individual spikes is larger.

Table A.6: Effects of the secondary filter on data with noise

	With Secondary Filter	Without Secondary Filter
term for comparison	$rms(D)$	$rms(D)$
$\nabla_2^2 B \times 0.5^2/2!$	0.682 G	0.962 G
$\nabla_2^4 B \times 0.5^4/4!$	1.74 G	3.33 G
$\nabla_2^6 B \times 0.5^6/6!$	2.08 G	5.53 G

Bibliography

[1] M. M. Gordon and V. Taivassalo, Nucl. and Instr. and Meth. A**247**, 423 (1986).

[2] M. M. Gordon, F. Marti and X. Y. Wu, Proc. 11th Int. Conf. on Cyclotrons and Their Applications, Ionics, Tokyo (1987) p. 252.

[3] Dong-o Jeon, J. Comput. Phys. in press.

[4] J. A. Nolen, et al., Proc. 12th Int. Conf. on Cyclotrons and Their Applications, World Scientific, Berlin (1991) p. 5.

[5] H. Blosser, et al., Proc. 11th Int. Conf. on Cyclotrons and Their Applications, Ionics, Tokyo (1987) p. 157.

[6] J. A. Nolen, Jr., Proc. 1987 IEEE Particle Accelerator Conf. (IEEE Cat.#87CH2387-9) p. 239.

[7] E. J. N. Wilson, Proc. of CERN Accelerator School on Advanced Accelerator Physics, Oxford, CERN 87-03 (1987) p. 41.

[8] K. Symon, AIP Conf. Proc. **249**, 277 (1991).

[9] R. D. Ruth, AIP Conf. Proc. **153**, 150 (1987).

[10] Dong-o Jeon and M. M. Gordon, Nucl. Instr. and Meth. A **349**, 1 (1994).

[11] H. Blosser and F. Resmini, IEEE Trans. Nucl. Sci. **NS-26**, 3653 (1979).

[12] P. S. Miller, et al., Proc. 9th Int. Conf. on Cyclotrons and Their Applications, Caen (1981) p. 191.

[13] M. M. Gordon, Part. Accel. **16**, 39 (1984).

[14] M. M. Gordon and V. Taivassalo, IEEE Trans. Nucl. Sci. **NS-32**, 2447 (1985).

[15] H. O. Kreiss, S. A. Orszag, and M. Israeli, Annu. Rev. Fluid Mech. **6**, 281 (1974).

[16] R. S. Hirsh, J. Comput. Phys. **19**, 90 (1975).

[17] Y. Adam, J. Comput. Phys. **24**, 10 (1977).

[18] S. K. Lele, J. Comput. Phys. **103**, 16 (1992).

[19] S. G. Rubin and P. K. Khosla, J. Comput. Phys. **24**, 217 (1977).

[20] W. J. Goedheer and J. H. H. M. Potters, J. Comput. Phys. **61**, 269 (1985).

[21] J. G. Proakis and D. G. Manolakis, *Introduction to Digital Signal Processing* (Macmillan, N. Y., 1988).

[22] A. V. Oppenheim and R. W. Schafer, *Discrete- Time Signal Processing* (Prentice Hall, Englewood Cliffs, New Jersey, 1989), p. 149.

[23] R. J. Thome and J. M. Tarrh, *MHD and Fusion Magnets* (Wiley, New York, 1982), p. 319.